Performance Scaling of Magnetic Nozzles for Electric Propulsion

Justin M. Little

A Dissertation

Presented to the Faculty

of Princeton University

in Candidacy for the Degree

of Doctor of Philosophy

Recommended for Acceptance

by the Department of

Mechanical and Aerospace Engineering

Adviser: Edgar Y. Choueiri

January 2015

Abstract

The use of magnetic nozzles (MNs) in electric propulsion (EP) systems is investigated analytically and experimentally. MNs have the potential to efficiently accelerate propellant without the restrictions of electrodes, however, their measured performance has been poor compared to existing EP technology. A theoretical model was developed to understand the requirements for efficient operation. Analytical scaling laws were derived for the mass utilization efficiency, channel efficiency, and MN thermal and divergence efficiencies, in terms of dimensionless parameters that describe the relevant collisional processes in the channel and the radial plasma structure at the MN throat. In comparison to previous MN thrusters, performance levels comparable to state of the art EP systems are only possible if three conditions are met: (1) the thruster operates in a high confinement mode, (2) the plume divergence is significantly reduced, and (3) electron temperatures are increased by an order of magnitude. The final requirement implies these thrusters should be operated with heavy propellants such as xenon to limit the specific impulse to reasonable values.

An experiment was designed to investigate the fundamental dynamics of plasma flow through a MN. The experiment consists of a helicon plasma source and two electromagnetic coils. The plasma parameters are determined at a variety of locations using electric probes mounted on a positioning system. The existence of a critical magnetic field strength for high confinement and the predicted scaling of the mass utilization efficiency were verified. Electron cooling in the magnetically expanding plasma was observed to follow a polytropic law with an exponent that agrees with theory. With decreasing magnetic field, a transition from a collimated plume to an under-collimated plume was found, where an under-collimated plume is defined such that the plume divergence is greater than the magnetic field divergence. This transition was accompanied by the disappearance of an ion-confining potential well at the plasma periphery. Using the potential well as a metric for plasma confinement

downstream, it is shown that confinement is lost when the electrons demagnetize via finite Larmor radius effects. The ambipolar ion response to this demagnetization determines the difference between the two plume modes.

Acknowledgements

I would first like to acknowledge my advisor, Professor Edgar Choueiri, for trusting me with a project that was previously unknown to the lab. This thesis would not have been possible without your patience and guidance through failures and successes. Eddie, your demand for perfection – whether it be the choice of a single word in an abstract, a flawlessly disguised Hindu shuffle, or the aesthetic of some trinket on an audio gadget – is an attribute of life for which we should all strive. I look forward to many more conferences full of cigars, fine whiskey, and southern comfort food.

The experimental work in this thesis would not have been possible without the help of Robert Sorenson. Bob, the work you do in the machine shop is art. Your preparation and attention to detail is apparent in the quality of the parts that you create. I have greatly benefited from your willingness to teach me different concepts and techniques, oftentimes more than once.

I would like to offer a special thanks to Professor Sam Cohen. Sam, I met you a few years before I began my PhD during the weeklong plasma seminar for the NUF program. At the time I was only interested in plasmas for their ability to propel spacecraft. Your appreciation of the fundamental beauty of plasma instilled in me a fascination for plasma physics. I was fortunate to continue to benefit from your enthusiasm often throughout my PhD, first in your plasma lab class, and then through my research. I am grateful that, despite your busy schedule, you were always willing to meet with me to discuss new ideas.

I was fortunate to have interacted with a large number of labmates throughout my time in the EPPDyL. To Ashley, Danny, and Ben, thank you for preparing me for life in the lab. Danny, your ability to overcome the many challenges posed by the LiLFA taught me the perseverance required for successful experimental work. Also, thank you for teaching me that fusion was not discovered across Route 1, but rather by Uribarri *et al.* at the Kalluri Corner buffet. Ben, it was always possible to tell when you were on the verge of a breakthrough by the density of printer paper containing illegible mathematical hyroglyphics on the conference table. Your ability to attack a problem both theoretically and experimentally was inspirational. Thank you for being a good friend. Matt (short) and Matt (tall), thank you for always being around for a therapeutic coffee or beer. To the younger members of the lab; Chris, Pat, Will, Mike, Sebastian, and Pierre-Yves, I greatly appreciated your enthusiasm and humor during my final few years. The visiting students, Lorenzo and Jaume, were some of the most motivated researchers with whom I have worked. Thank you for the enthusiasm that you brought to lab. Finally, my research was assisted by two undergraduates, Margaret and Ian. Your contributions to the initial design of the experiment were invaluable.

To my friends and roommates at 36 Fisher; Anand, Andrew, Owen, Peter, and Sebastian, thank you for the great times and ridiculous conversations. Some of the best years of my life were spent in that broke down palace. I can't help but think of how much faster we all would have graduated if it weren't for that house. To the good Doc Hallowell, it is amazing how we can always pick up where we left off (given

a beer). I am glad to know that I have a great friend wherever life takes me. I look forward to the next Princeton-Harvard reunion.

It is safe to say that this thesis would not have been possible without the continued support from my family. You had faith that I was capable of achieving my crazy dream, even at times when I was in doubt. I took comfort in the fact that, when I returned to visit, I always had a soft bed, a car to drive, a good meal, a (sometimes violent) game of rummy wrinkle, and, above all, a home. Words cannot express how thankful I am to all of you.

Finally, I'd like to acknowledge Johanna, whose impact on my life has made the past four years easily my happiest. You were a constant source of strength when I needed it most. Your sense of adventure motivated us to explore so many incredible places, and allowed me to gain perspective beyond the small town of Princeton. I look forward to our three-month world tour. The patience you've shown towards me these past few months would easily grant you saint status in some circles. From every synapse, thank you.

To my (grand) parents.

Contents

List of Tables

List of Figures

List of Symbols

A	Cross-sectional area
A_p	Langmuir probe electrode area
B	Magnetic field
B_c^*	Critical-B_0 for exhaust plume collimation
B_0^*	Critical-B_0 for high confinement
B_0	Magnetic field strength at magnetic nozzle throat
c_s	Ion acoustic speed
C_T	Magnetic nozzle thrust coefficient
$D_\perp$	Cross-field diffusion coefficient
e	Elementary charge
F	Thrust
f_i	Ion energy distribution function
g_u	Ion velocity increment
h_n	Density profile cross-sectional average
h_w	Density profile shape factor
I_B	Magnet current
I_c	RPA collector current
I_e	Langmuir probe electron current
I_sat	Langmuir probe ion saturation current
I_sp	Specific impulse

j_i	Ion current density
k_b	Boltzmann constant
K	Effective magnetic field curvature
L_{bp}	Distance from backplate to magnetic nozzle throat
L_{cex}	Modified charge-exchange mean free path
L_{ion}	Modified ion mean free path
m_e	Electron mass
m_i	Ion mass
$\dot{m}$	Propellant mass flow rate
$\dot{m}_i$	Ion mass flow rate
$\dot{m}_{i,L}$	Ion mass flow rate at channel exit
$\dot{m}_{i,w}$	Ion mass flow rate the channel wall
$\dot{m}_{i,0}$	Initial ion mass flow rate for performance model
$\dot{m}_f$	Fast neutral flow rate
$\dot{m}_s$	Slow neutral flow rate
M	Ion Mach number
M_e	Ion Mach number at exhaust plane
$\bar{M}_{tp}$	Average ion Mach number at ζ_{tp}
n	Plasma density assuming quasineutrality
n_{cl}	Plasma density along nozzle centerline
n_i	Langmuir probe ion density
Nu	Nusselt number
P	Power
P_k	Exhaust kinetic power
$P_{k,z}$	Exhaust kinetic power in axial direction
P_L	Plasma power at channel exit for performance model
P_w	Plasma power lost to channel wall for performance model

Pe_{an}	Anisotropic Pclet numer
Pe_{an}^{i}	Anisotropic Pclet numer at the injection region
P_0	Initial power for performance model
Q_e	Power due to electron heat conduction
r	Radial coordinate
r^*	Normalized plume radius at the point of ion detachment
r_c	Radius of magnetic coil
r_d	Normalized plasma de-magnetization radius
r_e	Exhaust plane plasma radius normalized by magnet radius
$\bar{r}_f$	Mean plasma flux radius at the throat plane
r_L	Normalized electron Larmor radius
r_t	Throat plane plasma radius normalized by magnet radius
R	Channel radius
R_A	Magnetic nozzle aperture ratio
R_c	Magnetic field radius of curvature
R_e	Magnetic nozzle expansion ratio
R_{cex}	Charge-exchange collision rate
R_{ion}	Ionization collision rate
T_e	Electron temperature
$T_{e,0}$	Electron temperature at the throat center
T_i	Ion temperature
$u_{\theta e}$	Electron azimuthal velocity
u_i	Ion velocity
V	RPA bias voltage
V_b	Ion beam voltage
V_f	Floating potential
V_p	Plasma potential

V_0	Plasma potential at the throat center
z	Axial coordinate
z_ζ^*	Value of z_0 corresponding to ion detachment
$z_{\zeta,\mathrm{tp}}$	Value of z_0 corresponding to ζ_{tp}
z_0	Probe location at $\theta_{\mathrm{ts}} = 0$
α	Ratio of the effective ionization energy to the ionization energy
α_M	Nozzle model mass flow correction for ion Mach number
α_n	Nozzle model mass flow correction for density
α_ϕ	Nozzle model mass flow correction for potential
β	Ratio of thermal to magnetic energy densities
γ_e	Electron polytropic index
$\epsilon_{ei,w}$	Energy per electron-ion pair at channel exit
$\epsilon_{ei,w}$	Energy lost per electron-ion pair to the channel wall
$\epsilon_{\dot{m}}$	Nozzle model mass flow rate error
ϵ_{ion}	Ionization energy
ϵ_{ion}'	Effective ionization energy
ϵ_ψ	Electron streamline separation parameter
ϵ_0	Perimittivity of free space
ζ	Magnetic potential coordinate
ζ_{tp}	Value of ζ corresponding to the turning point of ψ_p
Γ_w	Plasma flux to the channel wall
η_c	Channel efficiency
η_{conv}	Thermal conversion efficiency
η_{div}	Divergence efficiency
η_m	Mass utilization efficiency
$\eta_{m,\mathrm{hc}}$	Mass utilization efficiency limit at high confinement
$\eta_{m,0}$	Initial mass utilization efficiency for performance model

η_{mn}	Magnetic nozzle efficiency
η_{ps}	Power supply efficiency
η_T	Thrust efficiency
η_T^*	Thrust efficiency upper-bound
θ_{B}	Effective magnetic field divergence
θ_{div}	Divergence half-angle
θ_p	Location of ψ_p in translation stage coordinates
θ_{ts}	Translation stage angle referenced to nozzle centerline
$\hat{\lambda}_e$	Electron mean free path normalized by magnet radius
Λ	Ratio of channel length to modified ionization mean free path
Λ_{hc}^*	Critical Λ at high confinement
Λ_{lc}^*	Optimal Λ at low confinement
μ_w	Ratio of wall and channel exit ion mass flow rates
μ_0	Permeability of free space
ξ	Ratio of first excited state energy to ionization energy
Π	Ratio of ionization and charge-exchange mean free paths
Π_B	Magnetic mirror ratio between throat and injection region
σ	Density profile uniformity parameter for nozzle model
σ_n	Density profile standard deviation
σ_t	Electron temperature profile standard deviation
ϕ	Normalized plasma potential for exhaust model
Φ_w	Potential well strength
$\bar{\phi}$	Cross-sectional average of ϕ
φ	Cross-sectional ϕ-correction
χ	Mass flow rate fraction, or ion streamline label
χ_{tp}	Density profile at ζ_{tp}
ψ	Magnetic flux coordinate

ψ_e	Electron streamline coinciding with ψ_p at the throat
ψ_p	Magnetic flux coordinate of plasma edge, or free-jet boundary
$\hat{\psi}_{1/2}$	Density profile HWHM in units of ψ normalized by ψ_p
Ψ	Ratio of ion wall loss rate to collisional ion production rate
Ψ^*	Critical-Ψ for high confinement

Chapter 1

Introduction

Simply stated, a magnetic nozzle (MN) converts random thermal energy of a plasma into directed kinetic energy. This conversion occurs as the plasma expands through a cylindrically symmetric magnetic field that is contoured similar to the solid walls of a conventional rocket nozzle (see Fig. 1.1). A transition from subsonic to supersonic flow occurs near the location of maximum magnetic field strength [1]. Magnetic confinement in the direction perpendicular to the applied field induces electric currents within the plasma [2]. Momentum imparted to the accelerated plasma is transferred back to the MN (producing thrust) through the repulsion of the magnetic circuit and internal plasma currents [3]. Detachment of the plasma from the applied magnetic field is a prerequisite to thrust production, however; the fundamental processes underlying plasma detachment are still a matter of debate [4, 5, 6, 7, 8, 9]. Applications of MNs include laboratory simulations of space plasmas [10], surface processing [11], and plasma propulsion for spaceflight [12].

Because they possess many desirable qualities from the standpoint of plasma propulsion, MNs have been considered as the acceleration stage for a diverse number of concepts ranging from 50 W RF powered thrusters [13] to 1 GW fusion rockets [14]. Their ability to scale to high powers is largely due to their independence from
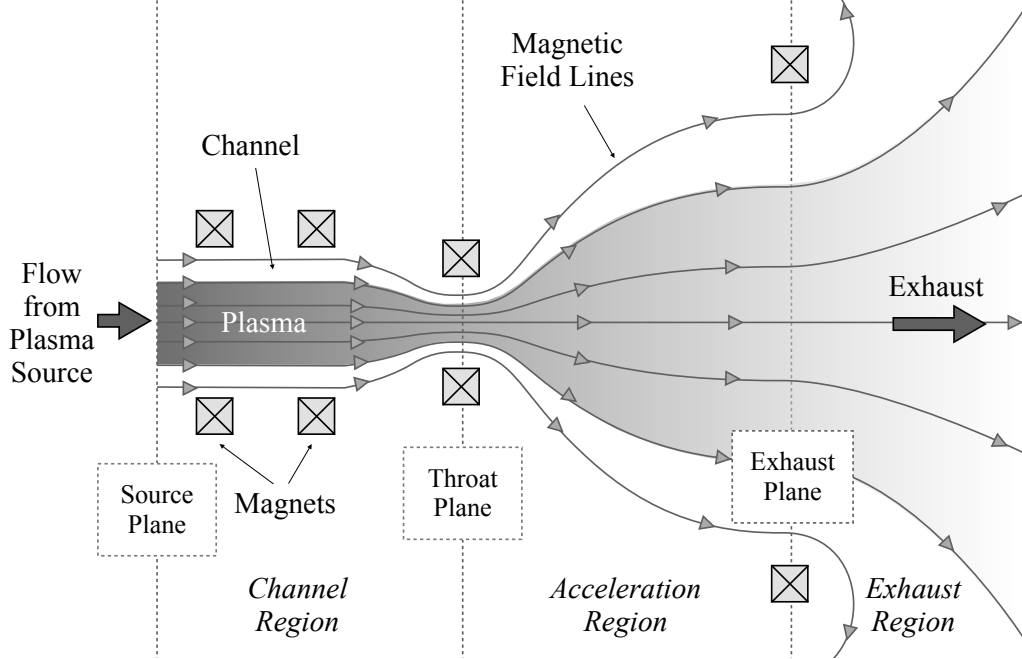
Figure 1.1: Example of a magnetic nozzle configuration. In our models, we define the magnetic nozzle as the region downstream from the throat plane, which can be further divided into an acceleration region and exhaust region. The channel connects the plasma source (not shown) with the magnetic nozzle.

electrodes, whose erosion typically limits the lifetime of high-power thrusters [15]. The magnetic field can be designed to shield the solid surfaces of the device from high energy particles to increase the lifetime [16] and efficiency [17] of the thruster. The added weight and complexity of a neutralizing hollow cathode is not required because the exhaust carries no net charge. Finally, they possess the ability to use various types of propellants, which may enable previously impossible missions via *in situ* utilization of resources found in space [18].

Considering the benefits that MNs possess for propulsion applications, it is no surprise that there has been great interest in the use of MNs by the electric propulsion community over the past few decades. In this time a large body of literature has emerged analyzing the various physical processes and performance of plasma flow through MN thrusters. Despite this large body of work, a key question remains:

Under what conditions is it possible to *efficiently* produce thrust by accelerating plasma through a magnetic nozzle? The central goal of this thesis is to answer the above question using analytical modeling and experimental techniques. Along the way to an answer, we will encounter problems that are important to the fundamental understanding of plasma expansion through diverging magnetic fields.

1.1 Magnetic nozzle classifications

Before answering the question posed above, it is necessary to limit the scope of the thesis. The low densities and high temperatures within a typical MN plasma can prevent thermal equilibrium among the various species [19]. Oftentimes the energization stage of the upstream plasma source targets a single species (e.g resonant wave heating [20, 21]). As a result, the plasma expansion will be driven primarily by the species that possesses the highest temperature. We define the term electron-driven magnetic
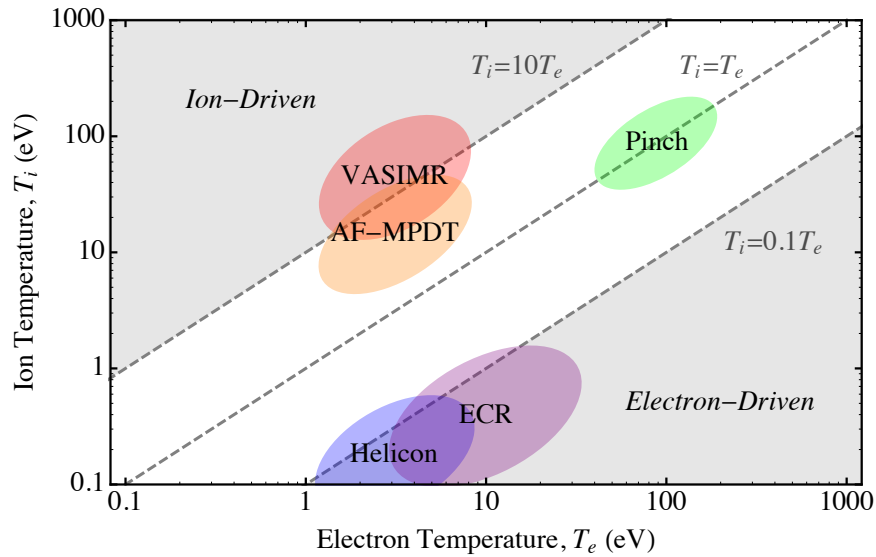
Figure 1.2: Schematic showing the different regimes of magnetic nozzle operation. Ion-driven magnetic nozzles are characterized by $T_i \gg T_e$. Alternatively, $T_e \gg T_i$ in electron-driven magnetic nozzles. The regime of magnetic nozzles commonly used in electric propulsion applications are highlighted.

nozzle (ED-MN) to describe MN plasma flow in which the electron temperature is much greater than the ion temperature, $T_e \gg T_i$. Alternatively, an ion-driven magnetic nozzle (ID-MN) satisfies $T_i \gg T_e$. Common examples of thrusters that utilize different types of MNs are shown in Fig. 1.2.

An electron-driven magnetic nozzle (ED-MN), the focus of this thesis, is characterized by the flow of a hot electron, cold ion plasma through a convergent-divergent magnetic field topology. The electrons, by virtue of their temperature, naturally expand through the nozzle at a rate greater than the ions. The tendency of the plasma to remain quasineutral leads to the formation of an ambipolar electric field [22, 23, 24], and under certain circumstances a current-free double layer (CFDL) [25, 26, 27] or quasineutral steepened layer (QSL) [28], which accelerates the cold ion population [29, 30]. Confinement of the thermal electrons by the magnetic field induces an azimuthal current density, or electron diamagnetic current, which is the primary mechanism of momentum transfer between the plasma and nozzle [31, 32]. For the sake of brevity, we will refer to the ED-MN simply as a MN throughout this thesis, and it should be noted that our results are valid primarily for plasma expansion satisfying $T_e \gg T_i$.

1.2 State of the art

The history behind the use of MNs for plasma acceleration closely follows the history of electrodeless electric propulsion systems. The earliest electrodeless thruster to be studied in depth was the Electron Cyclotron Resonance Thruster (ECRT) [33, 34, 35, 36, 37]. In an ECRT (Fig. 1.3), a microwave-energized plasma is accelerated through a MN. The magnitude of the magnetic field is chosen such that the frequency of the cyclotron motion of the electrons in the device couples with the frequency of the microwaves. Common values are $f = 2.45$ GHz and $B = 875$ G. The
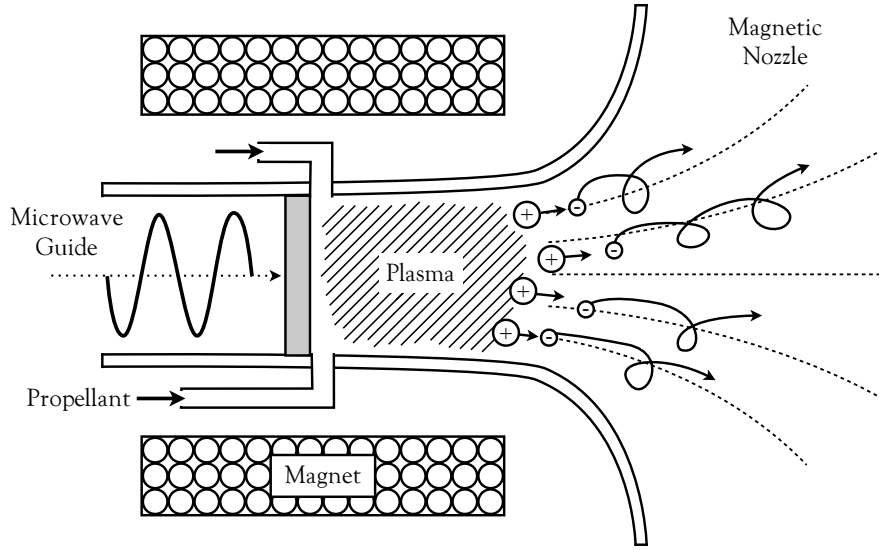
Figure 1.3: Schematic of the electron cyclotron resonance thruster (ECRT). Figure is adapted from [12].

resonance between the electromagnetic wave and particle motion leads to improved coupling between the power supply and propellant. Early experimental measurements indicated high levels of ionization and electron temperatures upwards of 30 eV [38]. Measurements of the power-coupling and MN efficiencies, however, reached only a fraction of their expected values.

Different variants of the ECRT have been proposed that also utilize MNs. The whistler-driven ECRT excites whistler waves in the plasma that propagate from a high B-field region to a low B-field region [39]. The waves are absorbed at the electron cyclotron resonance at the lower fields. This technique avoids the plasma density limitation of ECRTs due to the microwave cutoff at frequencies below the plasma frequency, and allows the plasma to be formed in regions of higher magnetic field, thus decreasing plasma losses to the walls of the device [40]. Recently, renewed interest in electrodeless EP systems has lead to the development of miniature [41]

and low-power [42] ECRTs that transmit power through coaxial lines as opposed to waveguides.

Helicon plasma discharges have recently received attention for their potential use as electric thrusters when combined with a MN. Developed by Boswell in 1970 [43], a helicon plasma is formed by adding a static magnetic field to a RF-excited plasma. The magnetic field allows propagation of the electromagnetic helicon wave, which is a type of whistler wave. The RF antenna, which may take many different shapes [44, 45], can be driven at frequencies between 100's of KHz and 10's of MHz. However, they are most commonly powered using standard 13.56 MHz RF power supplies. The helicon wave propagation allows energy to be absorbed further in the plasma as compared to inductive and capacitive discharges, for which absorption occurs within a few skin depths and in a thin sheath, respectively [46]. This allows high power-coupling efficiencies, high ionization percentages, and densities an order of magnitude larger than ECR discharges.

Electric propulsion systems that utilize helicon discharges typically take one of two forms: the Helicon Double Layer Thruster (HDLT) [29] or the Helicon Plasma Thruster (HPT) [47]. Each device relies on the expansion of a helicon plasma through a MN (Fig. 1.4). The distinction between the HDLT and HPT lies in the ion acceleration mechanism. In the HDLT, a significant portion of the ion kinetic energy is acquired in the strong electric field associated with the formation in the plasma of a current-free double-layer [29] (CFDL). A double layer (DL) is a non-neutral plasma structure, typically with a width of tens to hundreds of Debye lengths, that supports a strong electric field between two sheets of charge. A CFDL is a DL across which no current flows, which implies that the HDLT produces a neutral exhaust beam. Alternatively, ion acceleration in the HPT results from the ambipolar electric field formed in the wake of a thermally expanding electron population [24]. Although occurring in a much smaller region for the the HDLT, the potential drop associated with the
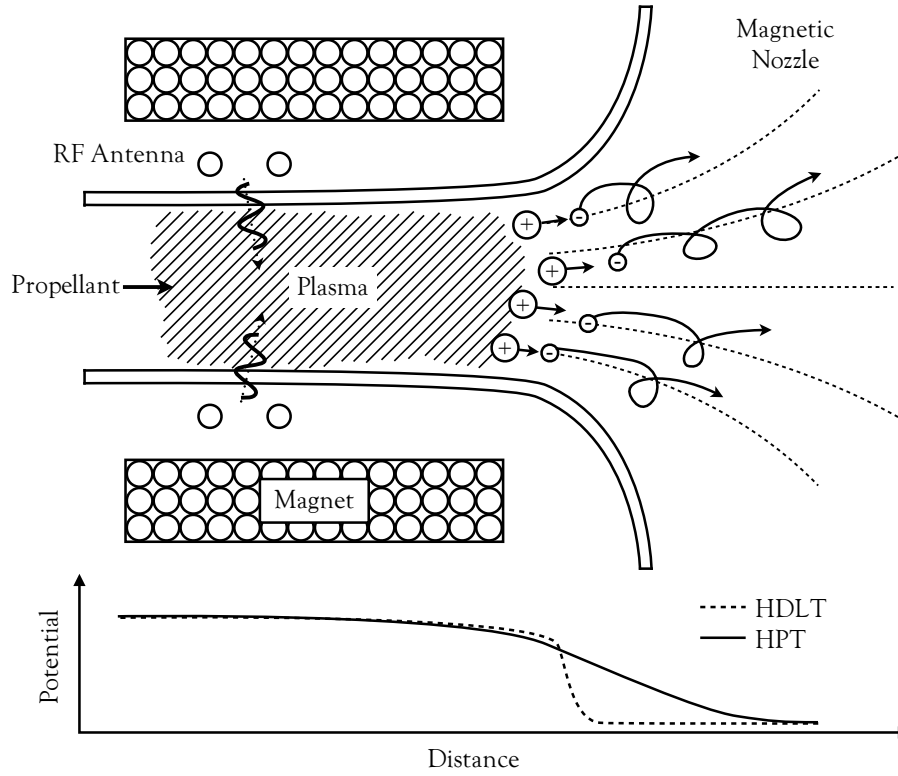
Figure 1.4: Schematic of the helicon double layer thruster (HDLT) and helicon plasma thruster (HPT). The main difference between the two similar devices is the length over which the potential drop occurs in the magnetic nozzle.

electric field in both configurations is believed to be comparable [48]. Because of the similarity of these devices, the exact cause for the formation of a CFDL is still a matter of debate [27, 49, 50], as are the possible benefits and downsides of the HDLT as compared to the HPT [28, 48, 50].

To date, MNs have not been flown in space. This is because they are still early in their development, with most of the proof-of concept research having been performed on bench top experiments. Devices have been designed to directly measure the performance MN thrusters. We will see in the next section, however, that vast improvements need to be made before they can be considered a competitive replacement to established electric propulsion technology.

1.2.1 Direct thrust measurements

The conventional method for characterizing the performance of an EP system is to measure the reaction force of the operating thruster using a mechanical thrust stand mounted inside a large vacuum chamber [51]. It is expected that, as the vacuum chamber pressure is reduced, the performance of the thruster approaches the expected performance in space [52]. This method has been used to successfully characterize both pulsed [53] and steady-state thrusters [54].

The two most common metrics for the performance of an electric thruster are the specific impulse and thrust efficiency [12]:

$$\text{Specific Impulse} = I_{\text{sp}} \equiv \frac{F}{\dot{m}g_0}, \tag{1.1}$$

$$\text{Thrust Efficiency} = \eta_T \equiv \frac{F^2}{2\dot{m}P}. \tag{1.2}$$

Here, F is the measured thrust, $\dot{m}$ is the total propellant flow rate, g_0 is the gravitational acceleration at sea level, and P is the total input power into the system. The I_{sp} is synonymous to the "gas mileage" of the thruster, while η_T quantifies the fraction of input power converted into thrust power.

Direct thrust measurements of MNs have been limited to the HDLT and HPT. Surprisingly, we were not able to find a single report on the measured thrust of an ECRT in the literature. This omission is likely due to the difficulty of mechanically coupling the microwave waveguide and thrust stand. While the ionization and heating processes for ECR-and-helicon-based thrusters are different, the literature implies that the expansion through the MN is fundamentally similar except for a small electron temperature anisotropy $(T_{e,\perp} \neq T_{e,\parallel})$ in the ECRT [38].

The earliest direct thrust measurements were performed on the HDLT. Independent measurements were made by Pottinger *et al.* [55], Takahashi *et al.* [56], and

Harle *et al.* [57] for $\dot{m} \sim 0.5 - 1.0$ mg·s^{-1} of argon, $P \sim 200 - 700$ W and applied field strengths up to 200 G. Each of these devices showed poor performance with $I_{\mathrm{sp}} \sim 100 - 300$ s and $\eta_T < 1\%$. Pottinger *et al.* found the mean velocity of the ion beam in the exhaust to be nearly five times the product $g_0 I_{\mathrm{sp}}$. From this, they concluded that the main source of inefficiency in the HDLT was a poor mass utilization efficiency. Because only a fraction of the incoming propellant was ionized and accelerated through the MN, the effective exhaust velocity of the thruster was much less than the ion beam velocity. In addition to improving the mass utilization efficiency, Takahashi *et al.* emphasized the importance of reducing the flux of plasma to the thruster walls for improved performance.

Early thrust measurements of the HPT also exhibited poor performance. For magnetic fields between $150 - 450$ G, the maximum specific impulse and thrust efficiency measured by Williams and Walker [58] were around 400 s and 1.5%, respectively, for an HPT operating with $\dot{m} \sim 1.5 - 4.5$ mg·s^{-1} of argon and $P \sim 200 - 850$ W . They attributed the low thrust efficiency to ionization losses because the energy of the ion beam was observed to be less than the expected energy cost to create each ion. While we will show that this is indeed an inherent problem with the HPT, the maximum thrust efficiency taking into account ionization losses was still an order of magnitude larger than the measured thrust efficiency. Based on the low densities measured within their thruster [59], the most likely source of inefficiency was a low mass utilization efficiency and poor coupling between the antenna and plasma. Operating near the same parameter space, similar results were found on a different HPT by Shabshelowitz and Gallimore [60].

The best HPT performance measured to date was by Takahashi *et al* [61]. His MN was formed using an array of permanent magnets with a peak strength of around 300 G. It was operated at 0.72 mg·s^{-1} of argon gas flow at RF powers between $0.3 - 2.0$ kW. Both the specific impulse and thrust efficiency were observed to increase with
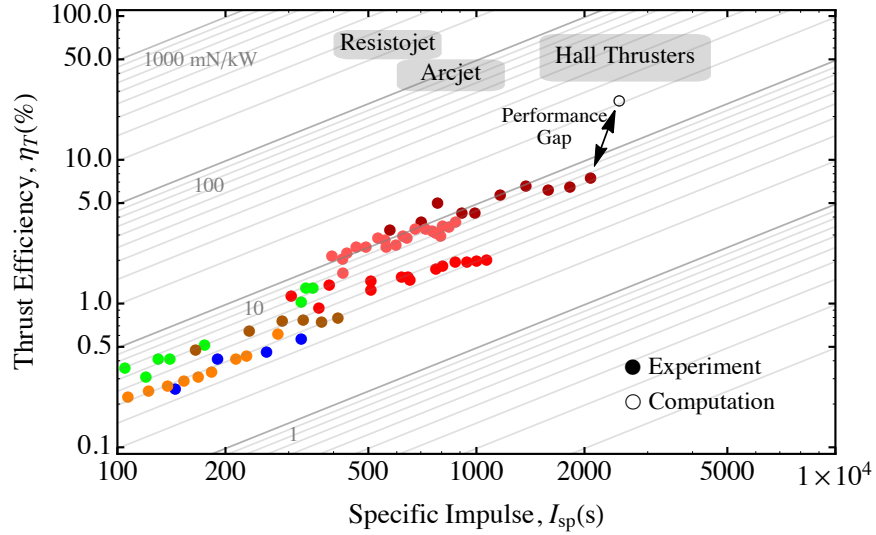
Figure 1.5: Measured (solid) and predicted (open) thrust efficiency vs. specific impulse for state of the art helicon plasma thrusters. Shaded regions show the approximate performance of established electric propulsion technology in a similar class ($0.5 - 5$ kW). Experimental measurements correspond to the following references: Green [58], Blue [60], Orange [55], Brown [66], Light Red [62], Red [32], Dark Red [61]. The computational data point comes from [17]

the RF power, and achieved maximum values of ~ 2000 s and $\sim 7.5\%$, respectively. According to their findings, further improvements may be realized by increasing the applied magnetic field strength [62] or adding a physical nozzle near the thruster exit [63]. It should be noted, however, that the vacuum chamber pressure during operation of these experiments was around 0.8 mTorr. This is nearly two orders of magnitude above the pressure at which facility effects become negligible [64], which may have artificially augmented the measured performance [65]. In addition, the vacuum chamber used to take these measurements (60 cm diameter) is significantly smaller than the chambers used by Williams and Walker (4 m diameter) [58] and Shabshelowitz and Gallimore (6 m diameter) [60]. Because the thruster size is comparable among each experiment (~ 20cm diameter), the interaction between the exhaust plasma and the facility walls may play a role in the large discrepancy in measured performance among the different HPTs.

We compare in Fig. 1.5 the measured performance of MN thrusters to established low-power ($\sim 0.5 - 5$ kW) EP concepts. It is clear from this figure that significant performance improvements are required of the HDLT and HPT before they can be considered an alternative to existing technology. The observation that η_T increases with I_{sp} is a well-known trait of electric thrusters. In light of this fact, it seems that the fundamental limitation of MN thrusters that have been tested in the laboratory thus far is a low thrust-to-power ratio (< 20 mN/kW). The reason for this limitation requires a deeper understanding of the physical processes in MN plasmas.

1.2.2 Review of theoretical work

Theoretical modeling has produced much insight into the operation of electrodeless thrusters. Fruchtman [50] showed that DLs formed during plasma expansion do not impart a net momentum to the plasma. This result was later confirmed by Ahedo [48] using a three-species model for DL formation in which the plasma has an additional population of hot electrons. The implication of these models is that acceleration due to the DL of the HDLT has no advantage over ambipolar acceleration in the HPT. Rather, for a given stagnation temperature, the energy of the exhaust ions will be comparable. The main difference between the two thruster varieties is the length over which ion acceleration occurs. A two-dimensional model by Merino and Ahedo [28] indicates that this difference has a negligible effect on the resulting plume divergence.

Some of the earliest theoretical work on the use of helicon plasma sources for plasma propulsion was performed by Fruchtman [67, 68]. Using a collisionless model for the plasma source, he predicted that the main sources of inefficiency are the energy flux to the back wall of the thruster and ionization costs [67]. Extending this model to the collisional regime, he found that collisionality increases the thrust to power ratio but decreases the thrust efficiency [68]. Plasma losses to the radial walls and acceleration through a MN were not included in his models.

The first comprehensive model of a HPT including radial and axial wall losses, collisionality, ionization, and ion acceleration in the MN was derived by Ahedo and Navarro-Cavallé [17]. They found that efficient operation requires magnetic fields and electron temperatures large enough to ensure that the ionization frequency greatly exceeds both the wall-recombination and ion-neutral collision frequencies. They also observed a sharp increase in the mass utilization efficiency at a critical value of the magnetic field. Performance degradation occurred from plasma losses to the rear wall of the thruster and incomplete expansion in the MN. Accounting for these losses, the predicted specific impulse and thrust efficiency were around 2500 s and 25%, respectively. The predicted performance from the theoretical model of Ahedo and Navarro-Cavallé is shown along with the experimental performance data in Fig. 1.5. A clear performance gap exists between the predicted and observed behavior of HPTs. Even if this gap is overcome, the theoretical thrust efficiency is expected to be nearly half that of established electric propulsion technology. However, Ahedo and Navarro-Cavallé explain that it may be possible to increase η_T to a competitive level by shielding the rear wall and recovering a larger amount of thermal energy during expansion through the MN.

Detailed models of plasma expansion in the divergent MN field have been used to elucidate phenomena associated with plasma acceleration and detachment. Using a two-fluid plasma model, Ahedo and Merino [23] characterized plasma flow through two different MN geometries and various applied magnetic field strengths, and derived key analytical expressions for the electron behavoir. They calculated efficiency losses around $20 - 40\%$ resulting from the divergence of the exhaust plume, and observed the plume divergence to decrease with the magnetic field divergence and increase with the applied magnetic field strength. The radial density profile of the incoming plasma had a strong influence on the plume divergence, with a smaller divergence calculated for a profile that was peaked towards the centerline of the MN. In a later

study [7], they used the results from their model to critically review different plasma detachment theories. It was concluded from their analysis that many of these theories are unsuitable to explain inward (with respect to the diverging magnetic field) detachment of a magnetized, thermally expanding plasma. Extensions of their model examined plasma demagnetization due to finite electron Larmor radius effects [69], ion detachment from the MN in the far-field region [9], and the effect of different thermodynamic models on the structure of the exhaust [70].

1.3 Impact of present work

In light of the poor measured performance of MN thrusters, and guided by the important theoretical contributions to the understanding of these devices, we seek to answer in this thesis the following question: Under what conditions, if any, is it possible to produce thrust with a magnetic nozzle at an efficiency that rivals established electric propulsion technology?

Throughout our analysis we will emphasize the influence of the fundamental plasma dynamics on MN performance. By normalizing the thrust, F, and specific impulse, I_{sp}, of the system by the mass flow rate, $\dot{m}$, and ion acoustic speed, c_s, we can separate the effect of different loss processes on the overall performance:

$$C_T \equiv \frac{F}{\dot{m}c_s} = \eta_m g_u \cos\theta_{\mathrm{div}}, \tag{1.3}$$

$$\hat{I}_{\mathrm{sp}} \equiv \frac{g_0 I_{\mathrm{sp}}}{c_s} = C_T, \tag{1.4}$$

$$\eta_T \equiv \frac{F^2}{2\dot{m}P} = \eta_m \eta_{\mathrm{ps}} \eta_c \eta_{\mathrm{mn}}. \tag{1.5}$$

Here, the thrust coefficient, C_T, represents the addition thrust force, and $g_u \equiv u_{\mathrm{ex}}/c_s$ represents the ion velocity increment achieved in the MN. The mass utilization effi-

ciency is defined as the ratio of the ion mass flow rate to the total propellant mass flow rate, $\eta_m \equiv \dot{m}_i/\dot{m}$, assuming that the thrust contribution of unionized propellant is negligible. The divergence half-angle, θ_{div}, accounts for losses due to undirected kinetic energy in the exhaust. Finally, η_{ps}, η_c, and η_{mn} are the plasma source, channel, and magnetic nozzle efficiencies, respectively, which account for power lost in each of these regions, and will be defined in more detail later in the thesis.

Through this simple analysis, we find that the performance of a MN can be understood in terms of six metrics: η_m, g_u, θ_{div}, η_c, η_{mn}, and η_{ps}. With these metrics as a guide, our aim is to use theoretical modeling and experimental measurements to elucidate the underlying plasma processes that dictate MN performance. From this understanding, we will develop simple scaling laws that capture the important physics and define the regimes for which efficient thrust production is possible.

1.4   Thesis structure

Chapter 2 begins with a discussion of the theoretical aspects of MN operation. We derive a 1D performance model to examine the scaling of the channel and MN efficiencies with the plasma parameters. We then proceed to derive an analytical solution to the 2D plasma expansion model for MN flow in the divergent magnetic field region, and use this solution to examine the influence of the properties of the outgoing plasma flow on the divergence of the plume. We describe in Chapter 3 the experiment and diagnostics used throughout the remainder of the thesis. In Chapter 4, we characterize the effect of the applied magnetic field strength on confinement in the MN plasma source and channel, and find a critical condition for plasma confinement that must be met in order to maximize the mass utilization efficiency. We focus in Chapter 5 on the electron thermodynamics in the expanding plasma and their influence on the exhaust velocity increment in the MN. Finally, in Chapter 6 we examine the role of

the applied magnetic field strength on the divergence of the exhaust, and find a transition from an under-collimated exhaust at low fields to a collimated exhaust at high fields. We finish in Chapter 7 with a summary of our key findings and a discussion of future avenues of research.

Chapter 2

Performance Model

The primary loss mechanisms for electric propulsion systems that use MNs for plasma acceleration are low mass utilization [55], poor plasma confinement [71], unrecovered excitation and ionization energies [58], and exhaust plume divergence [60]. Using theoretical models of varied complexity [17, 72], detailed analyses have been done on the influence of the operating conditions (mass flow rate, applied magnetic field strength, power) on the performance of MN thrusters. Missing from the literature is a MN model that encompasses all of the relevant loss mechanisms, yields simple, albeit approximate, algebraic scaling laws, and is applicable over a wide range of operating conditions.

The goal of this chapter is to develop an approximate, yet comprehensive theoretical model for the plasma channel and MN regions. We focus on the observation by Ahedo and Navarro-Cavallé [17] of the existence of a critical magnetic field strength for efficient plasma confinement, and search for a dimensionless parameter that governs its value. In light of the interplay between ionization, wall recombination, and charge exchange collisions, we attempt to understand how the absence of perfect confinement influences the optimal channel length. Furthermore, we focus on fundamental questions of great practical interest that have thus far eluded theoretical

models; specifically, *is there an optimal temperature range?* And, *what is the best propellant?* Ultimately, we seek algebraic scaling laws that allow us to examine the theoretical performance limitations of MNs for plasma propulsion.

2.1 Plasma channel model[1]

A number of theoretical models exist in the literature for the plasma dynamics within the cylindrical chamber of a MN thruster [17, 67, 72, 74]. While these models were developed to describe a Helicon plasma source, they exclude the power coupling between the helicon antenna and plasma, thus making their results applicable to a general channel flow of an axially magnetized plasma. Each model considers the plasma as a two-species (ions and electrons), quasineutral fluid. Fruchtman *et al.* [74] consider an axisymmetric, 2D model (r-z) that includes the continuity and momentum conservation equations for each species. They simplify the problem to a set of five ordinary differential equations using an approximate variable-separation technique [75] to decouple the radial and axial equations of motion. They close the equations by assuming the electron temperature, T_e, is constant everywhere, and is an eigenvalue determined by the global particle balance. The plasma density, n, is determined by a global power balance. Assuming perfect confinement of the plasma, they examine three asymptotic solutions that correspond to different axial ion transport regimes, and compare their results to experimental data.

Ahedo and Navarro-Cavallé [17] also use the variable-separation technique, but include plasma recombination at the chamber walls, a detailed spatial model for the neutral density, and inertial forces in the radial momentum equations. Furthermore, they consider a regime where the ion dynamics are influenced mainly by ambipolar electric fields as opposed to collisional diffusion. They couple the plasma dynamics in

---

[1]This section is an extension of the theoretical model presented in [73]: J. M. Little and E. Y. Choueiri, "Critical Condition for Plasma Confinement in the Source of a Magnetic Nozzle Flow," *IEEE Trans. Plasma Sci.*, Vol. PP, no. 99, 2014.

the chamber to a separate model for the expansion of the plasma through a MN. Also assuming constant T_e, they are required to terminate the MN plume at a conducting wall to avoid the singularity associated with isothermal expansion [76]. They condense the eight partial differential equations of the two-fluid model into a more manageable set of three ordinary differential equations, and derive asymptotic solutions for the radial and axial dynamics that provide fundamental insight and yield useful scaling laws. Contrary to Fruchtman *et al.*, they find n to be determined by the mass balance and T_e to be determined by the power balance.

Recently, Lafleur [72] developed a theoretical model to help explain experimental performance trends obtained using thrust stand measurements of an HPT [61, 77]. Lafleur's model consists of a quasi-1D approximation to the two-fluid equations that accounts for particle, momentum, and energy balance. A semi-empirical model is used for the radial plasma density profile, which is assumed to remain self-similar through the channel and MN regions. Because collisions are neglected, ion recombination at the channel wall is dominated by collisionless Bohm diffusion. T_e is assumed constant throughout the channel and MN. The isothermal expansion singularity is avoided by assuming the plasma detaches from the MN when the ion Larmor radius equals the local radius of the plume. By specifying a value for the mass utilization efficiency, a relatively simple iterative procedure is used to find T_e, n, the total required power, the ion Mach number at the point of detachment, and the thrust. From these quantities, the specific impulse and thrust efficiency are easily obtained.

With the exception of certain asymptotic regimes, these theoretical models require either an exact numerical solution to a set of ordinary differential equations [17, 74], or an iterative solution to a set of algebraic equations [72]. In regards to the predicted performance of MN thrusters, this requirement limits the above models to parametric investigations in which one or more design parameters are held constant. Our goal here is to obtain closed-form algebraic solutions to the fluid equations used in previous
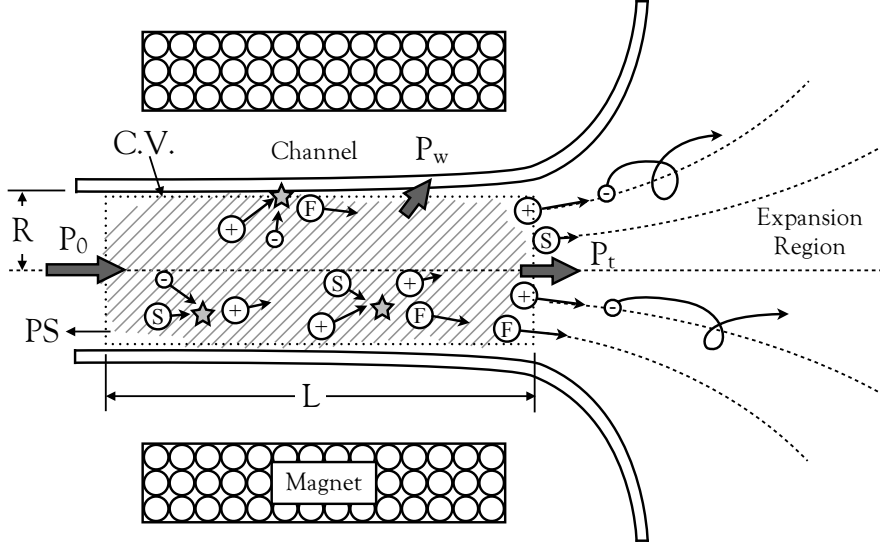
Figure 2.1: Geometry of the magnetic nozzle model. The channel control volume (C.V.) consist of the region downstream from the plasma source (PS) and upstream from the magnetic nozzle (MN) throat. The flux of power from the PS to the channel, P_0, is divided into power lost to the channel walls, P_w, and power into the MN throat, P_t. Particle balance within the channel is governed by ionization, wall recombination, and charge exchange processes. Particles are labelled as: (S) slow neutrals, (F) fast neutrals, (+) ions, (-) electrons.

models by employing a number of simplifying approximations. We note that we do not add additional physics to the plasma dynamics models described above, but rather condense the behavior observed from these models into a more manageable, albeit less accurate form. As we will demonstrate, a solution of this form is highly valuable for understanding the relative importance of different loss processes, and can be used to derive simple scaling laws for the performance of MN thrusters.

2.1.1 Channel model formulation

A MN thruster can be thought of as having three distinct regions (Fig. 2.1): (1) a plasma source (PS) where most of the external power is absorbed, (2) a channel

where additional propellant ionization occurs,[2] and (3) the MN where thermal energy is converted into kinetic energy. To maintain generality, we depart from previous models by separating the PS and the channel regions. Indeed, one of the main criticisms of these models is their lack of a self-consistent description between the external source of power and the plasma dynamics. Instead, we assume that the external source of energy, whether it be from wave heating or some other mechanism, produces a partially ionized plasma upstream from the channel. We assume the ions remain singly ionized with charge $+e$. Furthermore, we posit that all of the external power is absorbed in the PS region with a given efficiency, η_{ps}. From the PS flows into the channel an ion mass flow rate, $\dot{m}_{i,0}$, and power, P_0. Although these quantities represent two extra degrees of freedom into our model, they reflect the fact that MNs are a general means of plasma acceleration, and can be used with various types of plasma discharges.

We consider a cylindrical channel of radius R and length L with a uniform magnetic field directed along the axis of symmetry (Fig. 2.1). We assume that the plasma thermal energy density is much less than the energy density of the applied magnetic field, written symbolically as

$$\beta \equiv \frac{n k_b T_e}{B^2/2\mu_0} < 1. \tag{2.1}$$

With $\beta < 1$ we can ignore perturbations to the magnetic field due to the presence of internal currents within the plasma, which are predicted to deteriorate plasma confinement and increase wall losses [78].

For simplicity, we ignore the momentum equation of the plasma and concentrate solely on the mass balance in the chamber and its implications on the global power balance. We are allowed to do this because we know that the ion velocity at the channel wall and exit are predetermined by the Bohm and sonic conditions, respectively.

---

[2]In previous models [73] we have referred to the channel as the magnetic nozzle plasma source because the channel plasma flows into the MN. We avoid this nomenclature here to avoid confusion with the region in which the plasma is initially formed.

As a consequence of this approximation, and in contrast to the models of Fruchtman *et al.* [74] and Ahedo and Navarro-Cavallé [17], we are not able to determine the detailed 2D profile of the plasma parameters in the channel. Therefore, the prescribed value of the parameters in our model ultimately represent an effective average over the length of the channel.

Following Fruchtman [68], we account for the plasma ions, and a slow and fast population of neutral particles. Particle balance along the length of the channel is governed by collisional ionization and charge exchange (CEX) processes. We extend Fruchtman's model to include the effect of the ion flux to the channel wall. The quasi-1D mass conservation equations may be written as,

$$\frac{d\dot{m}_i}{dz} = m_i R_{\text{ion}}(n_s + n_f)n_i A - m_i \Gamma_w, \tag{2.2}$$

$$\frac{d\dot{m}_s}{dz} = -m_i(R_{\text{cex}} + R_{\text{ion}})n_s n_i A + m_i \alpha_w \Gamma_w, \tag{2.3}$$

$$\frac{d\dot{m}_f}{dz} = m_i(R_{\text{cex}} n_s - R_{\text{ion}} n_f)n_i A + m_i(1 - \alpha_w)\Gamma_w, \tag{2.4}$$

where $\dot{m}_i$, $\dot{m}_s$, and $\dot{m}_f$ are the mass flow rates of the ions, slow neutrals, and fast neutrals, respectively, and are subject to the constraint $\dot{m} = \dot{m}_i + \dot{m}_s + \dot{m}_f$. Similarly, n_i, n_s, and n_f are the ion, slow neutral and fast neutral densities, respectively. The ionization rate coefficient is denoted R_{ion} and the CEX collision rate is given by R_{cex}. Here, $A = \pi R^2$ is the cross-sectional area of the channel. The ion flux to the wall, Γ_w, creates either slow neutrals or fast neutrals depending on the wall accommodation coefficient, $\alpha_w \in [0, 1]$. We note the inclusion of α_w in the above model is an overly simple approximation for wall accommodation, but it captures the main effect of neutral creation through ion recombination at the wall.

We assume the residence time of the fast neutrals in the channel is much shorter than the slow neutrals, which results in $n_f \ll n_s$. This allows us to drop the fast

neutral contribution to the ionization terms because the fast neutrals leave the plasma source before undergoing further collisions. The low pressure within the plasma source implies $\alpha_w \ll 1$ [79], therefore we assume that ion recombination at the channel wall produces fast neutrals that immediately leave the device. Under these assumptions, Eqs. (2.2)-(2.4) simplify to

$$\frac{d\dot{m}_i}{dz} = \dot{m}_s / L_{\text{ion}} - m_i \Gamma_w, \tag{2.5}$$

$$\frac{d\dot{m}_s}{dz} = -\dot{m}_s \left(1/L_{\text{ion}} + 1/L_{\text{cex}} \right), \tag{2.6}$$

$$\frac{d\dot{m}_f}{dz} = \dot{m}_s / L_{\text{cex}} + m_i \Gamma_w, \tag{2.7}$$

where $L_{\text{ion}} \equiv v_s / (R_{\text{ion}} n)$ and $L_{\text{cex}} \equiv v_s / (R_{\text{cex}} n)$ are the modified mean free paths for ionization and CEX collisions, respectively. To obtain these terms, we used the relation $n_s m_i A = \dot{m}_s / v_s$, where v_s is the speed of the slow neutrals. Furthermore, we have assumed the plasma remains quasineutral, and defined the plasma density, n, such that $n = n_i = n_e$.

The ion flux to the wall may be written as $\Gamma_w = -D_\perp (\partial n / \partial r)_{r=R_s}$ [80], where $D_\perp$ is the cross-field diffusion coefficient and $(\partial n / \partial r)_{r=R_s}$ is the radial plasma density gradient at the sheath. We consider sheaths with thicknesses that are small compared to the channel radius, or $R_s \approx R$. We decompose n into its value along the centerline, $n_{r=0}$, and a shape function, f_n, such that $n = n_{r=0} f_n$. We take $h_w = (\partial f_n / \partial r)_{r=R_s}$, and rewrite $n_{r=0}$ in terms of the local ion mass flow rate, $n_{r=0} = \dot{m}_i / (h_n m_i c_s A)$. Here, $h_n = \int f_n dA / A$ is the normalized density profile cross-sectional average.

With these simplifications, the second term on the right-hand side of Eqs. (2.5) and (2.7) may then be written as

$$m_i \Gamma_w = \frac{\dot{m}_i}{L} \left(b / Pe_{\text{an}} \right). \tag{2.8}$$

22

where $b = h_w/(\pi h_n)$ is a constant depending only on f_n. We have introduced the dimensionless, anisotropic Péclet number, which we define as,

$$Pe_{\mathrm{an}} \equiv \frac{c_s/L}{D_\perp/R^2}. \tag{2.9}$$

This parameter reflects the relative importance of field-aligned advection with respect to cross-field diffusion on the global particle balance within the channel. Effectively, Pe_{an} is the ratio of the cross-field diffusion timescale to the field-aligned advection timescale. We note that we have not yet specified a form for $D_\perp$.

2.1.2 Mass utilization efficiency scaling

To gain insight into the fundamental physics governing the performance of the channel, we simplify the problem by seeking a solution to Eqs. (2.5)-(2.7) assuming that L_{ion}, L_{cex}, and Pe_{an} remain constant throughout the flow. We further assume self-similarity of the density profile, or $\partial f_n/\partial z = 0$. The solution to Eqs. (2.5)-(2.7) under these assumptions yields

$$\eta_m = \left[\frac{1 + \eta_{m,0}(\Pi - \Psi)}{1 + \Pi - \Psi}\right] e^{-\Psi\Lambda} - \left(\frac{1 - \eta_{m,0}}{1 + \Pi - \Psi}\right) e^{-(1+\Pi)\Lambda}. \tag{2.10}$$

Here, $\eta_{m,0} = \dot{m}_{i,0}/\dot{m}$ and $\eta_m = \dot{m}_{i,L}/\dot{m}$ represent the mass utilization efficiency at the channel entrance and exit, respectively.

The solution in Eq. (2.10) depends upon three dimensionless parameters that embody the physical processes governing particle balance in the channel:

Ionization Parameter, $\Lambda \equiv L/L_{\mathrm{ion}} = f_\Lambda(n, T_e, \mathrm{Gas})$

The ionization parameter is defined as the ratio of the channel length to the effective ionization mean free path. It is a measure of the probability of a slow neutral to become ionized before transiting the length of the channel. In

23

addition to the propellant type, it is a function of the ion density and electron temperature.

Neutral Pumping Parameter, $\Pi \equiv L_{\rm ion}/L_{\rm cex} = f_\Pi(T_e, {\rm Gas})$

The neutral pumping parameter is defined as the ratio of the ionization mean free path to the CEX mean free path. It can be viewed as a measure of the rate at which slow neutrals are lost, or pumped, from the device due to CEX collisions with respect to the loss rate due to ionization. It depends primarily on the electron temperature and propellant gas.

Confinement Parameter, $\Psi \equiv (b/Pe_{\rm an})\,/\Lambda = f_\Psi(n, T_e, B, {\rm Gas})$

The confinement parameter represents the rate at which ions are lost to wall recombination normalized by the rate at which they are produced through collisional ionization. We refer to the ratio of these two rates as the confinement parameter because the flux of ions to the wall results from imperfect radial confinement of the plasma. Perfect confinement occurs for $\Psi = 0$. The confinement parameter depends on the ion density, electron temperature, magnetic field strength, and propellant type.

As expected, an additional dependence on $\eta_{m,0}$ is also observed. This dependence reflects the limitation of our model to the regions downstream from the plasma source (i.e downstream from where the external power is absorbed). A detailed model of the coupling mechanism between the external power supply and source plasma is required to eliminate this free parameter. Because power can be coupled to the plasma through various means, this region is beyond the scope of our model.

We can use Eq. (2.10) to gain qualitative understanding of the scaling of the mass utilization efficiency with the above dimensionless parameters. In agreement with the analysis of Ahedo and Navarro-Cavallé [17], the desire to have a channel much longer than the ionization mean free path ($\Lambda \gg 1$) to ensure full utilization of the neutral

propellant is reflected in the exponent of the second term. The exponent of the first term indicates that a long channel is not always desirable, especially for circumstances where poor plasma confinement may lead to an appreciable flux to the channel walls. Finally, the device should be operated under conditions such that $\Pi \ll 1$ to ensure ionization of the propellant as opposed to CEX expulsion from the device.

The solution implies that there exists two regimes of operation based on the level of confinement in the channel. We denote these regimes as the low confinement regime and the high confinement regime:

Low Confinement: $\Psi < 1$ & $\Psi\Lambda \sim 1$

Low confinement is characterized by channel flow in which wall losses, while not dominant, play an important role on length scales comparable to the ionization mean free path. Using a contour plot of η_m as a function of Λ and Π, we show in Fig. 2.2(a) that a balance exists within this regime with respect to the channel length. If the channel is too short the neutral propellant does not have sufficient time for an ionizing collision to occur before traveling the length of the channel. On the other hand, if the channel is too long, the rate at which ions are lost to the wall increases beyond the ionization rate. The importance of this balance depends on the role of CEX collisions within this device, as highlighted from the transition from nearly vertical contour lines to horizontal contour lines with decreasing values of Π.

We solve Eq. (2.10) for the value of Λ that maximizes η_m. This value, from which an optimum channel length can be found in terms of the expected plasma parameters, takes the form

$$\Lambda_{\mathrm{lc}}^* = \frac{1}{1+\Pi-\Psi} \ln\left\{ \frac{(1-\eta_{m,0})(1+\Pi)}{\Psi\left[1+\eta_{m,0}(\Pi-\Psi)\right]} \right\} \approx \frac{\ln\left[(1-\eta_{m,0}\Pi)/\Psi\right]}{1+\Pi}. \qquad (2.11)$$
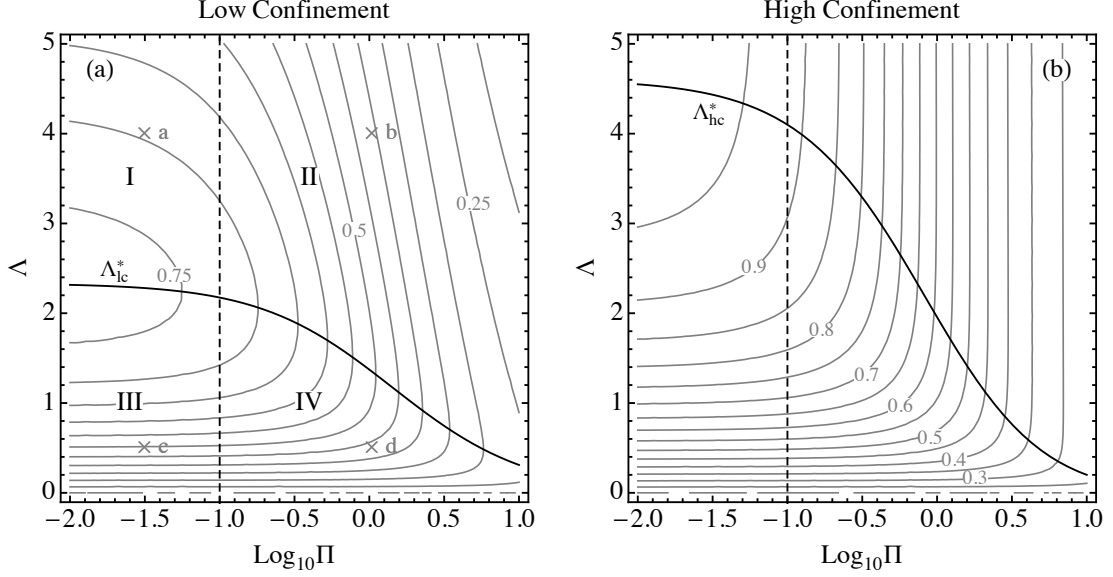
Figure 2.2: Contour plot of the mass utilization efficiency, η_m, as a function of the ionization, Λ, and neutral pumping, Π, parameters for the (a) low confinement and (b) high confinement regimes. The roman numerals in (a) denote the four regions described in the text, while the crosses correspond to Figs. 2.3(a)-(d). The solid black lines represent the critical channel length for low and high confinement, Λ_{lc}^* and Λ_{hc}^*, respectively. Here, we take $\eta_{m,0} = 0.2$ to corresponds to an ionization fraction representative of helicon [44, 81, 82] and ECR [83, 84] plasma sources.

This equation is plotted along with the η_m-contours in Fig. 2.2(a). We note that the approximation on the right hand side is valid for $\Pi < 1$.

It is apparent from Fig. 2.2(a) that four regions of operation exist depending on the length of the channel with respect to the optimum value and the relative importance of CEX collisions:

I. $\Lambda > \Lambda_{lc}^*$ & $\Pi < 0.1$ Channel too long, CEX not important

II. $\Lambda > \Lambda_{lc}^*$ & $\Pi > 0.1$ Channel too long, CEX important

III. $\Lambda < \Lambda_{lc}^*$ & $\Pi < 0.1$ Channel too short, CEX not important

IV. $\Lambda < \Lambda_{lc}^*$ & $\Pi > 0.1$ Channel too short, CEX important

26

We plot in Fig. 2.3 the evolution of the mass flow rates of the ions, slow neutrals, and fast neutrals for each of the above regions as a function of distance within the channel to demonstrate their fundamental differences. Channel flow characteristic of region I is shown in Fig. 2.3(a). Here, the channel is clearly too long as the ion mass flow reaches a maximum about halfway along the length of the channel. Ion wall recombination dominates ionization beyond this maximum, which results in a steady increase in the mass flow of fast neutrals. Region II flow, Fig. 2.3(b), is similar to region I in that the ion mass flow reaches a maximum and then starts to decrease along the length of the channel. This maximum is shifted upstream because the CEX collisions result in the increased depletion of slow neutrals compared to region I flow. The combined effect of CEX collisions and wall recombination results in a greater amount of fast neutrals emerging from the channel. The channel in region III is
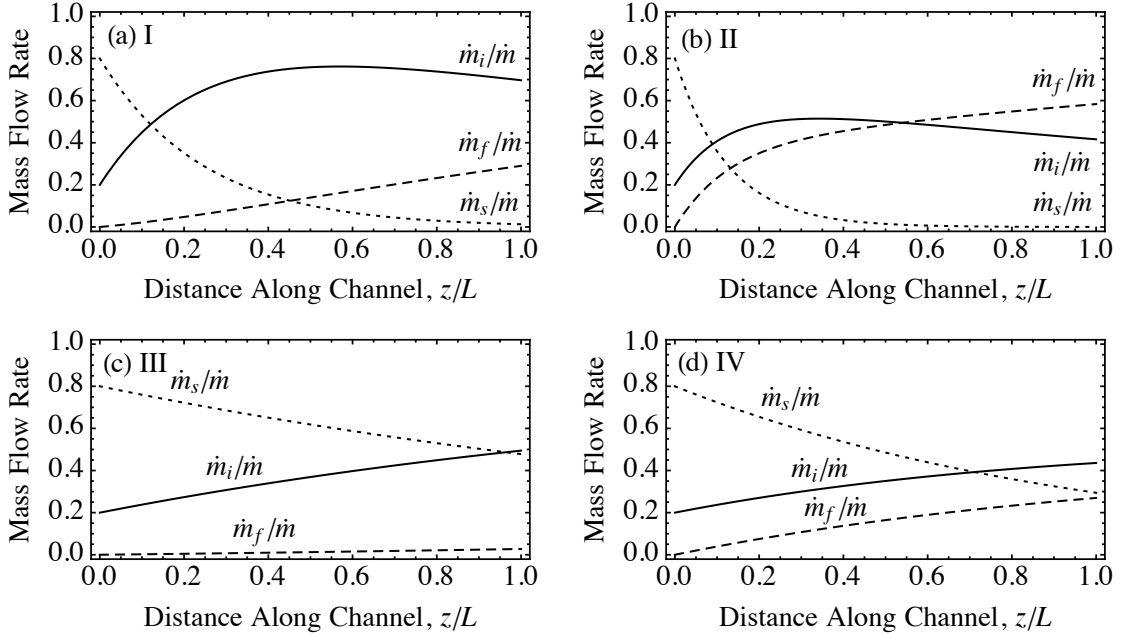
Figure 2.3: Relative mass flow rate of ions, $\dot{m}$, fast neutrals, $\dot{m}_f$, and slow neutrals, $\dot{m}_s$, as a function of distance along the channel for (a)-(d) different regions of operation in the low confinement regime. Here, we take $\eta_{m,0} = 0.2$ to corresponds to an ionization fraction representative of helicon [44, 81, 82] and ECR [83, 84] plasma sources.

simply not long enough to fully ionize the incoming propellant, as seen in Fig. 2.3(c). Finally, Fig. 2.3(d) demonstrates that, in addition to incomplete ionization of the incoming propellant, the role of CEX collisions on the short channel is to deplete the slow neutral population in favor of fast neutrals, which serves to decrease the ionization rate of the incoming propellant along with the ion mass flow rate.

Eq. (2.11) indicates that Λ_{lc}^* increases with decreasing Ψ, resulting in an upward shift of the solid line in Fig. 2.2(a). This implies that the optimum channel length increases as the plasma becomes more confined. As confinement increases, the behavior of the plasma reaches a point that η_m becomes relatively insensitive to the length of the channel. We refer to this as the high confinement regime.

High Confinement: $\Psi\Lambda \ll 1$

The high confinement regime [Fig. 2.2(b)] is characterized by increased η_m and an insensitivity to the channel length beyond a critical value of Λ. Although the maximum of η_m is still achieved at Λ_{lc}^*, it is not desirable from an engineering standpoint to design a channel to meet this requirement because it could lead to excessively large devices. Indeed, $\Lambda_{lc}^* \to \infty$ as $\Psi \to 0$.

It can be shown that the critical value of Λ scales approximately as

$$\Lambda_{hc}^* = -\frac{\ln\left[c(1+\Pi)\right]}{1+\Pi},\tag{2.12}$$

where $c \approx 0.01$ is a constant. We show the variation of Λ_{hc}^* with Π in Fig. 2.2(b) along with the lines of constant η_m. It is clear from this figure that Λ_{hc}^* marks the upper boundary of a region in which the η_m-contours transition from primarily horizontal (sensitive to Λ) to primarily vertical (insensitive to Λ).

For operation in the high confinement regime, the length of the channel should satisfy $\Lambda \geq \Lambda_{hc}^*$. With this inequality satisfied, the maximum mass utilization efficiency

may be estimated from

$$\eta_{m,\text{hc}} = \frac{1 + \eta_{m,0}\Pi}{1 + \Pi}, \qquad (2.13)$$

where we have found this result by solving Eq. (2.10) for η_m in the limit $\Psi\Lambda \ll 1$ and $\Lambda \gg 1$. It is clear from Eq. (2.13) that full propellant utilization is only possible if either the incoming plasma is fully ionized or CEX collisions are negligible. We will analyze these requirements in further detail in the next section.

We note that Ahedo and Navarro-Cavallé [17] derive a closed-form analytical solution for a subset of the high confinement regime in the limit $\Pi \ll 1$. From this solution, they find an implicit relation between η_m and Λ. Considering the asymptotic limit of Eq. (2.10) for $\Psi \ll 1$, $\Pi \ll 1$, and $\eta_{m,0} \ll 1$, we find from our model that $\eta_m = 1 - e^{-\Lambda}$. It can be shown that this expression agrees well with the results of Ahedo and Navarro-Cavallé for $\Lambda > 1.5$. Agreement with the detailed model of Ahedo and Navarro-Cavallé gives us confidence that, despite the large number of approximations that we employ, our model is able to analyze the relevant plasma processes in the MN channel.

2.1.3 Channel efficiency scaling

We are now in a position to examine the scaling of the MN channel efficiency. Multiple definitions for the efficiencies of the different regions of a MN thruster exist in the literature [17, 68, 85]. One of the primary differences among these definitions is the region to which ionization losses are attributed. Ahedo and Navarro-Cavallé [17] attribute these losses to the plasma chamber, which within their model combines the plasma source and channel regions. Because the internal energy contained within the ionization modes of the plasma can in principle be recovered in the MN, we choose instead to divide the ionization losses between the channel and MN regions according to the flux of plasma to the channel walls and through the exit of the device,

respectively. In other words, ionization energy lost to the channel wall represents a loss mechanism of the channel region. Ionization energy lost to the plume, commonly referred to as a frozen-flow loss, represents a loss mechanism of the MN region.

With this distinction in mind, we define the channel efficiency, η_c, as the ratio of the power emerging from the channel, P_L, to the incoming power, P_0. This can be written symbolically as

$$\eta_c \equiv \frac{P_L}{P_0} = \frac{1}{1 + P_w/P_L}. \tag{2.14}$$

Here, P_w represents the power lost to the channel wall, and we have used the fact $P_0 = P_w + P_L$. The channel efficiency is then governed by the ratio P_w/P_L. We note that η_c is equivalent to η_{cham} in Eq. (47) of Ref. [17], with the exception that only ionization losses to the channel walls are accounted for in η_c.

Here, we follow the approach of Sudit and Chen [86] to model the power lost through the interaction with the channel wall. Electron and ion fluxes to the insulating wall must remain equal to conserve quasineutrality. Each electron-ion pair will remove from the plasma an average amount of energy, which we denote $\epsilon_{ei,w}$. The total power removed from the plasma is then

$$P_w = \frac{\dot{m}_{i,w}\epsilon_{ei,w}}{m_i}, \tag{2.15}$$

where $\dot{m}_{i,w}$ is the ion mass flow rate to the wall. Each ion removes on average an energy equal to the sum of the kinetic energy acquired through the pre-sheath and sheath potential drops, and the effective ionization energy, $\epsilon_{i,w} = T_e/2 + (1/2)T_e \ln [m_i/(2\pi m_e)] + \epsilon'_{\text{ion}}$, where the effective ionization energy, ϵ'_{ion}, accounts for power lost to both ionization and excitation of the incoming propellant [87]. The average kinetic energy lost per electron entering the wall sheath is given by $\epsilon_{e,w} = 2T_e$. The total energy removed from the plasma per electron-ion pair is then $\epsilon_{ei,w} = \epsilon_{e,w} + \epsilon_{i,w}$.

The ion and electron fluxes from the channel must also remain equal. This will obviously change if we allow ions of higher charge states, but this is an added complexity that is beyond the scope of our simple model. The power emerging from the channel can be written

$$P_L = \frac{\dot{m}_{i,L} \epsilon_{ei,L}}{m_i},$$ (2.16)

where $\epsilon_{ei,L}$ is the average energy lost per electron-ion pair leaving the channel. The average energy loss per ion includes the kinetic energy of the ion and the effective ionization energy, $\epsilon_{i,L} = \gamma_e T_e/2 + \epsilon'_{\text{ion}}$. Here, we have used the fact that the ion fluid emerges from the channel at the ion acoustic velocity, $c_s = \sqrt{\gamma_e T_e/m_i}$, where γ_e is the electron polytropic exponent. The average energy loss per electron is $\epsilon_{e,L} = 5T_e/2 + m_i Q_e/\dot{m}_i$, where Q_e is the power lost to field-aligned electron heat conduction. The average energy removed from the plasma through the channel exit per electron-ion pair is then $\epsilon_{ei,L} = \epsilon_{e,L} + \epsilon_{i,L}$.

The ratio of the power lost to the wall to the power emerging from the channel takes the form

$$\frac{P_w}{P_L} = \mu_w \frac{\epsilon_{ie,w}}{\epsilon_{ie,L}},$$ (2.17)

with

$$\mu_w \equiv \frac{\dot{m}_{i,w}}{\dot{m}_{i,L}}.$$ (2.18)

Thus, the ratio P_w/P_L scales linearly with the ratio of the ion mass flow rate to the wall to the ion mass flow rate exiting the channel, μ_w.

We determine μ_w from our particle balance model, Eqs. (2.5)-(2.7). The ratio of the mass flow rates of fast neutrals created by ion recombination at the wall to the total fast neutral mass flow rate is given by

$$\frac{\dot{m}_{i,w}}{\dot{m}_{f,L}} = \frac{\Psi}{\Pi + \Psi}.$$ (2.19)

Using this equation, μ_w may be rewritten as

$$\mu_w = \frac{\dot{m}_{i,w}}{\dot{m}_{f,L}} \frac{\dot{m}_{f,L}}{\dot{m}_{i,L}} = \left(\frac{\Psi}{\Pi + \Psi} \right) \mu_f, \tag{2.20}$$

where

$$\mu_f \equiv \frac{\dot{m}_{f,L}}{\dot{m}_{i,L}} = \frac{(1 + \Pi - \Psi)\left[e^{(1+\Pi)\Lambda} - (1 - \eta_0) \right]}{\left[1 + \eta_0\left(\Pi - \Psi\right) \right] e^{(1+\Pi+\Psi)\Lambda} - (1 - \eta_0)} - 1, \tag{2.21}$$

represents the mass flow rate of fast neutrals relative to the mass flow rate of ions at

the channel exit.

Immediately we notice that the channel efficiency has a strong dependence on the

confinement parameter. In the limit of perfect confinement, $\Psi \to 0$, the ion flux and

power to the wall disappear, $\mu_w \to 0$ and $P_w/P_L \to 0$, and the channel efficiency

approaches unity, $\eta_c \to 1$. To determine how the level of confinement influences the

channel efficiency, we plot in Fig. 2.4 the scaling of η_m, η_c, and μ_w for varying Ψ

using Eqs. (2.10), (2.14), and (2.18), respectively. Here, we have taken $\Lambda = \Lambda_{\mathrm{lc}}^*$ and

$\Pi = 0.1$, and set arbitrarily $\epsilon_{ie,w}/\epsilon_{ie,L} = 1$. We will use a more detailed model of the

ratio $\epsilon_{ie,w}/\epsilon_{ie,L}$ in the next section.

The effect of transitioning from low confinement to high confinement is demon-

strated in Fig. 2.4. Here, we say that the transition occurs when $\Psi^* \Lambda_{\mathrm{lc}}^*(\Psi^*) = 0.1$,

which is an implicit relation for Ψ^* and can be solved numerically. The high con-

finement regime ($\Psi < \Psi^*$) is coincident with very small wall fluxes, $\mu_w \ll 1$, a near

perfect channel efficiency, $\eta_c \approx 1$, and a mass utilization efficiency that approaches

$\eta_m \approx \eta_{m,\mathrm{hc}}$. As Ψ increases above Ψ^*, an appreciable percentage of the ions formed

in the channel flow to the wall compared to the exit. As a result, the mass utilization

efficiency decreases because fast neutrals are lost from the device, and the channel

efficiency decreases because power deposition at the wall becomes significant.

The increased efficiency with applied magnetic field strength was observed in

the analytical model of Ahedo and Navarro-Cavallé [17] and Lafleur [72]. Ahedo
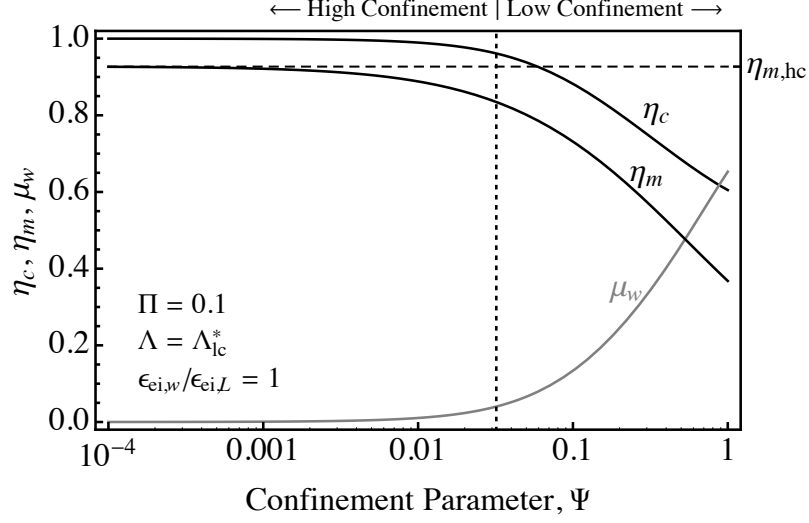
Figure 2.4: Variation of the channel efficiency, η_c, mass utilization efficiency, η_m, and ratio of the ion mass flow rate to the wall and channel exit, μ_f, with the confinement parameter, Ψ. The transition between low confinement and high confinement at $\Psi = \Psi^*$ is clearly demonstrated.

and Navarro-Cavallé considered a cylindrical model of a plasma discharge in which diffusion to the walls was dominated by classical collisions [88]. Lafleur, on the other hand, used a semi-empirical model for ion Bohm diffusion to the wall. As we showed in the example above, the critical magnetic field strength for efficient confinement can be described within our model by the dimensionless product $\Psi\Lambda = b/Pe_{\mathrm{an}}$. This is a general result, from which we can recover the dimensionless parameters governing wall losses in the models of Ahedo and Navarro-Cavallé and Lafleur by inserting the classical diffusion coefficient and ion Bohm diffusion coefficient into the anispotropic Peclet number, Pe_{an}, respectively.

2.2 Magnetic nozzle model

Possessing scaling relations for the performance of the channel, we now focus our efforts on modeling the magnetic nozzle region. The efficiency of the magnetic nozzle, defined as the ratio of the (axially) directed kinetic power of the exhaust to the power

into the MN, can be factorized as [85]

$$\eta_{\text{mn}} \equiv \frac{P_{k,z}}{P_L} = \eta_{\text{conv}}\eta_{\text{div}}. \tag{2.22}$$

Here, $\eta_{\text{conv}} \equiv P_k/P_L$ is the thermal conversion efficiency of the MN, defined as the ratio of the total kinetic power of the exhaust to the incoming power. The divergence efficiency, $\eta_{\text{div}} \equiv P_{k,z}/P_k$, represents the ratio of the directed to undirected kinetic power of the exhaust.

We develop simple scaling laws for η_{conv} in Sec. 2.2.1. Because the exhaust divergence is inherently a two-dimensional problem, we derive in Sec. 2.2.2 an approximate analytical solution for the 2D MN expansion model of Ahedo and Merino [23]. Using this solution, we obtain a basic scaling law for η_{div}.

2.2.1 Thermal conversion efficiency scaling

The MN converts electron thermal energy into ion kinetic energy. If we define the exhaust velocity, u_{ex}, as the asymptotic ion velocity for full expansion, the maximum kinetic power achievable within the MN ion beam may be written as

$$P_k \equiv \frac{1}{2}\dot{m}_{i,L}u_{\text{ex}}^2 = \frac{1}{2}\dot{m}_{i,L}g_u^2\left(\frac{\gamma_e T_e}{m_i}\right). \tag{2.23}$$

Here, $g_u = u_{\text{ex}}/\sqrt{\gamma_e T_e/m_i}$ is a measure of the ion velocity increase acquired in the MN and T_e is the electron temperature at the MN throat.

Using Eq. (2.16), we write the thermal conversion efficiency in the following form,

$$\eta_{\text{conv}} \equiv \frac{P_k}{P_L} = \frac{g_u^2\gamma_e T_e}{2\epsilon_{ei,L}}. \tag{2.24}$$

It is clear from this equation that a high conversion efficiency requires the average kinetic energy per downstream ion, $g_u^2\gamma_e T_e/2$, be a significant portion of the average

34

energy per electron-ion pair emerging from the channel, $\epsilon_{ei,L}$. In reality, g_u is limited by frozen-flow losses because the recombination rate of the plasma is much slower than the expansion rate.

We highlight the importance of the electron heat conduction term, Q_e, within the electron-ion loss term, $\epsilon_{ei,L}$. As noted by Ahedo and Navarro-Cavallé [17], electron heat conduction plays an important role in the overall power balance of a MN thruster because it can significantly change the amount of power in the exhaust. Fruchtman et al. [74] assume the plasma to be adiabatic ($Q_e = 0$) at the channel exit. Ahedo and Navarro-Cavallé [17] argue that adiabaticity requires a highly-collisional plasma, which is not the case for the HPTs considered in their model. Instead, they assume that the high electron mobility along the magnetic field promotes an isothermal electron population. A well-known consequence [76] of unbounded, isothermal expansion is that it requires an infinite amount of heat ($Q_e \to \infty$) to maintain a constant temperature. This crisis is avoided in their model by assuming the plasma is absorbed by a conducting metal wall at a distance L_n downstream from the MN throat. Similarly, Lafleur [72] avoids the same crisis by assuming the plasma detaches at a location where the ion Larmor radius equals the local plume radius [89, 90]. In contrast to the results of Ahedo and Merino [23], this detachment mechanism assumes the Lorentz force on the ions dominates the force due to the ambipolar electric field. Furthermore, it relies on knowledge of the ion temperature, which introduces a free parameter within Lafleur's model. For MN performance predictions, the reliance of these models on a free parameter to bound the effective expansion, and therefore the electron heat conduction, represents a severe limitation because the predicted performance can be relatively sensitive to the value of the free parameter.

We avoid the isothermal expansion singularity by assuming the electrons cool according to a polytropic process, $p_e/n_e^{\gamma_e} = C(\psi)$, where C is constant along a char-

acteristic surface ψ. The ion velocity increase acquired through the nozzle is [85]

$$g_u = \sqrt{\frac{\gamma_e + 1}{\gamma_e - 1}}, \tag{2.25}$$

where we have assumed that the plasma expands fully, but does not recover the energy contained within the excitation and ionization modes. Furthermore, the electron heat flux at the nozzle throat takes the form [70]

$$Q_e = \frac{3}{2} \frac{\dot{m}_{i,L} T_e}{m_i} \left(\frac{5/3 - \gamma_e}{\gamma_e - 1} \right). \tag{2.26}$$

We note the two well-known limits of adiabatic ($\gamma_e = 5/3$) and isothermal ($\gamma_e = 1$) expansion. For an adiabatic process, $Q_e = 0$ and $g_u = 2$. Again, for isothermal expansion both $g_u \to \infty$ and $Q_e \to \infty$.

It is fair to say that, in order to limit Q_e, we have also introduced a free parameter to our equations in the form of the electron polytropic index, γ_e. Contrary to the free parameters used by Ahedo and Navarro-Cavallé and Lafleur, the polytropic law (and thus γ_e) has been used extensively in the literature to simplify the energy equation when modeling a wide variety of plasmas [76, 91, 92, 93]. Given its importance to MN performance models, we will return to γ_e in Chapter 5.

Insertion of Eqs. (2.25) and (2.26) into Eq. (2.24) yields a simple scaling law for the thermal conversion efficiency of the MN,

$$\eta_{\mathrm{conv}} = \left(1 + \frac{2}{\gamma_e g_u^2} \frac{\epsilon_{\mathrm{ion}}'}{T_e} \right)^{-1}. \tag{2.27}$$

The dependance of η_{conv} on the ratio $\epsilon_{\mathrm{ion}}'/T_e$ is a known trait of low pressure, high temperature electric propulsion systems [12], whose recombination timescales far exceed the transit time of the plasma. In other words, energy deposited into ionization and excitation of the plasma represents a frozen-flow loss of the expansion process.

Eq. (2.27) indicates that thermal conversion losses can be minimized with respect to the input power if the kinetic energy per ion exceeds the effective ionization energy. A similar equation was derived previously by Manheimer and Fernsler [11] and Ahedo [94], although neither for the polytropic expansion. The main consequence is that the electron temperature within the thruster becomes an important parameter in the overall efficiency of the device.

2.2.2 Divergence efficiency scaling[3]

Quasi-1D (Q1D) models are limited by the fact that any variation of the plasma parameters in the direction perpendicular to the flow is averaged out. Therefore, it is impossible to predict the effect of non-uniformities in this direction. Some semi-empirical performance models have had success by assuming that the radial plasma density profile maintains the same shape, or is self-similar, throughout the exhaust [32, 96]. The self-similar assumption, however, is not capable of describing the radial focusing of the plasma density profile with respect to the magnetic field divergence: a behavior that has been observed in several experiments [22, 97, 98, 99] and numerical models [23, 97].

Ahedo and Merino investigated the 2D nature of ED-MNs by solving a reduced, collisionless two-fluid plasma model [23]. They showed that the relative focusing of the density profile occurs along with the growth of an electric field perpendicular to the direction of the applied magnetic field. They also observed separation between the ion and electron (magnetic) streamlines. A later extension of their model to the far downstream region revealed that ion separation from the magnetic field lines results in the bulk flow of momentum towards the downstream direction, thus minimizing the

---

[3]This section is adapted from the theoretical model presented in [95]: J. M. Little and E. Y. Choueiri, "Thrust and efficiency model for electron-driven magnetic nozzles," *Phys. Plasmas*, Vol. 20, no. 103501, 2013.

problem of plasma detachment, and allowing for the determination of the divergence efficiency, η_{div} [9].

Theoretical models have provided valuable insight into the 2D nature of ED-MN exhaust plumes, but a simple performance model that captures this nature is lacking. Because of its ability to self-consistently reproduce 2D effects, we seek an approximate, closed-form solution to the model of Ahedo and Merino [23]. We will apply this solution to the ED-MN exhaust plume and compare the analytical solution to the exact numerical results of Ahedo and Merino. The transparency of our closed-form analytical solution will allow us to analyze in greater depth than possible with numerical solutions the dependence of the 2D nature of the plasma exhaust on the properties of the plasma flow into the MN. This analysis ultimately yields analytical scaling laws for η_{div} in terms of the properties of the plasma flow into the MN and magnetic field geometry.

2-Fluid Model Separable Solution

In this section we derive an approximate analytical solution to the two-fluid model proposed by Ahedo and Merino[23]. Our solution method is motivated by their exact numerical solution, which indicates that the average of the plasma potentials along the nozzle axis and the exhaust boundary approximates the potential predicted from the Q1D model. Assuming that the ion trajectory *approximately* follows the magnetic field lines, it is possible to find the potential gradient in the direction perpendicular to the magnetic field. This result, combined with the Q1D solution for the potential averaged over the plasma cross-section, yields an analytical expression for the 2D potential distribution in the plasma. Conservation equations provide the plasma density and ion Mach number.

We restrict our model to a collisionless, isothermal plasma flow. The validity of the collisionless assumption depends strongly on the properties of the source plasma,

but is typically met in low-pressure, high-temperature ED-MN plasmas [19]. The isothermal electron assumption is common in the literature due to the high electron thermal conductivity along the magnetic field [11]. Ultimately, we will see both theoretically and experimentally that a polytropic law is more appropriate to describe electron cooling in a MN exhaust. An extension of the model presented here to a polytropic flow is contained in Appendix B. The insight obtained from the isothermal model, however, applies to both cases.

We neglect electron inertial effects and induced magnetic fields. Electron inertial effects become important when $r_{L,e}/L_{\nabla B} \sim 1$, where $r_{L,e}$ is the electron Larmor radius and $L_{\nabla B} = |B/\nabla B|$ is the magnetic field scale length. The magnitude of the induced magnetic field becomes the same order as the applied magnetic field as $\beta \sim 1$. Here, β is the ratio of the thermal energy density of the plasma to the magnetic field energy density. These requirements ($r_{L,e}/L_{\nabla B} \ll 1$ and $\beta \ll 1$) are also met in a typical ED-MN plasma source [19]. Far downstream, however, both $r_{L,e}/L_{\nabla B}$ and β may approach unity, at which point these processes have been hypothesized to play a pivotal role in plasma detachment [5, 6, 7, 69].

In light of the above assumptions, the problem is described by the momentum and continuity equations for the ions and electrons [23]. These eight equations may be re-cast in the following dimensionless form:

$$\nabla \left(\frac{1}{2} u_i^2 + \phi \right) = \mathbf{u}_i \times \left(\frac{\mathbf{B}}{\rho_i} + \nabla \times \mathbf{u}_i \right), \tag{2.28}$$

$$\nabla \left(\ln n - \phi \right) = \mathbf{u}_e \times \frac{\mathbf{B}}{\rho_e}, \tag{2.29}$$

$$\nabla \cdot (n\mathbf{u}_i) = 0, \tag{2.30}$$

$$\nabla \cdot (n\mathbf{u}_e) = 0. \tag{2.31}$$

Here, we have normalized the ion and electron velocities by the ion acoustic speed, $c_s = (k_b T_e/m_i)^{1/2}$. The electric potential, Φ, is normalized by the electron temperature, T_e, such that $\phi = e\Phi/kT_e$. Furthermore, $\rho_j = (m_j c_s/eB^*)/L^*$, is the normalized Larmor radius of species j, with B^* and L^* the characteristic magnetic field strength and length scale of the plasma, respectively. We note ρ_i represents an *effective* Larmor radius for the ions, and can be viewed as a measure of ion magnetization [23].

Using an approximation for the ion trajectory, we will now reduce Eqs. (2.28)-(2.31) to a system of three equations for three unknowns: the ion Mach number, $M = |\mathbf{u}_i|$; the plasma density, n; and the plasma potential, ϕ. First, we consider the component of Eq. (2.29) along the magnetic field unit vector, $\mathbf{b}$,

$$\mathbf{b} \cdot \nabla (\phi - \ln n) = 0. \tag{2.32}$$

This is the well-known Boltzmann distribution along a magnetic field line [100].

Ahedo and Merino [23] show that the terms on the right hand side of Eq. (2.28) have little influence on the ion dynamics for flows that satisfy $\rho_i > 1$ (i.e. unmagnetized ions). The triviality of this term, which includes the centrifugal and magnetic forces, implies that the ion motion is dominated by electrostatic forces. Furthermore, they find $M \gg |\mathbf{u}_i \cdot \mathbf{e}_\theta|$, which implies the ion velocity unit vector, $\mathbf{s}$, is contained primarily in the $r - z$ plane: $\mathbf{s} \cdot \mathbf{e}_\theta \approx 0$.

Projecting Eq. (2.28) onto the ion velocity unit vector relates the ion Mach number and potential,

$$\mathbf{s} \cdot \nabla (M^2 + 2\phi) = 0, \tag{2.33}$$

which represents the conservation of ion energy along an ion streamline.

The final equation comes from rewriting Eq. (2.30) in integral form. Applying the divergence theorem yields,

$$\int_S nM (\mathbf{s} \cdot \mathbf{dA}) = 0, \tag{2.34}$$

where S denotes a control surface that intersects the plasma flow.

Eqs. (2.32)-(2.34) represent an underdetermined system of three equations for four unknowns: M, n, ϕ, $\mathbf{s}$. The only physical phenomena eliminated from the governing equations, Eqs. (2.28)-(2.31), are the magnetic and centrifugal forces on the ions. Closure of the problem does not require the equation for electron force balance in the perpendicular direction as it would introduce the electron azimuthal velocity, $u_{\theta,e}$, as a fifth unknown. In fact, assuming knowledge of the plasma parameters along a cross-sectional flow plane, Ahedo and Merino show that, for isothermal expansion, $u_{\theta,e}$ can be determined everywhere analytically using only the magnetic field topology [69]. We note that we have not neglected the effect of the hot electrons because we included their influence over the ions through the ambipolar electric field in Eqs. (2.32) and (2.33). By ignoring the cross-field electron force balance, we are assuming that the electrons, by virtue of their strong magnetization, ensure the plasma is confined within a bounding magnetic flux surface.

Numerical results [23] indicate that, even for plasmas where the ion streamlines deviate significantly from their initial magnetic flux surface, the local angle between the magnetic field and ion velocity unit vectors remains less than five degrees even far downstream into the plume. Thus, we close the system of equations by assuming that ion velocity unit vector is *approximately* parallel to the magnetic field unit vector, $\mathbf{s} \approx \mathbf{b}$. We refer to this assumption as *quasi*-field-aligned flow.

While the quasi-field-aligned approximation seems prohibitive, especially in the presence of significant cross-field ion motion, we will show that it allows analytical solutions that exhibit remarkable agreement with numerical solutions. Eventually, however, this approximation becomes invalid in the far-field region beyond the turning point of the magnetic field [9].

With the aim of further simplifying Eqs. (2.32)-(2.34), we employ a transformation from cylindrical to magnetic coordinates. The magnetic field vector, $\mathbf{B}$, may be
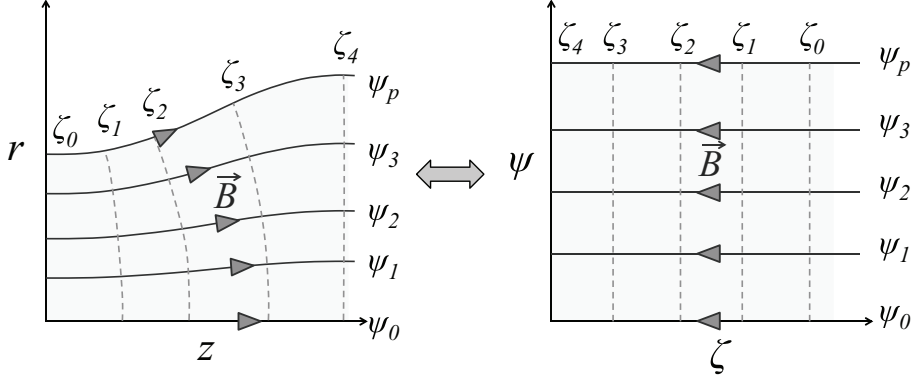
Figure 2.5: Transformation from cylindrical (r,z) to magnetic (ψ,ζ) coordinates. $\vec{B}$ represents the magnetic field vector aligned along surfaces of constant ψ.

described in terms of two scalar functions as

$$\mathbf{B} = -\frac{1}{r}\left(\mathbf{e}_\theta \times \nabla\psi\right) = -\nabla\zeta, \tag{2.35}$$

where ψ is constant along any magnetic flux surface, ζ is constant along any surface that is everywhere normal to the magnetic field vector, and $\mathbf{e}_\theta$ is the unit vector in the azimuthal direction. We refer to surfaces of constant ψ and ζ as ψ-surfaces and ζ-surfaces, respectively. Figure 2.5 illustrates the conversion from cylindrical coordinates to magnetic coordinates for a flow confined within the flux surface ψ_p.

The coordinate transformation allows the simplification, $\mathbf{b}\cdot\mathbf{dA} = dA$, where dA is the differential area of a ζ-surface. The integral of a function $X(\psi,\zeta)$ over a ζ-surface from $\psi \in [0,\psi_p]$ simplifies to

$$\int_\zeta X(\psi,\zeta)dA = 2\pi \int_0^{\psi_p} \frac{X(\psi,\zeta)}{B(\psi,\zeta)}d\psi. \tag{2.36}$$

Furthermore, the ψ-average of this function is given by

$$\bar{X}(\zeta) = [A(\zeta)]^{-1}\int_\zeta X(\psi,\zeta)dA, \tag{2.37}$$

42

where $A(\zeta)$ is the total area of the ζ-surface.

We assume that there exists a throat plane defined by $\zeta = \zeta_t$, along which $M(\psi, \zeta_t) = 1$ and $\phi(\psi, \zeta_t) = 0$. The plasma density profile along this plane is defined by the function $n(\psi, \zeta_t) = n_t(\psi)$.

Using the quasi-field-aligned assumption, the conditions at the throat plane may be substituted into Eqs. (2.32) and (2.33) to yield algebraic expressions for the density and ion Mach number in terms of the electric potential [23],

$$n = n_t e^{\phi}, \tag{2.38}$$

$$M = \sqrt{1 - 2\phi}. \tag{2.39}$$

Thus, our main task is to derive ϕ, from which n and M may be found from Eqs. (2.38) and (2.39).

The coordinate transformation enables the separate treatment of the electric potential averaged over the beam cross-section and its variation across the beam cross-section,

$$\phi(\psi, \zeta) = \bar{\phi}(\zeta) + \varphi(\psi, \zeta), \tag{2.40}$$

with the additional requirement

$$\int_{\zeta} \varphi(\psi, \zeta) \, dA = 0. \tag{2.41}$$

Hence, along each ζ-surface, the potential is separated into a ψ-averaged component, $\bar{\phi}$, and a two-dimensional, ψ-dependent correction, φ, whose average over the entire beam cross-section along the ζ-surface is zero.

The ζ-dependance of the ψ-averaged potential is obtained from the well known Q1D model [1],

$$e^{\bar{\phi}} \sqrt{1 - 2\bar{\phi}} = \frac{A_t}{A}. \tag{2.42}$$

43

Here, $A_t = A(\zeta_t)$ may be found from Eq. (2.36). We note that Eq. (2.42) is an implicit equation and does not have a closed-form solution.

The ψ-dependent correction, φ, may be found from the force balance on ions in the direction perpendicular to the magnetic field,

$$rB\frac{d\varphi}{d\psi} = -\frac{M^2}{R_c}.$$

(2.43)

We have introduced here the local radius of curvature of the ion streamline, $R_c = |\mathbf{n}\cdot(\mathbf{s}\cdot\nabla\mathbf{s})|^{-1}$, where $\mathbf{n}$ is the unit vector along a ζ-surface.

Invoking the quasi-field-aligned approximation, we express the radius of curvature in terms of the unit vectors perpendicular and parallel to the applied magnetic field, $\mathbf{h}$ and $\mathbf{b}$, respectively: $R_c \approx |\mathbf{h}\cdot(\mathbf{b}\cdot\nabla\mathbf{b})|^{-1}$. This allows R_c to be determined from the local radius of curvature of the applied magnetic field.

Substitution of Eqs. (2.39) and (2.40) into Eq. (2.43) allows the description of φ in terms of the nonlinear ODE,

$$\frac{d\varphi}{d\psi} + \frac{1 - 2\bar{\phi} - 2\varphi}{rBR_c} = 0,$$

(2.44)

from which separation of variables and Eq. (2.40) yield

$$\phi(\psi,\zeta) = \frac{1}{2} + C(\zeta)\exp\left[\int_0^\psi K(\psi',\zeta)\,d\psi'\right].$$

(2.45)

Here, $K = (rBR_c)^{-1}$, and represents the effective local curvature of the magnetic field in the magnetic coordinate system. The integration constant, C, may be found from Eq. (2.41).

We take a moment to discuss an inconsistency that arises from solving Eq. (2.43) with the quasi-field-aligned approximation. Specifically, the formation of a perpendicular electric field implies a changing cross-sectional density profile through Eq. (2.38).

44

However, the changing density profile requires that the ion streamlines deviate from the magnetic field lines to preserve quasineutrality. The implication is that perpendicular electric fields are incapable of constraining ions to *exactly* follow curved magnetic field lines.

Therefore, the quasi-field-aligned approximation is inconsistent with Eq. (2.43) because the local ion curvature radius cannot equal the magnetic field curvature radius. By setting the two curvature radii to be equal, Eq. (2.43) overestimates the electric field, and thus also the potential gradient in the cross-field direction. We will show, however, that the error due to this inconsistency is relatively small for plasma flows through slowly diverging magnetic fields. This is because the cross-field velocity of the ions remains small compared to the field-aligned velocity, which implies that the length scale of separation between the ion streamlines and magnetic field lines is much smaller than the length scale over which that separation occurs. Ultimately, this allows our approximate analytical solution to capture the effect of ion cross-field motion on the plasma density profile without self-consistently solving the ion equations of motion.

Using the expansion region of an ED-MN plasma as an example, we will show that the analytical equations derived here predict ϕ, M, and $\ln(n)$ to within a few percent of the values obtained from the exact numerical solution to the fluid equations. However, the error in ϕ increases in the far downstream region due to ion cross-field motion. Because errors in n scale exponentially with errors in ϕ, the separable solution violates mass conservation in this region. Therefore, it is necessary to implement a mass conservation correction into the solution.

The excess mass flow rate through each ζ-surface is given by

$$\epsilon_{\dot{m}} = \frac{1}{\bar{n}_t A_t} \int_\zeta n M dA, \tag{2.46}$$

where zero error occurs for $\epsilon_{\dot{m}} = 1$. We multiply each plasma parameter by a correction factor, α, that is a function of only ζ, such that,

$$\phi \to \alpha_\phi \phi \qquad n \to \alpha_n n \qquad M \to \alpha_M M \tag{2.47}$$

Using Eq. (2.46), mass conservation is guaranteed for any α-combination that satisfies

$$\epsilon_{\dot{m}} = (\alpha_M \alpha_n)^{-1}. \tag{2.48}$$

The mass-conserving solutions must also satisfy the quasi-one-dimensional equations. From these, we derive the final two equations needed to solve for each α:

$$\left(1 - 2\bar{\phi}\right) \exp\left[2\left(1 - \alpha_\phi\right)\bar{\phi}\right] - \epsilon_{\dot{m}}^2 \left(1 - 2\alpha_\phi\bar{\phi}\right) = 0, \tag{2.49}$$

$$\alpha_n = \exp\left[\left(\alpha_\phi - 1\right)\bar{\phi}\right], \tag{2.50}$$

Here, $\bar{\phi}$ is the ψ-averaged potential *prior* to applying the mass correction. Eq. (2.49) represents an implicit equation for α_ϕ in terms of $\bar{\phi}$ and $\epsilon_{\dot{m}}$. The mass-conserving potential may then be found by multiplying the right hand side of Eq. (2.45) by α_ϕ.

Structure of the Magnetic Nozzle Exhaust Plasma

We will now demonstrate how our 2D separable solution can be applied to the MN exhaust plume. Most experiments and physical models of MNs use a simple magnetic configuration for which acceleration occurs in the fringe fields of the plasma source magnets. We will not restrict ourself to this configuration, but rather allow for an acceleration region prior to the exhaust plane as depicted in Fig. 1.1. Ultimately, this is equivalent to starting the model of Ahedo and Merino [23] with a Mach number greater than one [7].

We begin by defining the coordinate transformation from cylindrical to magnetic coordinates (Figure 2.6). The magnetic field in the exhaust region may be approximated by the magnetic field of a single loop of current, from which the ψ-surfaces and ζ-surfaces may be further approximated as

$$\psi\left(r, z\right) = \frac{r^2/2}{\left(1 + r^2 + z^2\right)^{3/2}},\tag{2.51}$$

$$\zeta\left(r, z\right) = \frac{z/2}{\left(r^2 + z^2\right)^{3/2}}.\tag{2.52}$$

All lengths above and throughout the remainder of this section are normalized by the effective radius of the exhaust magnet, r_c. Eq. (2.52) is a valid approximation to Eqs. (2.35) and (2.51) for values of $z > 1$. From this point forward, our results will be limited to MN exhausts whose magnetic field may be approximated by that of a dipole, or Eqs (2.51) and (2.52).

The acceleration region, used to increase the Mach number of the flow prior to entering exhaust region, relates the throat and exhaust plane plasma parameters. For the magnetic field model above, the throat is not necessarily located at $z = 0$, but rather at some unspecified location upstream from the exhaust plane. Along the throat plane the potential and ion Mach number are given by $M\left(\psi, \zeta_t\right) = 1$ and $\phi\left(\psi, \zeta_t\right) = 0$, respectively.

An analytical expression for the radial density distribution of plasma confined within a cylindrical vessel was derived by Ahedo [88], and later used by Ahedo and Merino [23] to characterize the 2D expansion of a non-uniform magnetic nozzle plasma. To allow direct comparison with their numerical results, we adopt their expression and transform it to magnetic coordinates as

$$n\left(\psi, \zeta_t\right) = J_0\left[a_0\sigma\left(\frac{2\psi^{1/2} + 3\psi^{3/2}}{2\psi_p^{1/2} + 3\psi_p^{3/2}}\right)\right].\tag{2.53}$$
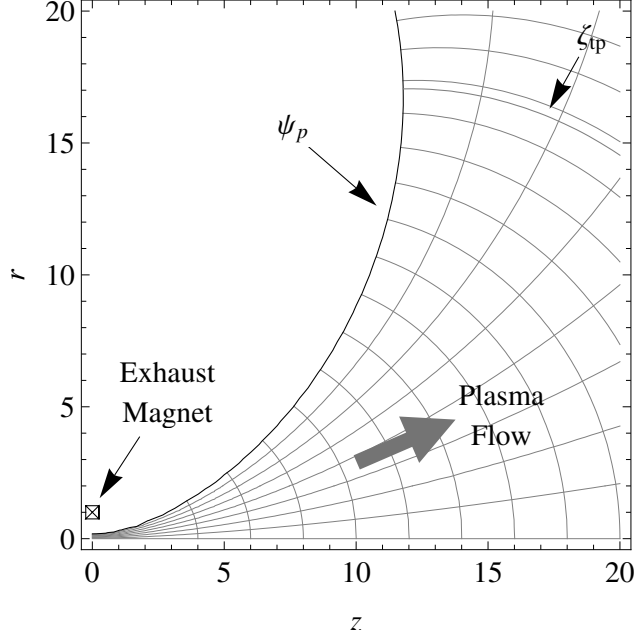
Figure 2.6: Transformation from cylindrical (r, z) to magnetic (ψ, ζ) coordinates using Eqs. (2.51) and (2.52). Distances are normalized by the effective radius of the exhaust magnet, r_c. In this example, the bounding flux surface is given by $\psi_p = \psi(0.185, 0)$. The ζ-surface corresponding to the turning point (tp) of ψ_p is labelled ζ_{tp}.

In this equation, J_0 is the zeroth Bessel function, a_0 is the first zero of J_0, and σ is a parameter less than unity that controls the uniformity of the density profile at the throat. For example, $\sigma = 0$ represents a radially uniform plasma. The uniformity decreases for $\sigma > 0$.

The plasma at the nozzle exhaust plane is related to the throat plane by two geometric ratios: the expansion ratio, R_E, and exhaust aperture ratio, $R_{A,e}$. The expansion ratio, defined above, determines the Mach number at the exhaust plane, M_e, through Eq. (2.39),

$$R_E = \frac{1}{M_e} \exp\left(\frac{M_e^2 - 1}{2}\right). \tag{2.54}$$

The exhaust aperture ratio, $R_{A,e} = (r_e/r_c)^2$, determines the bounding magnetic field flux surface, $\psi_p = \psi(r_e, 0)$, and thus the divergence of the plasma boundary in the exhaust region. It is reassuring that we recover, with the exception of the ion magne-

tization parameter, the same independent variables used by Ahedo and Merino [7, 23], namely M_e, r_e, and σ.

Armed with a magnetic field model and exhaust plane conditions, our task is now to solve Eq. (2.45) for ϕ. Substitution of Eq. (2.51) into Eq. (2.35) yields an expression for **B**. This expression may then be inserted into Eq. (2.36) with X=1 to find the cross-sectional area, A. The area of the plasma at ζ_t is given by $A_t = A_e/R_E = \pi r_e^2/R_E$. Finally, insertion of the ratio A_t/A into Eq. (2.42) yields $\bar{\phi}$.

An analytical solution to Eq. (2.45) is still out of reach due to the complexity of the function $K(\psi, \zeta)$. It is possible to show that K is much more sensitive to variations in ζ than ψ. In fact, K varies by less than a factor of 2 along a ζ-surface. Thus, we approximate this function as constant with respect to ψ, from which we take the taylor series of K and consider the limit as $\psi \to 0$. This procedure yields,

$$K\left(\psi, \zeta\right) \approx k\left(\zeta\right) = \frac{3\sqrt{2}}{8}\left[\frac{1+4\zeta}{\sqrt{\zeta\left(1+2\zeta\right)}}\right] \approx \frac{3}{4\sqrt{2\zeta}}, \tag{2.55}$$

where the approximation on the far-right-hand side is valid for $\zeta < 1$ (or, $z > 1$). Eqs. (2.41) and (2.45) thus give

$$\phi = \frac{1}{2}\left[1 - \left(1 - 2\bar{\phi}\right)\frac{2k\psi_p}{e^{2k\psi_p} - 1}e^{2k\psi}\right]. \tag{2.56}$$

We note that $\bar{M}^2 = 1 - 2\bar{\phi}$. Eq. (2.56) then suggests that the extent to which non-uniformities manifest within the exhaust depends on the local, ψ-averaged ion Mach number. Indeed, we will show that the relative focusing of the exhaust beam, and consequently the detachment of ions and beam divergence efficiency of the nozzle, both scale with $\bar{M}$.
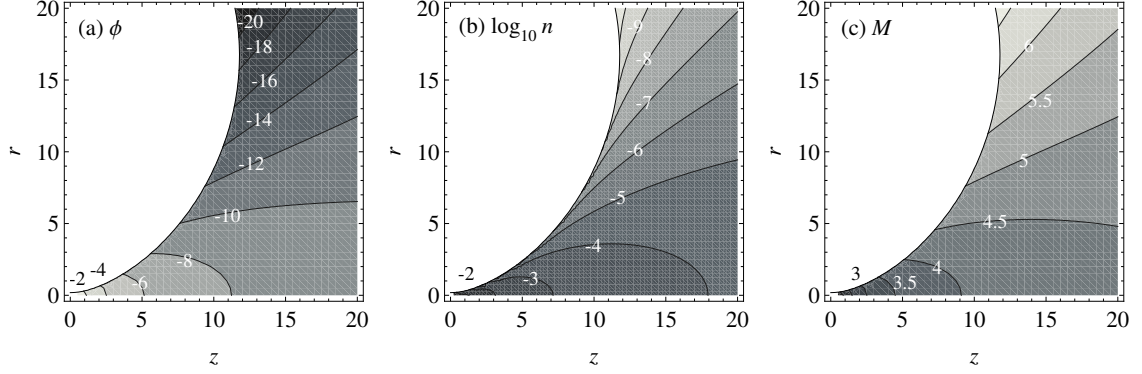
Figure 2.7: Contour plots of the approximate analytical solution for the potential, ϕ, density, n, and ion Mach number, M, for the plasma exhaust plume of an ED-MN. The exhaust and throat planes coincide ($M_e = M_t = 1$), and the plasma radius at the exhaust plane is $r_e = 0.185$.

The location at which 2D effects become important may be determined from the parameter,

$$\epsilon_u \equiv \left| \frac{\phi\left(\psi_p, \zeta\right) - \phi\left(0, \zeta\right)}{\bar{\phi}\left(\zeta\right) - \phi_e} \right| \approx 2k\psi_p \left[1 + \left(\frac{M_e}{\bar{M}}\right)^2\right]. \qquad (2.57)$$

The approximation on the right-hand side is valid in the immediate expansion region ($k\psi_p << 1$). Setting $\epsilon_u = 0.05$ in the limit $M_e/\bar{M} << 1$ yields $z^* \approx (2/30)r_e^{-2}$, where z^* is the axial location along the nozzle axis at which point 2D effects become predominant, which also corresponds to the breakdown of the self-similar assumption and the point at which ion detachment from the applied magnetic field begins. Clearly, z^* should increase for highly magnetized plasma, which is not captured here.

Closed-formed solutions for n and M are obtained by substituting Eqs. (2.53) and (2.56) into Eqs. (2.38) and (2.39). These expressions are not shown here for the sake of brevity. Finally, it may be necessary (*e.g.* to calculate C_T) to implement the mass-conservation correction outlined in Eq. (2.49). Numerical integration of Eq. (2.46) yields $\epsilon_{\dot{m}}$. Eqs. (2.48)-(2.50) can then be used to find α_ϕ, α_n, and α_M.

Contour plots of ϕ, n, and M are presented in Fig. 2.7 for $M_t = M_e = 1$ and $r_t = r_e = 0.185$. A number of observations may be made about the nature of this

50
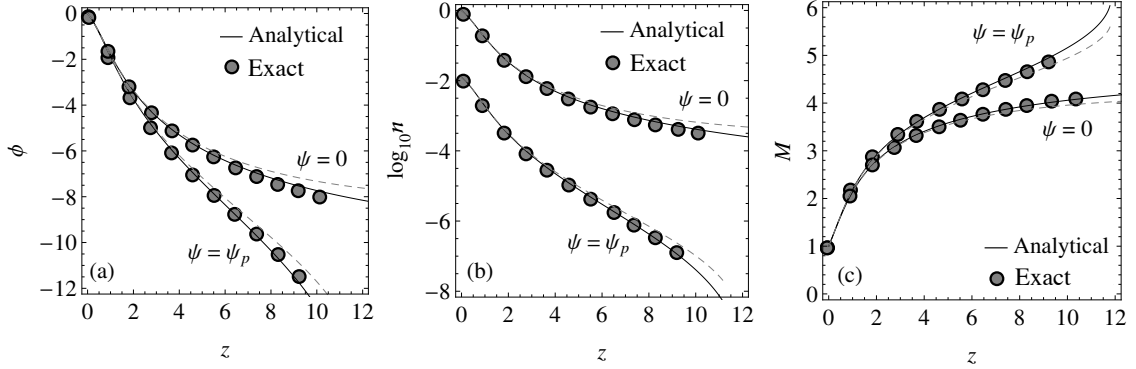
Figure 2.8: Comparison of the approximate analytical solution with (solid) and without (dashed) the mass conservation correction for the potential, ϕ, density, n, and ion Mach number, M to the numerical results (shaded points) from Fig. 4 of Ref. [23]. Note that the x-axis of the numerical data was adjusted to be consistent with our normalization.

flow that are in qualitative agreement with the analysis of Ahedo and Merino [23]: (1) A large potential well develops along the plasma edge in the far field of the plume; (2) the increased potential gradient near the edge of the plume leads to a rarefaction of the plasma edge; and (3) ions accelerate at a slower rate towards the nozzle axis compared to the plasma edge in the far field region.

We show in Fig. 2.8 a quantitative comparison of our 2D separable solution to the numerical results of Ahedo and Merino. Specifically, we take sample points from the low magnetization ($\Omega_i = 0.1$) curve of Fig. 4 from Ref. [23] to compare the analytical and numerical solutions for the axial dependence of ϕ, n, and M along the nozzle axis, $\psi = 0$, and plasma edge, $\psi = \psi_p$. The dashed lines correspond to the solution without the mass conservation correction, while the solid lines include the correction.

A strikingly good agreement is found between our approximate, analytical solution and the exact numerical solution to the full two-fluid equations. Specifically, the analytical solution, both with and without the mass conservation correction, accurately tracks the non-uniformities in the potential and ion Mach number that develop in the downstream region. Furthermore, the increased rarefaction of the plasma along

51

the boundary as predicted by the analytical solution matches that of the numerical solution.

Finally, we note that $z^* = 1.95$ for this example, which coincides well with the location at which the two curves bifurcate in Fig. 2.8.

Plume Divergence Scaling

The main question presented at the beginning of this section may now be recast in terms of the specific parameters relevant to the 2D separable solution. Specifically, *how does the beam divergence efficiency, η_{div}, of an ED-MN depend on the normalized plasma radius, r_e, ion Mach number, M_e, and density profile uniformity, σ, at the nozzle exhaust plane?*

It is necessary to first define the domain of our MN performance model. It is reasonable to suspect that the loss of magnetic confinement through plasma detachment defines the downstream boundary to the domain. This is because the reaction force of the plasma on the MN results from the diamagnetic current, and this current is a by-product of confinement of the thermal plasma by the magnetic field. With that said, the process by which the plasma detaches from the MN is not fully understood and is a topic of active research [4, 5, 6, 7, 8].

Fortunately, recent simulations of the far-field region of an ED-MN by Merino and Ahedo [9] show that a large portion ($> 99\%$) of the ion flow effectively separates from the applied magnetic field. In their model, the electrons are still confined by the magnetic field and continue to transfer momentum throughout the plume. Ion detachment implies that the bulk of the plasma, and thus the region that transfers the most momentum, continues to flow downstream as opposed to returning along the diverging magnetic field.

We conjecture, based on the results of Merino and Ahedo, that it is not necessary to include electron detachment within an ED-MN performance model as long as the

solution captures the effects of ion detachment (specifically, the relative focusing of the plasma with respect to the applied field). Furthermore, the axial separation between the magnets and the far-field plasma implies that very little momentum is exchanged beyond the the turning point of the applied magnetic field.

With this in mind, we define the domain for our performance model to be the volume of plasma up until the ζ-surface corresponding to the turning point of the nozzle, ζ_{tp} (see Fig. 2.6). Effectively, we are assuming electron detachment occurs downstream of ζ_{tp}. The performance parameters may then be obtained by considering the relevant momentum and power fluxes through the surface defined by ζ_{tp}. We were not able to find an analytical description of ζ_{tp} as a function of ψ_p. However, ζ_{tp} may be found numerically by solving $B_z\left(\psi_p, \zeta_{\mathrm{tp}}\right) = 0$. Fitting a curve to the various solutions, we obtain the approximate relation, $\zeta_{\mathrm{tp}} \approx 2.5\psi_p^2$, which is accurate to within 8% for $\psi_p \in [0, 0.07]$.

For a given ψ_p, the plasma beam divergence will depend on the relative focusing of the plasma density profile in the plume with respect to the divergence of the applied magnetic field. As an index of this focusing, we derive here a scaling relation for the half-width at half-maximum of the plasma density profile at ζ_{tp}.

The normalized density profile at ζ_{tp} is given by,

$$\chi_{\mathrm{tp}}(\hat{\psi}) = \frac{n(\hat{\psi}, \zeta_{\mathrm{tp}})}{n(0, \zeta_{\mathrm{tp}})}, \tag{2.58}$$

where $\hat{\psi} \equiv \psi/\psi_p$. The normalized half-width at half-maximum of the density profile at the nozzle turning point in the magnetic coordinate system, $\hat{\psi}_{1/2}$, may then be found from $\chi_{\mathrm{tp}}(\hat{\psi}_{1/2}) = 1/2$.

We find n using Eqs. (2.38) and (2.56), and approximate the plasma density profile at the throat, Eq. (2.53), as $n_t(\hat{\psi}) \approx 1 - [1 - J_0(a_0\sigma)]\hat{\psi}$. We substitute n into Eq. (2.58), expand $\chi_{\mathrm{tp}}(\hat{\psi})$ in a Taylor series up to second order in $\hat{\psi}$, and solve for

$\chi_{\text{tp}}(\hat{\psi}_{1/2}) = 1/2$. From this procedure we find,

$$\hat{\psi}_{1/2} \approx \frac{1}{2}\left[f_b\left(\bar{M}_{\text{tp}}, \sigma\right) - \sqrt{f_b\left(\bar{M}_{\text{tp}}, \sigma\right)^2 - 4f_c\left(\bar{M}_{\text{tp}}, \sigma\right)}\right], \tag{2.59}$$

where the functions f_b and f_c are given by

$$f_b\left(\bar{M}_{\text{tp}}, \sigma\right) = \frac{1}{c_1 \bar{M}_{\text{tp}}^2} + \frac{1}{1 - J_0\left(a_0 \sigma\right)}, \tag{2.60}$$

$$f_c\left(\bar{M}_{\text{tp}}, \sigma\right) = \frac{1 - h_f/2}{\left[1 - J_0\left(a_0 \sigma\right)\right] c_1 \bar{M}_{\text{tp}}^2}, \tag{2.61}$$

with constants,

$$c_1 = \frac{c_2^2}{2\left(e^{c_2} - 1\right)}, \qquad c_2 = \frac{3}{4\sqrt{5}}. \tag{2.62}$$

Here, $\bar{M}_{\text{tp}} = \bar{M}\left(\zeta_{tp}\right)$ is the ψ-averaged Mach number at the nozzle turning point. The additional constant, h_f, accounts for higher order terms.

Eq. (2.59) implies that $\hat{\psi}_{1/2}$ is dependent upon only two parameters: $\bar{M}_{\text{tp}}$ and σ. Using the quasi-1D equations, $\bar{M}_{\text{tp}}$ may be well-approximated as

$$\bar{M}_{\text{tp}} \approx \sqrt{M_e^2 - 2\ln\left(5^{1/2} M_e \psi_p^3\right)}. \tag{2.63}$$

To verify the scaling of Eq. (2.59), we plot in Fig. 2.9 the numerical solution to Eq. (2.58) for $\hat{\psi}_{1/2}$ versus $\bar{M}_{\text{tp}}$ for the following parameter space: $M_e \in [1, 4]$, $r_e \in [0.02, 0.45]$, and $\sigma \in [0.25, 1.0]$. We note that this parameter space will be used extensively throughout this section. Also shown in Fig. 2.9 are four curves that correspond to Eq. (2.59) with $\sigma = 0.25$, 0.5, 0.75, and 1.0. Here, $h_f = 1.22$ is chosen to produce the best fit.

The density profile HWHM *at the exhaust plane* may be approximately found by solving $J_0(a_0 \sigma \hat{\psi}^{1/2}) = 0.5$, which yields $\hat{\psi} \approx 6.4$, 1.6, 0.7, and 0.4 for $\sigma = 0.25$, 0.5, 0.75, and 1.0, respectively. It is clear from Fig. 2.9 that the HWHM at ζ_{tp} is much

54
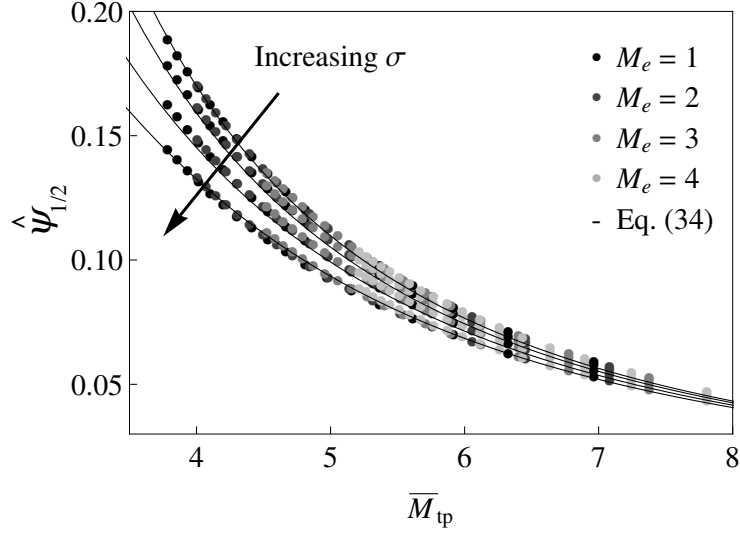
Figure 2.9: Half-width at half-maximum of the normalized density profile, $\hat{\psi}_{1/2}$, versus the ψ-averaged Mach number, $\bar{M}_{\text{tp}}$, at ζ_{tp}. Data points are found from the numerical solution of $\chi_{\text{tp}} = 1/2$. The analytical model (solid line) comes from Eq. (2.59).

less than its initial value, which indicates that the density profile has become focused with respect to the diverging magnetic field. Furthermore, this focusing increases with $\bar{M}_{\text{tp}}$.

We can use this result to derive scaling relations for η_{div}. Under the quasi-field-aligned assumption, the beam divergence efficiency may be written as,

$$\eta_{\text{div}} \equiv \frac{P_{k,z}}{P_k} = \int_{\zeta_{\text{tp}}} nM^3 \frac{B_z^2}{B^2} dA \bigg/ \int_{\zeta_{\text{tp}}} nM^3 dA \ . \tag{2.64}$$

Unfortunately, even though we now have analytical equations for the 2D distributions of each plasma parameter, the above integrals do not yield simple closed-form solutions. Therefore, η_{div} must be found through numerical integration of Eq. (2.64).

It is reasonable to assume, however, that the beam divergence efficiency may scale with the HWHM of the plasma density profile. As $\hat{\psi}_{1/2}$ decreases, we anticipate the beam divergence efficiency to increase because more plasma is concentrated along the nozzle axis. We take the effective plume half-angle, θ_{div}, to be the angle that

55

the magnetic field vector makes with the nozzle centerline at $\hat{\psi}_{1/2}$. This may be approximated as $\cos\theta_{\text{div}} \approx 1 - \hat{\psi}_{1/2}$. The beam divergence efficiency should then scale as $\eta_{\text{div}} \sim (1 - \hat{\psi}_{1/2})^2$. Indeed, Fig. 2.10 shows that this scaling is valid for small $\hat{\psi}_{1/2}$.
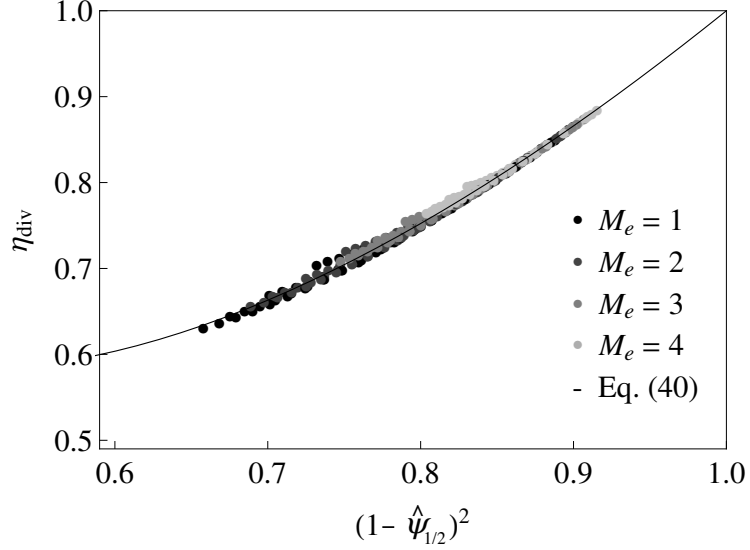
Figure 2.10: Beam divergence efficiency, η_{div}, versus the quantity $(1 - \hat{\psi}_{1/2})^2$. Data points are found from the numerical solution of Eq. (2.64). The analytical solution (solid line) comes from Eq. (2.65).

Adding a term to correct for larger values of $\hat{\psi}_{1/2}$, we propose the following model for η_{div}

$$\eta_{\text{div}} \approx c_{\eta 1} \left[(1 - \hat{\psi}_{1/2})^2 - 1 \right] + c_{\eta 2} \hat{\psi}_{1/2}^2 + 1. \tag{2.65}$$

Here, $c_{\eta 1} = 1.432$ and $c_{\eta 2} = 3.473$ result from the method of least-squares. Eq. (2.65), with $\hat{\psi}_{1/2}$ found from Eqs. (2.59) and (2.63), represents a fully analytical equation for the beam divergence efficiency of an ED-MN in terms of M_e, r_e, and σ.

Fig. 2.11 shows the beam divergence efficiency versus the normalized plasma radius for four different values of the ion Mach number at the exhaust plane and $\sigma = 1$. Similar agreement between the numerical solution to Eq. (2.64) and Eq. (2.65) may be seen for different values of σ. We can summarize from these plots the general
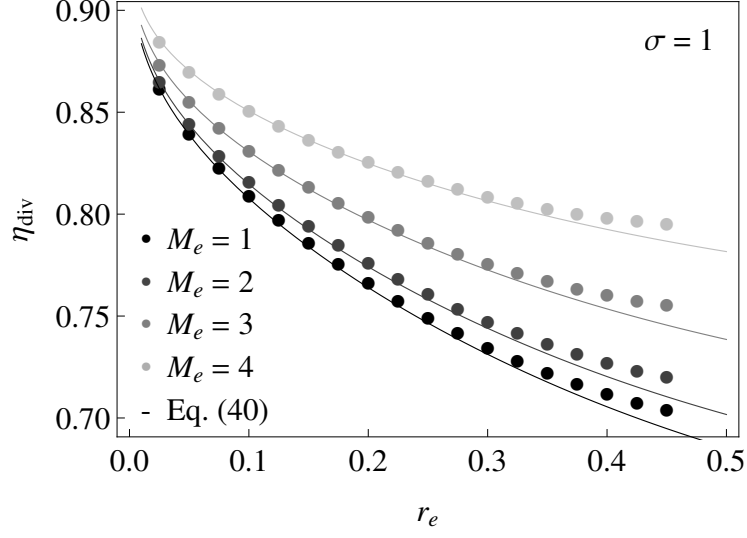
Figure 2.11: Beam divergence efficiency, η_{div}, versus the normalized exhaust radius, r_e, for $\sigma = 1$ and $M_e \in [1, 4]$. Data points are found from the numerical solution of Eq. (2.64). The analytical solution (solid lines) comes from Eq. (2.65).

dependence of the beam divergence efficiency on the nature of the exhaust plane plasma:

1. η_{div} decreases as r_e increases, and is very sensitive to changes in r_e.

2. The increased η_{div} that results from increasing M_e becomes more pronounced for $M_e > 1$ and $r_e > 0.1$.

3. Decreases in σ lead to decreases in η_{div} (not shown).

4. The sensitivity of η_{div} to changes in σ is much greater for small M_e (not shown).

Each of these dependencies is predicted by Eqs. (2.59), (2.63), and (2.65) over the chosen parameter space. We note the first and third dependencies were first observed in the exact numerical solutions of Ahedo and Merino [23].

Nozzle Design Implications

Most ED-MN thrusters that have been built in the laboratory utilize the fringe fields of the plasma source as a simple MN. The results of this section allow us the compare

the performance of the more general MN configuration depicted in Fig. 1.1 with the simple MN. Specifically, we want to answer the question: *how is the divergence efficiency of an ED-MN affected by the addition of an acceleration region outside of the channel?*

We showed previously that the ion Mach number and plasma radius at the exhaust section may be adjusted by altering the MN geometry. Specifically, M_e is determined by the expansion ratio from Eq. (2.54). Using the simple two magnet configuration depicted in Fig. 1.1, the normalized plasma radius at the exhaust, $r_e = R_{a,e}^{1/2}$, is related to the aperture ratio at the throat of the nozzle and the expansion ratio through

$$\frac{R_{A,e}}{R_{A,t}} \approx R_E \left(\frac{r_{c,t}}{r_{c,e}} \right)^2 \approx \frac{1}{R_E} \left(\frac{I_t}{I_e} \right)^2 . \tag{2.66}$$

Here, $I_t = r_{c,t} B_t$ and $I_e = r_{c,e} B_e$ represent the effective total current needed to produce the magnetic field B_t and B_e for the throat and exhaust magnets, respectively.

We may use Eq. (2.66) to examine the effect of adding an acceleration region to a given thruster. It is clear that R_A decreases with increasing R_E if the exhaust magnet carries the same current as the throat magnet, but at a larger radius. Alternatively, R_A increases with R_E if the exhaust magnet, while carrying less current, is the same size as the throat magnet.

Because η_{div} increases as R_A decreases, it is not beneficial to add an exhaust magnet that is the same size as the throat magnet. The addition of an exhaust magnet that is larger than the throat magnet, yet carrying comparable current, does lead to increased performance. However, it can be shown that this increase in performance is only significant for plasmas in which the throat aperture ratio is relatively large ($R_{A,t} \gtrsim 0.2$). This relates to our previous observation that improvements in η_{div} become more sensitive to increases in M_e as r_e increases.

In general, the addition of an acceleration region adds weight and complexity to the thruster. Eq. (2.66) implies that an exhaust magnet may only be beneficial for thrusters that exhibit poor confinement near the throat (large $R_{A,t}$). This may change, however, for highly magnetized plasmas ($\rho_i \ll 1$). The desire to reduce losses within the plasma source may lead to magnetic fields much larger than those reported in the literature for ED-MN thrusters. Plasma flow from an ED-MN in the high magnetization limit has been marked by a noticeable decrease in performance.[23, 9] Therefore, substantial efficiency improvements may be seen by using an exhaust magnet to step down the effective level of ion magnetization prior to exiting the thruster. A full analysis of this problem, however, is beyond the scope of this thesis.

2.3 Theoretical performance scaling

The scaling laws for the mass utilization efficiency and channel efficiency that we derived in Sec. 2.1 can be combined with the MN scaling laws from Sec. 2.2 to analyze the performance scaling and limitations of electric propulsion systems that use MNs. Recalling Eqs. (1.3)-(1.5),

$$\hat{I}_{\mathrm{sp}} = C_T = g_u \eta_m \eta_{\mathrm{div}}^{1/2}, \tag{2.67}$$

$$\eta_T = \eta_{\mathrm{ps}} \eta_m \eta_c \eta_{\mathrm{conv}} \eta_{\mathrm{div}}. \tag{2.68}$$

we see that, for a given plasma source, the performance of the MN can be analyzed using the dimensionless scaling parameters found in the previous sections.

In addition to the propellant properties, the dimensionless scaling parameters depend on the electron temperature, density, and magnetic field strength within the channel. Here, we will assume the channel is operating in the high confinement mode, $\eta_c = 1$, and is sufficiently long to allow full ionization, $\Lambda = \Lambda_{\mathrm{hc}}^*$. Under these assumptions, the specific impulse and thrust efficiency scale with only the electron

temperature for a specific propellant, polytropic index, and divergence efficiency. The plasma density can then be found from the desired thruster power, which determines the required channel length and magnetic field strength to meet the mass utilization and high confinement conditions.

2.3.1 Influence of the propellant gas

The propellant gas has a strong influence on performance because of the dependence on the ion mass, ionization and excitation energies, and ionization and CEX collision cross-sections. Here, we examine how these properties affect the neutral pumping parameter, channel length, and effective ionization energy.

The neutral pumping parameter can be written as the ratio of the CEX and ionization collision rate coefficients, $\Pi \equiv R_{\mathrm{cex}}/R_{\mathrm{ion}}$. Assuming a Maxwellian electron energy distribution, the CEX rate coefficient [101] and ionization rate coefficient [102] may be written in terms of the electron temperature as

$$R_{\mathrm{cex}} = 10^{-19} \left(a - b \log_{10} T_e \right) c_s \qquad [m^3/s], \qquad (2.69)$$

$$R_{\mathrm{ion}} = 6.7 \times 10^{-13} \frac{c}{T_e^{3/2}} \frac{1}{\epsilon_{\mathrm{ion}}/T_e} \int_{\epsilon_{\mathrm{ion}}/T_e}^{\infty} \frac{e^{-x}}{x} dx \qquad [m^3/s]. \qquad (2.70)$$

Here, electron temperature and ion acoustic velocity are expressed in units of eV and m/s, respectively. The coefficients a, b, and c are tabulated in Tab. 2.1 for common propellant gases.

Table 2.1: Table of CEX and ionization collision model parameters.

Gas	$a\,(m^2)$	$b\,(m^2)$	c	μ	$\epsilon_{\mathrm{ion}}\,(\mathrm{eV})$	$\epsilon_1\,(\mathrm{eV})$
Argon (Ar)	6.0	1.2	4	40	15.8	11.6
Helium (He)	2.7	0.7	4	4	24.6	19.8
Hydrogen (H)	4.9	1.2	4	1	13.6	10.2
Xenon (Xe)	10.2	1.8	4	131	12.1	8.3
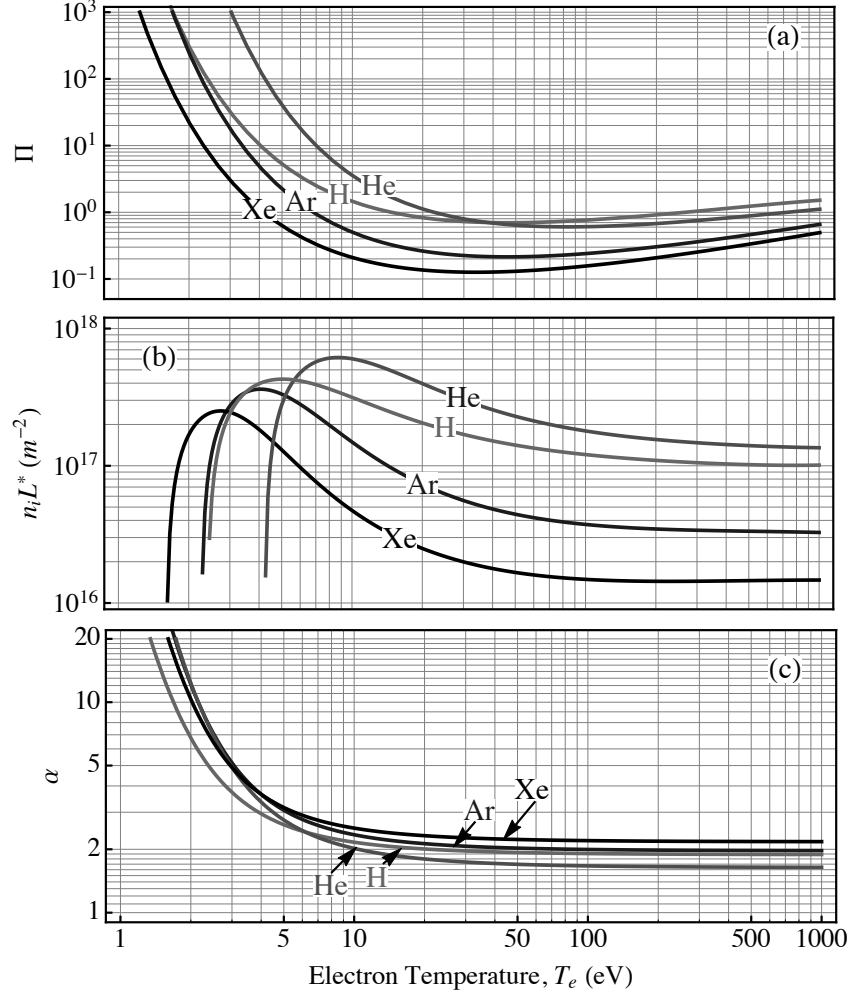
Figure 2.12: Electron temperature dependence of the (a) neutral pumping parameter, Π, (b) product of the critical channel length and plasma density, nL^*, and effective ionization energy to ionization energy ratio, α. Four different propellant gases are shown that correspond to the parameters in Tab. 2.1

We show in Fig. 2.12(a) that there is a very strong dependence of the neutral pumping parameter on both the electron temperature and propellant gas. In general, Π decreases strongly with increasing T_e until a minimum value of Π is reached, after which a slight increase is observed with T_e. This behavior is largely governed by R_{ion}. The decrease in Π reflects the fact that very few electrons exist with energies greater than ϵ_{ion} for $T_e \ll \epsilon_{\text{ion}}$. The increase in Π at high T_e is due to the decreased

ionization cross-section for high energy electrons. This result is in conflict with Ahedo and Navarro-Cavallé [17], who find $\Pi \ll 1$ for an argon plasma with $T_e > 5$. Their ionization model results in values of R_{ion} nearly two orders of magnitude greater than those predicted from Eq. (2.70). Because a reference is not included with their ionization model, we were unable to determine the exact cause of this discrepancy.

It is interesting to note that, while our scaling laws suggest $\Pi \ll 1$ is required for high η_m, Π is limited to a minimum value that is inherent to the propellant gas. The heavier propellant gases generally exhibit the lowest values of Π, which can be attributed to their low ionization energies. Hydrogen is an exception to this rule, however, as the minimum value of Π for hydrogen is greater than that of argon and helium due its larger CEX cross-section and low mass. The scaling of the minimum value of Π indicates that heavy propellant gases such as xenon are favorable for mass utilization in the high confinement limit.

The product of the ion density and the optimal channel length, $nL^* = v_s \Lambda_{\text{hc}}^* / R_{\text{ion}}$, is a function of only T_e and the propellant gas properties. Thus, for a given gas and electron temperature, the optimal channel length scales inversely with the plasma density. We plot the quantity nL^* in Fig. 2.12(b). For a given density, L^* exhibits a sharp increase at low T_e until a maximum value. This increase may be attributed to the dominance of CEX collisions within the channel at low temperatures. L^* decreases as T_e is further increased due to increasing R_{ion}. We saw earlier that Π increases at large T_e due to decreasing R_{ion}. The effect of decreasing R_{ion} at large T_e is not felt by the quantity $n_i L^*$, however, because it is offset by a comparable decrease of Λ_{hc}^*. We note that this parameter also favors the use of heavier propellant, with the optimal channel length for xenon being around an order of magnitude less than that of helium for the same density.

The ratio of the effective ionization energy to the ionization energy, $\alpha \equiv \epsilon_{\text{ion}}' / \epsilon_{\text{ion}}$, was shown by Dugan and Sovie [103] to depend on the dimensionless parameters

$\xi \equiv \epsilon_l/\epsilon_{\rm ion}$ and $T_e/\epsilon_{\rm ion}$. Here, ϵ_l is the energy level of the first excited state. This dependance is reproduced by the following equation [17]

$$\alpha \equiv \frac{\epsilon'_{\rm ion}}{\epsilon_{\rm ion}} = c_1(\xi) \exp\left[c_2(\xi)\frac{\epsilon_{\rm ion}}{T_e}\right] + c_3(\xi), \tag{2.71}$$

where the coefficients $c_j(\xi)$ depend on the parameter ξ. Using a least squares fit of Eq. (2.71) to the numerical results of Dugan and Sovie for $\xi \in [0.4, 0.8]$, we find that the fitting parameters can be approximated to within a few percent by the following functions

$$c_1(\xi) = 246.7 \exp(-13.6\xi) + 0.4, \tag{2.72}$$

$$c_2(\xi) = -1.9\xi + 1.8, \tag{2.73}$$

$$c_3(\xi) = -4.3\xi + 4.7. \tag{2.74}$$

Eqs. (2.71)-(2.74) may then be used to estimate $\epsilon'_{\rm ion}$ as a function of T_e for a particular gas using $\epsilon_{\rm ion}$ and ϵ_l. These values are tabulated in Tab. 2.1 for common propellants.

We show in Fig. 2.12(c) the dependence of α vs. T_e for various gases. The general trend is gas-independent, with α strongly increasing with decreasing T_e at low temperatures. This indicates that within this regime energy is preferentially deposited into excitation modes as opposed to ionization. The value of α approaches an asymptotic value for large T_e. A transition occurs between these two regimes around $T_e \sim 5$ eV, beyond which only small decreases in α can be achieved. The asymptotic value of α is slightly higher for the heavier gases, however, this difference is small compared to the difference in $\epsilon_{\rm ion}$.

2.3.2 Theoretical performance limit

We are now in a position to answer from a theoretical standpoint the question we posed in the introduction to this thesis: under what conditions, if any, is it possible

to efficiently produce thrust using an electron-driven magnetic nozzle? Ignoring the losses in the plasma source ($\eta_{\mathrm{ps}} = 1$) and channel ($\eta_c = 1$), and assuming zero plume divergence ($\eta_{\mathrm{div}} = 1$), we seek the upper limit to the thrust efficiency as a function of the electron temperature. We will show that T_e can be used to determine the I_{sp} in the high-confinement limit. From this relation, we obtain an upper bound of η_T vs. I_{sp}.

Using Eq. (2.13) and (2.27), we can write thrust efficiency upper bound, $\eta_T^* = \eta_{m,\mathrm{hc}}\eta_{\mathrm{conv}}$, in terms of the MN scaling parameters,

$$\eta_T^* = \left(\frac{1 + \eta_{m,0}\Pi}{1 + \Pi}\right)\left(1 + \frac{2}{\gamma_e g_u^2}\frac{\epsilon'_{\mathrm{ion}}}{T_e}\right)^{-1}. \tag{2.75}$$

Here, the first term in parentheses is the contribution of the mass utilization efficiency and the second term is the thermal conversion efficiency. We plot η_T^* in Fig. 2.13 along with each of its components as a function of T_e. Here, we chose the value $\eta_{m,0} = 0.2$ to correspond to an ionization fraction representative of helicon [44, 81, 82] and ECR [83, 84] plasma sources. Furthermore, we let $\gamma_e = 1.2$ – a value that falls between isothermal and adiabatic expansion, for which we will lend experimental support in Chapter 5.

We see that the loss of particles to CEX collisions and energy to collisional excitation and ionization produces a low thrust efficiency limit at low temperatures. As the temperature increases, the relative importance of CEX collisions decreases along with the energy deposited into excitation modes. Furthermore, the amount of energy recovered during thermal expansion exceeds the energy lost to excitation and ionization, thus drastically increasing η_T^*. The decreased ionization rate coefficient at very high temperatures yields a greater number of fast neutrals, decreasing both $\eta_{m,\mathrm{hc}}$ and η_T^*. The balance between increasing η_{hc} and decreasing $\eta_{m,\mathrm{hc}}$ produces a maximum value of $\eta_T^* \approx 0.8$. For the example in Fig. 2.13, this value corresponds to $\eta_T^* \approx 0.8$ for
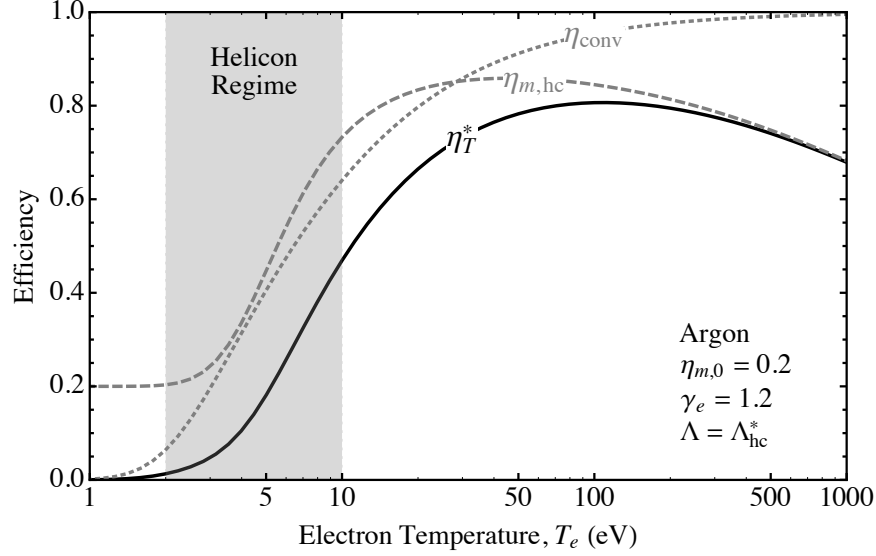
Figure 2.13: Thrust efficiency upper bound, η_T^*, versus electron temperature, T_e, for a high-confinement channel. Also shown are the mass utilization efficiency, $\eta_{m,\mathrm{hc}}$, and nozzle conversion efficiency, η_{conv}. The shaded region corresponds the the temperature range inherent to helicon plasma sources.

$T_e \approx 110$ eV. The electron temperature inherent to helicon plasma sources falls within the range $T_e \sim 2 - 10$ eV, depending mainly on the pressure within the chamber [46] and applied RF power [104]. In light of this fact, it is no surprise that the measured thrust efficiency of HPTs has yet to exceed a few percent.

In reality, radiative losses and losses associated with higher ionization states become important at high T_e [87]. These effects will tend to decrease the maximum value of η_T^*, shift its location to lower T_e, and increase the rate at which η_T^* falls off at high temperatures. A detailed examination of these processes requires a complex model for the different excitation, de-excitation and ionization processes in the plasma, including knowledge of the different rates for each process, and is therefore beyond the scope of this thesis.

We examine the influence of the propellant gas on η_T^* vs. T_e in Fig. 2.14(a). Here, the preferred traits of xenon propellant that we found in Sec. 2.3.1 conspire to produce the largest value of η_T^*. Xenon is closely followed by argon, while helium has a

significantly lower value of η_T^*. The difference among the nobel gases is due primarily to their disparate ionization energies. Hydrogen, however, has an ionization energy lower than both argon and helium. The large CEX cross-section of hydrogen relative to the heavier nobel gases results in a lower mass utilization efficiency, which produces the lowest value of η_T^*.

While the maximum values of η_T^* among all of the gases considered here occur within a small range of T_e ($\sim 70 - 120$ eV), their different atomic weights imply that the specific impulses at which these maxima occur should vary greatly. We show in Fig. 2.14(b) curves for η_T^* vs. I_{sp} obtained using the same parameters in Fig. 2.14(a). We see that the maximum values of η_T^* for xenon and argon occur at
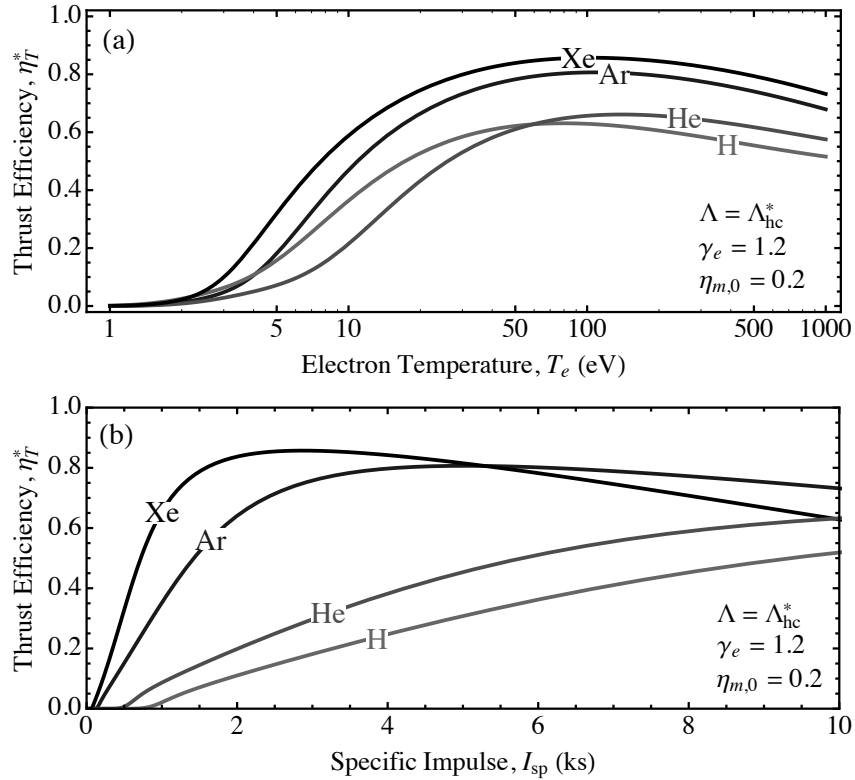

Figure 2.14: Scaling of the thrust efficiency upper bound, η_T^*, with (a) the electron temperature, T_e, and (b) the specific impulse, I_{sp} for the four propellant gases described in Tab. 2.1.

$I_{\mathrm{sp}} \sim 2.8$ ks and $I_{\mathrm{sp}} \sim 5.1$ ks for argon, respectively. It is interesting to note that the curves are relatively flat near these values, with η_T^* in excess of 95% of its maximum value within the ranges $I_{\mathrm{sp}} \sim 1.6 - 5.4$ ks for xenon and $I_{\mathrm{sp}} \sim 3.1 - 8.5$ ks for argon. The implication is that MNs may offer versatility in regards to the operating I_{sp}, in contrast to many electric propulsion systems that are restricted to a narrow range [87]. From a mission design standpoint, the decreased efficiency associated with increased ionization energy for argon may be offset by its ability to operating over a wide range of high-I_{sp}. However, operation at low-to moderate-I_{sp} requires the use of a heavier gas such as xenon. Krypton should also be a good alternative to both argon and xenon at moderate-I_{sp}. In addition to their low thrust efficiencies, the optimal specific impulse for the lighter gases exceeds 10 ks, which is much too large for near-to-far term electric propulsion missions.

Our model can be used to guide the initial design of a thruster. We take $T_e = 50$ eV and assume $\eta_{\mathrm{div}} = 0.8$, $\eta_{\mathrm{ps}} = 0.9$, $\eta_{m,0} = 0.2$, and $\gamma_e = 1.2$. For a thruster operating on Xenon, we find using Fig. 2.14 that $\eta_T \approx 0.6$ and $I_{\mathrm{sp}} \approx 2$ ks. Assuming a 5 kW thruster, the thrust and mass flow rate are $F \approx 300$ mN and $\dot{m} \approx 16$ mg/s. Using our model, $\eta_m \approx 0.9$. This implies that the mean density in the channel can be found from $nR^2 \approx 1 \times 10^{15}$ m^{-1}. Furthermore, from Fig. 2.12, we know $nL^* \approx 2 \times 10^{16}$ m^{-2}. The geometry of the channel must then satisfy $R^2/L \leq 0.1$ m. If we assume a channel radius of $R = 3$ cm, we find $L^* \approx 1$ cm and $n \approx 10^{18}$ m^{-3}. Because we want $L > L^*$, we can chose $L = 2$ cm. We note that, at high temperatures such as this example, a long channel is not required, which further motivates operation under these conditions. From Fig. 2.11, we see that the magnet radius should be around 30 cm in order for $\eta_{\mathrm{div}} = 0.8$, which is quite large from a systems standpoint. The magnetic field strength can be determined from the requirement of high confinement. This can be found from the condition $Pe_{\mathrm{an}} \gg 1$. For ambipolar diffusion assuming Spitzer resistivity [2], the required magnetic field is extremely low with $Pe_{\mathrm{an}} \sim 1$
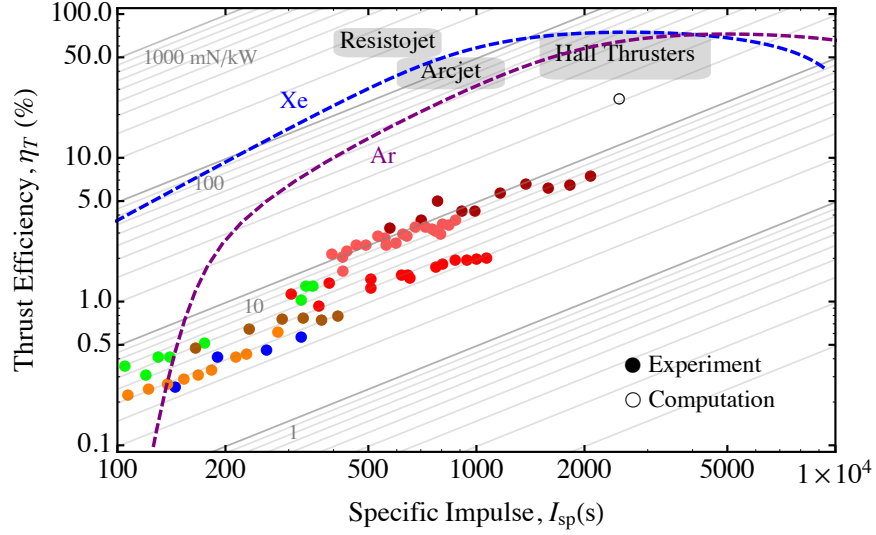
Figure 2.15: Comparison of the thrust efficiency upper-bounds of xenon and argon with established electric propulsion systems and the state-of-the art in HPTs. Figure is adapted from Fig. 1.5

at $B \sim 1$ G. Turbulent electron Bohm diffusion [105], on the other hand, requires $B \gg 70$ G for high confinement. The $\beta < 1$ constrain similarly demands $B \gg 70$ G. Therefore, a magnetic field of a few hundred Gauss is required. The discrepancy between the requirements for classical and turbulent diffusion highlights the importance of understanding the dominant diffusion mechanism in the channel region.

We return to the direct thrust measurements of state-of-the-art HPTs presented in Sec. 1.2. In in Fig. 2.15, we modify Fig. 1.4 to include the scaling of η_T^* vs. I_{sp} obtained from our model for xenon and argon. Again, we see that these two propellants could potentially offer a wide range of I_{sp} at high η_T compared to conventional thrusters. We note, however, that the curves shown here represent maximum values for the given parameters. An actual device will have inefficiencies stemming from power coupling in the plasma source, wall losses, and plume divergence – each of which will act to lower η_T. These other sources of inefficiency could heavily degrade the performance of MN thrusters. This fact is exemplified by the computation data point in Fig. 2.15,

for which the plasma was not confined in the axial direction – a result that can be recovered by setting $\eta_{\mathrm{ps}} \sim 0.5$ in our model.

Finally, we note that our model should not be compared directly to the experimentally measured performance values in Fig. 2.15. This is because the variation of η_T with I_{sp} results from changing T_e. For the experiments, however, T_e varies by only a few percent among the different thrusters. Therefore, the trend observed in the experimental measurements is a consequence of behavior external to the idealized model for η_T^*. Rather, this trend is more likely explained by improved antenna-plasma coupling (increased η_{ps} and $\eta_{m,0}$) and confinement (increased η_c). However, a comparison of the experimental measurements with the theoretical curve does serve to emphasize the need for significant performance improvements before HPTs become a competitive electric propulsion system.

2.4 Chapter summary

Using simplified theoretical models, we have derived here analytical equations for the performance of the channel and MN regions of electric propulsion systems that use a MN for propellant acceleration. The channel model combines two previously known scaling parameters, Λ [17] and Π [68], into a simple functional equation for the mass utilization and channel efficiencies. We identified a third dimensionless parameter, Ψ, that governs the transition from a low confinement to high confinement regime, and derived expressions for the optimal channel length in each of these regimes.

We derived an equation for the thermal conversion efficiency of the nozzle, which adds the effect of polytropic electron cooling to previous expressions [11, 94]. We developed an analytical solution to the 2D MN expansion model of Ahedo and Merino [23]. Using this solution, we examined the scaling of the divergence efficiency with the ratio of the plasma radius to magnet radius, density profile uniformity, and ex-

haust ion Mach number. The scaling laws obtained from this model suggest that the addition of an extra magnet to increase the ion Mach number before exhausting the plasma may decrease the divergence of the plume, but at the cost of additional weight and system complexity.

The results from our model offer insight into the practical use of MNs for electric propulsion. The requirement of an ion beam energy much greater than the effective ionization energy for efficiency MN operation creates the need for sources capable of forming plasmas with electron temperatures in the range of tens to hundreds of electron volts – a fact that calls into question the efficacy of helicon plasma sources for MN plasma propulsion. The specific impulses associated with this range of temperatures rules out lighter propellant gases like hydrogen and helium, and instead favors heavier gases such as argon and xenon.

Because of the simple nature of our model, the scaling laws derived here depend on a number of free parameters. Notably, the form of the diffusion coefficient has a large role in the confinement of the plasma [17, 72]. Additionally, the ion acoustic velocity, ion beam energy and electron heat conduction terms all depend on the value of the electron polytropic index. Finally, the MN expansion model assumed the plasma remained confined through the turning point of the magnetic field. The remainder of the thesis will be devoted to experimental investigations designed to examine these processes in more detail.

Chapter 3

Experimental Setup and Diagnostics

Our experimental investigations aim to understand the fundamental dynamics of plasma flow through a magnetic nozzle, and to compare the results with our theoretical scaling laws. We will emphasize the influence of the applied magnetic field strength, magnetic topology, and channel length on the mass utilization efficiency, electron thermodynamics, and plume divergence. To this end, we designed a versatile helicon plasma source to be combined with electromagnetic coils to form a magnetic nozzle. This chapter provides an overview of the experimental setup and diagnostics used throughout the remainder of the thesis.

3.1   Plasma source and channel

In Chapter 2 we called into question the efficacy of helicon plasmas for efficient MN plasma propulsion due to their low electron temperatures. Our decision to build a MN experiment around a helicon plasma source was based on the availability of resources in our lab, and the fact that we are not developing a thruster, but rather seeking fundamental insight into MN physics. Unfortunately, because we are limited
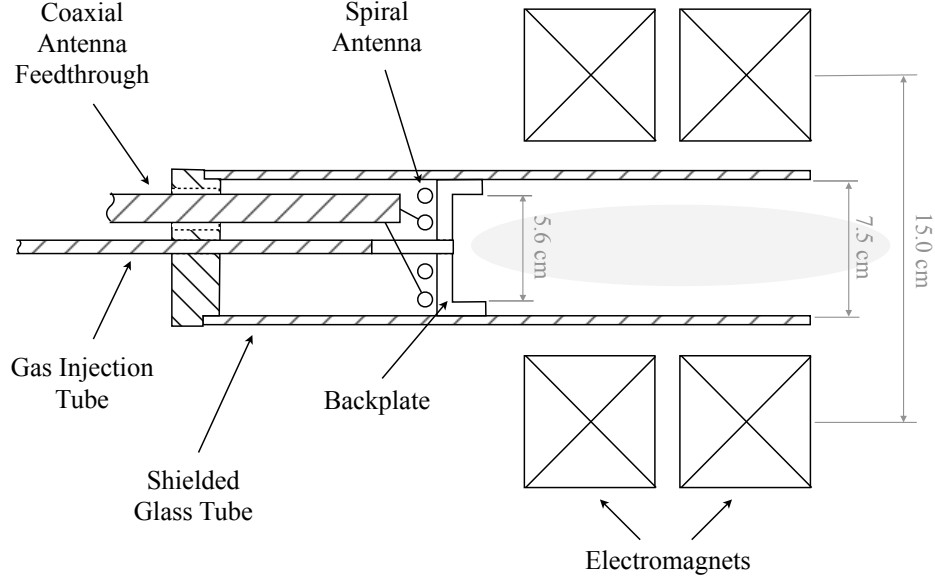
Figure 3.1: Schematic of the flat-spiral antenna RF plasma source.

to a small range of T_e, this prevents us from verifying the predicted scaling of η_T^* vs. $I_{\rm sp}$ shown in Fig. 2.14. We focus our experimental efforts instead on developing a deeper understanding of the physical processes that are fundamental to the various components of η_T [Eq. (1.5)].

The plasma source (PS) and channel (Fig. 3.1) consist of a 7.5 cm inner diameter, 30.5 cm long tube of borosillicate glass mounted concentrically inside two electro-magnetic coils. The tube is wrapped with grounded copper mesh to prevent stray RF fields outside of the device [106]. The entire assembly is mounted in a vacuum chamber on a flat plate that is attached to the end of a swinging-arm thrust stand, which will not be used in this thesis.

We use a two-turn spiral antenna positioned within the glass tube to excite the plasma. The antenna is not mechanically connected to either the PS or any components on the thrust stand. Using an alumina injection tube, gas is fed through the center of a Macor backplate that isolates the plasma from the antenna. The backplate

has a 5.6 cm inner diameter recession. All of the experiments reported in this thesis were conducted using Argon as the working gas.

The RF signal is produced by an Agilent 8648B signal generator. An ENI 2100L pre-amplifier steps the signal up to approximately 20 W, which is fed into an Alpha 9500 linear amplifier capable of producing 1.5 kW. An Alpha 4520 digital wattmeter is used to monitor the standing-wave ratio (SWR) and determine the power delivered to the matching network/antenna (P_D). This system is capable of generating RF power over a range of frequencies, however, we limit our tests to 13.56 MHz.

The power is transferred to the antenna via an L-type impedance matching network [107] that is mounted rigidly inside of the vacuum chamber and mechanically isolated from the thrust stand. The matching network consists of two Comet vacuum-variable capacitors with a range of $5 - 500$ pF. Each capacitor is rated at 5 kV. The experiment was performed with a reflected power between $4 - 20\%$ of the incident power. We designed the matching network such that the antenna leads are mounted on two copper rail electrodes that are aligned parallel to the axis of the device to allow adjustment of the axial position of the antenna. Furthermore, the Macor backplate and gas injection tube may be translated axially to remain next to the antenna. This design allows for adjustment of the axial position of the antenna and gas injection location, and therefore the channel length, within a 13 cm range.

3.2   Magnetic nozzle

Two electromagnetic coils were built to form the magnetic nozzle. The electromagnets were made by wrapping 144 turns (12×12) of AWG 10 square, copper magnet wire wound around an aluminum mandrel. The mean current radius was measured to be $r_c = 7.51$ cm, which corresponds closely to the physical radius of the center of the
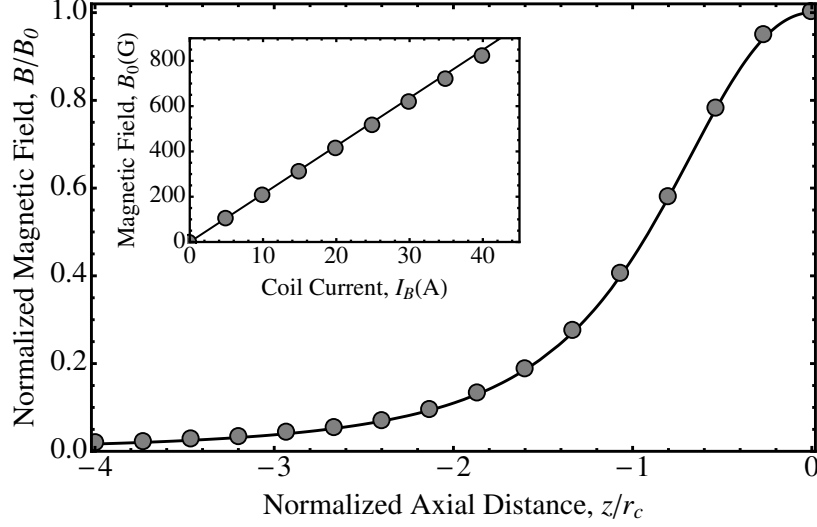
Figure 3.2: Axial variation of the magnetic field strength, B, relative to it's value at the throat, B_0. The inset shows the dependence of B_0 on the magnet current, I_B. Measured quantities are shown as circles while the black line indicates the theoretical prediction.

copper windings. The magnets are powered using an Amrel SPS32 DC switching power supply, and are each capable of handling up to 50 A of current.

The magnets were designed such that they may move independently with respect to each other and the glass tube, thus allowing control over the physical and magnetic geometries of the PS. A single configuration is used throughout the duration of this experiment (Fig. 3.1) whereby the magnets are connected rigidly together with an axial separation of 4.5 cm between their effective centers.

Gaussmeter measurements of the relative magnetic field strength along the nozzle axis are shown in Fig. 3.2. The magnitude of the maximum magnetic field as a function of the coil current, I_B, is also shown in the inset. The solid black lines in Fig. 3.2 result from approximating the two magnets as single loops of current with radius r_c. Continuing with this approximation, the surfaces of constant magnetic flux are shown in Fig. 3.3 as dashed lines. The colored lines correspond to the different injection planes and bounding magnetic flux surfaces used throughout the experiment.
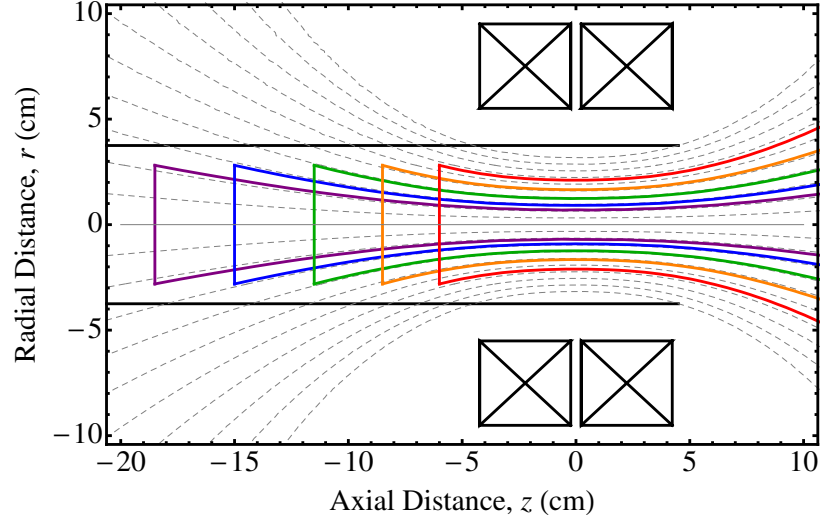
Figure 3.3: Magnetic flux contours (dashed) are shown along with the flux contours corresponding to the plane of the following injection locations: $L_{bp} = 6.0$ cm (Red), $L_{bp} = 8.5$ cm (Orange), $L_{bp} = 11.5$ cm (Green), $L_{bp} = 15.0$ cm (Blue), and $L_{bp} = 18.0$ cm (Purple).

3.3   Vacuum chamber

The plasma flow is exhausted into the EPPDyL's Large Dielectric Pulsed Propulsion (LDPP) vacuum chamber (Fig. 3.4). The cylindrical chamber is made out of fiberglass and measures 8 ft. in diameter and 25 ft. in length. The chamber is evacuated using two mechanical Stokes roughing pumps, a roots blower, and a 48 inch diameter CVC diffusion pump rated at 95,000 l/s of pumping capacity. The facility is also equipped with liquid nitrogen (LN_2) baffles to further reduce the pressure and halt contamination due to back streaming diffusion and roughing pump oil. Pressure is measured using a Varian ConvectTorr vacuum gauge and two Varian 525 cold cathode gauges connected to a Varian L8350 multi-gauge controller.

The vacuum system has a minimum base pressure of 0.2 μTorr, however, vacuum leaks restricted the base pressure of the present experiments to 20 μTorr without the LN_2 baffles and 0.9 μTorr with the LN_2 baffles. We show in Fig. 3.5 how the steady-state operating pressure of the tank varied as a function of the mass flow rate into the

PS. These measurements were made using cold cathode gauges mounted in the front (near the PS) and rear (near the diffusion pump) of the chamber. As expected, the operating pressure increases with the mass flow rate, and is generally higher towards the front of the tank.

We also show in Fig. 3.5 the expected gas pressure within the PS. With the exception of very low mass flow rates, we see that the PS pressure is an order of magnitude larger than the chamber pressure for all cases. Therefore, we are able to experimentally characterize the PS without the need for the LN_2 baffles. For measurements of the exhaust plume, however, the CEX mean free path with the background gas can approach the same order as the expansion length scale, and are therefore required to run the baffles to minimize facility effects on measurements in this region.

Figure 3.4: Photograph of the LDPP vacuum chamber, or "orange tank".
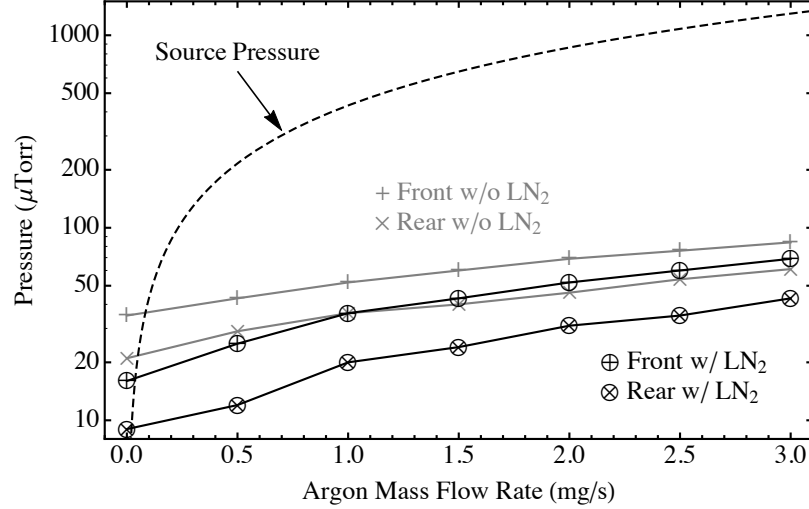
Figure 3.5: Cold cathode gauge measurements of the vacuum chamber pressure at the rear and front of the tank with and without the liquid nitrogen baffles for different argon mass flow rates. The solid line shows the estimated scaling of the pressure within the plasma source.

3.4 Plasma diagnostics

Four plasma diagnostics are used throughout our experiments (Fig. 3.6): an RF-compensated Langmuir probe (RF-LP), emissive probe (EP), Faraday probe (FP), and retarding potential analyzer (RPA). These diagnostics are described in Secs. 3.4.1-3.4.5. Depending on the desired measurement, one or multiple probes were mounted on a probe positioning system (PPS) that allows 2D positioning of the probe tip. A more detailed description of the PPS is provided in Sec. 3.4.5.

3.4.1 RF-compensated Langmuir probe

We constructed the RF-LP according to the design by Sudit and Chen [108]. It is well-known that an oscillating plasma potential has a non-linear effect on the current-voltage characteristic of a Langmuir probe [109]. To combat this effect, large RF impedances are introduced to the circuit by placing chip inductors near the probe tip with self-resonant frequencies near the operating frequency (13.56 MHz) and first

Figure 3.6: Photograph of the RF-compensated Langmuir probe (RF-LP), emissive probe (EP), Faraday probe (FP), and retarding potential analyzer (RPA).

harmonic (27.12 MHz). Furthermore, we create a floating electrode by winding tungsten wire around the alumina tube that houses the probe. The electrode is connected to the probe tip through a capacitor to allow the tip to follow the RF fluctuations. The external electrode and probe tip can be seen in Fig. 3.6. The probe tip is made of 0.25 mm diameter tungsten wire and has an adjustable length. The wire is friction-fit to a stainless steel tube inserted in an alumina tube. A 0.1 mm wide by 0.5 mm deep recess exists between the probe tip and alumina jacket so that the tip remains electrically isolated from any conductive coating that could potentially be sputtered onto the jacket. Using high temperature solder, we connected the steel tube to the RF compensation circuit within a concentric, larger diameter alumina tube.

The source of the bias voltage signal is a three-stage phase shift oscillator. This oscillator drives a Kepco 1000M bi-polar operational power/amplifier (BOP) to produce a 5 Hz, 140 V peak-to-peak waveform. The BOP is connected to the LP compensation circuit using BNC cables on each side of a vacuum feedthrough. The probe current is measured across the 1 kΩ resistor of a low-pass filter with a cutoff frequency of 16
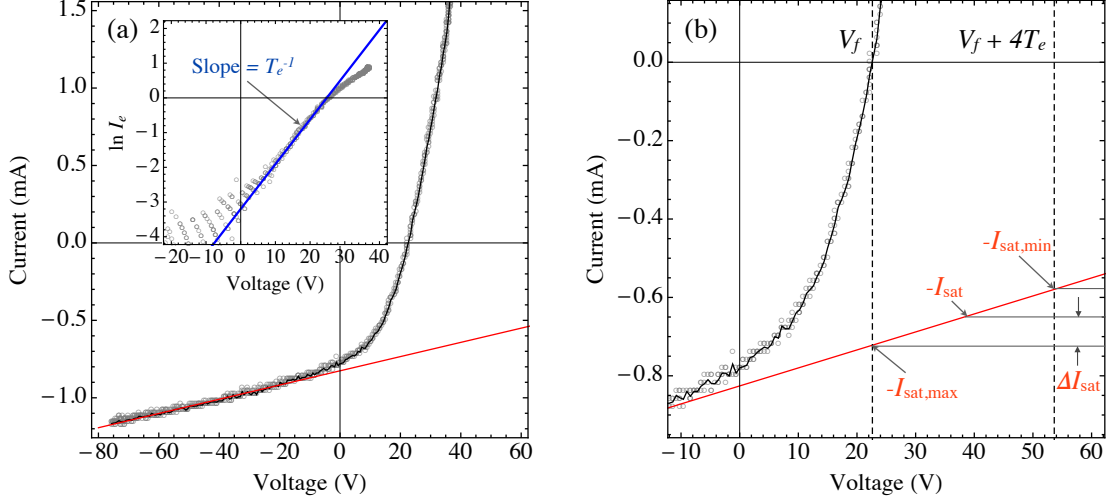
Figure 3.7: (a) Typical RF-LP current-voltage trace. (b) Enhanced version of (a) that demonstrates our method for calculating the ion saturation current, I_{sat}.

kHz. Depending on the fidelity of the signal, the voltage and current traces were averaged over somewhere between four and 64 periods, and displayed on a Tektronix TDS 3034B digital oscilloscope. For cases in which hysteresis was observed in the current signal, the average of the current for both the up-and down-sweeps was taken.

Analysis

A typical current-voltage (IV) characteristic is shown in Fig. 3.7(a). We avoided sampling in the electric saturation region of the Langmuir probe trace to prevent damage to the probe and improve the signal to noise ratio. The electron current to the probe, I_e, was found by fitting a linear line to the ion saturation region of the IV trace and subtracting this from the total current. As we demonstrate in the inset of Fig. 3.7(a), the electron temperature (in eV) is equal to the inverse of the slope of the linear region of the $\ln I_e$-V graph [110]. From the literature [108, 111] we estimate a 10% error in the temperature measurement for the RF-LP.

The plasma density, n, was found from the ion saturation region of the IV curve [110]. Sheath expansion effects of cylindrical LPs have previously been accounted

for in the literature using linear extrapolation of the I-V curve in the ion saturation region to either the floating potential, V_f [112], or the plasma potential V_p [113]. We make the rough assumption that $V_p = V_f + 4T_e$, and obtain I_{sat} from the average of these two methods. We take the error in I_{sat} as one-half of the difference between the resulting values. Using this method to obtain I_{sat}, we calculated the density from the standard Bohm approximation [114],

$$n = \frac{I_{\text{sat}}}{0.61 e A_p \sqrt{T_e/m_i}}, \tag{3.1}$$

where A_p is the area of the probe tip. We determined the error in the density measurement by propagating the errors in I_{sat}, T_e, and A_p ($\sim 5\%$).

3.4.2   Emissive probe

Due to hysteresis effects and the presence of RF potential fluctuations, conventional methods for determining the plasma potential from the Langmuir probe IV curve can exhibit significant errors. To avoid these complications, we measured the plasma potential using an emissive probe (EP) [115]. Our emissive probe was made by friction fitting a tungsten filament between two copper wires separated from each other by the wall of a two-bore alumina tube [116]. We heated the filament to electron emission using a half-wave rectified AC current and recorded the floating potential of the probe. Using the floating point method, the plasma potential was obtained from the rectified portion of the floating potential waveform [117]. In accordance with the larger estimates available in the literature [115], we take the measurement error of this method to be 10%.

3.4.3 Faraday probe

We measured the ion current density in the exhaust plume using a planar Faraday probe [118]. The Faraday probe consists of a flat electrode, or collector, surrounded by a guard ring – both biased to -27 V. Beam ions impinge on the collector and are neutralized by electrons that flow to the surface, thus forming a current. The collector current was measured through a 10 kΩ load resistor. A 16 kHz low pass filter was used to decrease RF noise. The guard ring serves to prevent low energy ions from being collected beyond the line of sight of the probe [119]. The ion current density was obtained by dividing the measured current by the area of the collector.

3.4.4 Retarding potential analyzer

We borrowed a four-grid retarding potential analyzer (RPA) [120] to directly measure the ion energy distribution function (IEDF). Using the same electronics as the RF-LP, the IV trace of the RPA was obtained by applying a voltage sweep between 0 V and 80 V to the ion repelling grid and measuring the current to the grounded ion collection disc. A DC bias of -15 V was applied to each of two electron repelling grids to minimize the effect of secondary electrons. The fourth grid, located at the entrance of the device, was left floating to shield the plasma from the other three grids.

A typical IV curve from our measurements is shown in Fig. 3.8. The collector current, I_c, remains nearly constant at low bias voltages as the majority of ions have enough energy to reach the collector. As the bias voltage increases, a drop in I_c is observed that corresponds to the reflection of incoming ions. Very few ions reach the collector for very large bias voltages. We obtained the IEDF from the derivative of the IV trace [114],

$$f_i(V) \propto \frac{1}{\sqrt{V}} \frac{dI_c}{dV},$$

(3.2)
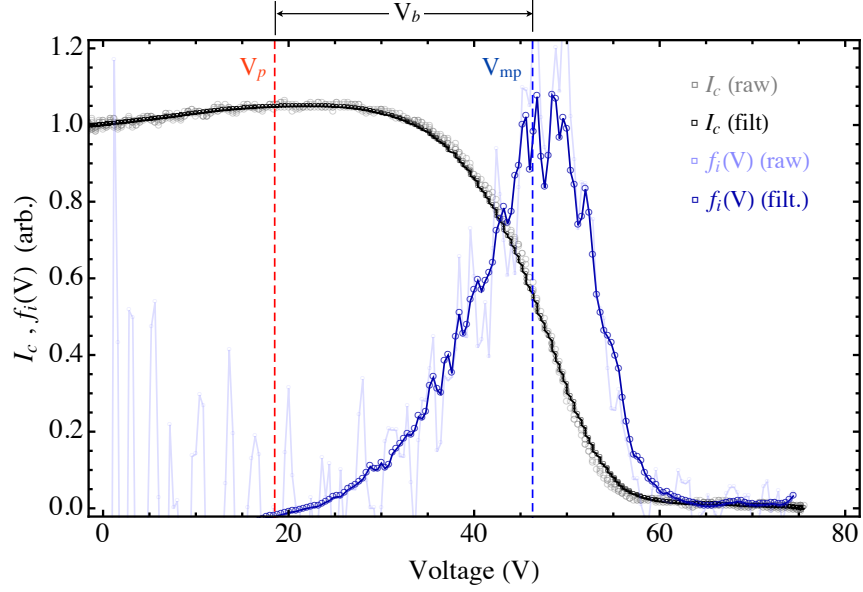
Figure 3.8: Typical raw and filtered RPA current-voltage traces. Also shown are the ion energy distribution functions that result from numerical differentiation of these signals. The ion beam voltage, V_b, is found from the difference between the IEDF most probable voltage, V_{mp}, and the plasma potential, V_p.

where V is bias voltage with respect to the laboratory ground. Because the ions enter the device at the plasma potential, V_p, a measurement of this quantity is required to determine the ion energies within the laboratory rest frame.

We observed the IEDF resulting from numerical differential of the raw IV curve to exhibit significant noise. The primary source of this noise was determined to be 60 Hz AC leakage current into our signal from to the BOP. We minimized this noise source using two methods. First, the IV curve was averaged over somewhere between four and 64 periods, depending on the signal level. Second, a numerical filter was applied during post processing of the data to eliminate the 60 Hz noise. As shown in Fig. 3.8, these techniques significantly improved the quality of the IEDF.
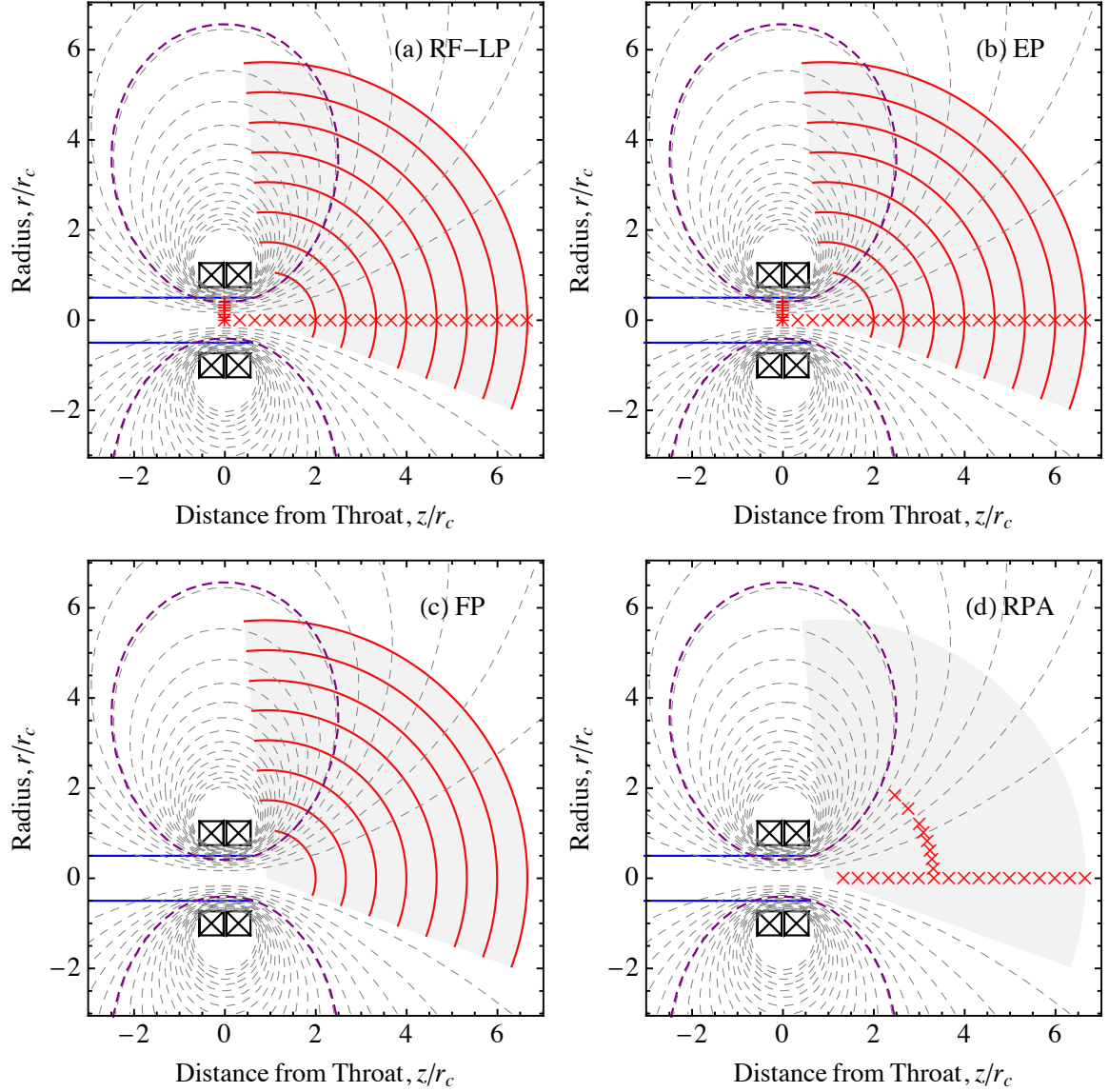
Figure 3.9: Measurement locations for the (a) RF-compensated Langmuir probe, (b) emissive probe, (c) Faraday probe, and (d) retarding potential analyzer. "×"s and "+"s denote single-point measurements along the centerline and throat plane, respectively. Measurement sweeps are shown as red lines while the gray dashed lines show the magnetic flux surfaces. The purple dashed line is the magnetic flux surface that intersects the glass chamber of the plasma source, which is shown as a solid blue line. For our experiment, $r_c = 7.51$ cm.

3.4.5 Probe positioning system

We constructed the probe positioning system (PPS) to allow accurate adjustment of the probe location within the r-z plane of the exhaust. The PPS is driven by two

independently controlled DC brush motors. The first motor controls the location of a linear transition stage upon which the probes are mounted. The second motor rotates the translation stage about a vertical axis aligned near the exit of the thruster. The location of the probe is determined using two potentiometers - one for each degree of freedom. A LabView program is used to monitor the probe location and control the relays within the motor power supply unit.

The locations at which we take measurements with each probe are depicted in Fig. 3.9. Here, "×"s and "+"s denote single-point measurements taken in the plume and radially along the MN throat plane, respectively, while solid lines indicate a measurement sweep along the line with a sampling rate determined by the specific probe. The oscilloscope was used for single point measurements, while the measurement sweeps were recorded in LabView. We see from Fig. 3.9 that, with a range in excess of 50 cm from the MN throat, the PPS allows the characterization of regions in which the plasma and magnetic field have undergone significant expansion.

3.5   Operating modes

We found the PS to operate in three distinct modes (see Fig. 3.10) depending on the argon mass flow rate, applied magnetic field strength, injection location, and RF power. For convenience sake, we refer to these modes according to the commonly observed modes in RF plasmas [46]: the capacitive mode (E), inductive mode (H) and helicon wave mode (W). We will show that the characteristics of each mode agree qualitatively with those observed in the literature, however, we emphasize the fact that we did not make wave measurements to discern the E, H, and W modes [121].

The discharge was most commonly ignited in the E mode, which was distinguished by a faint glow with electron temperatures and ion densities on the order $T_e \sim 10$ eV and $n_i \sim 10^{16} - 10^{17}$ m^{-3}. For fixed P_D and $\dot{m}$, as we *decreased* the magnetic field

84
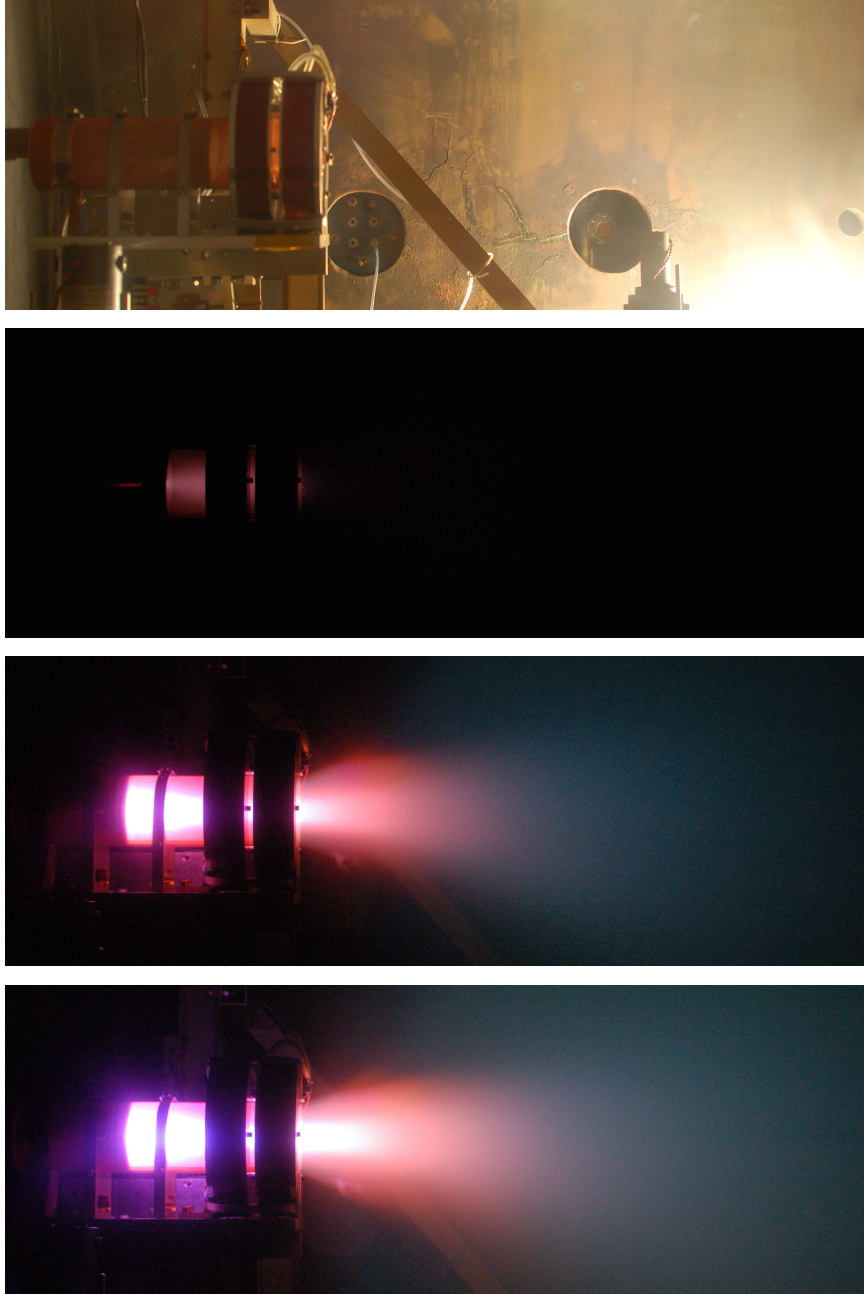
Figure 3.10: Photographs (f/7.1, 1/30 s exposure) of the plasma source (top) operating in the capacitive (middle-top), inductive (middle-bottom), and helicon wave (bottom) modes.

below a certain threshold the plasma would jump into either the H or W mode, leading to an impedance mismatch that had to be corrected using the tuning capacitors. The plasma was observed to be much brighter in the W mode and demonstrated the "blue core" characteristic of Helicon plasmas reported in the literature [122]. The temperature and density of the W mode were measured to be $T_e \sim 5$ eV and $n_i \sim 10^{18} - 10^{19}$ m^{-3}, respectively. Finally, we observed a second impedance mismatch while increasing the magnetic field, which suggests a W-H mode transition. The H mode was slightly less bright than the W mode and did not possess a "blue core." We observed T_e to be comparable between the W and H modes, while n_i showed a slight decrease upon transitioning from the W to H mode.

We note that the density in the W mode appears lower than that of the H mode at low magnetic fields in Fig. 3.11 due to diffusion of the plasma to the PS walls prior
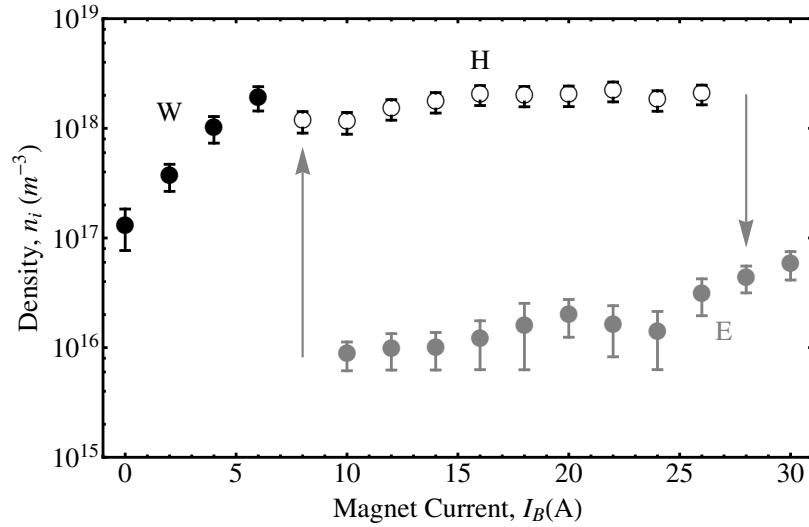
Figure 3.11: Langmuir probe measurements of the plasma density at the magnetic nozzle throat, n_i, versus magnet current, I_B, measurements indicate the presence of three distinct modes: wave mode (W), inductive mode (H) and capacitive mode (E). The operating parameters are $P_D = 500$ W, $\dot{m} = 2$ mg/s, and $L_{\mathrm{bp}} = 11.5$ cm. The arrows indicate the direction of the mode transition to and from the E mode. A similar hysteresis was not observed for the W-H transition. Note that the decreasing density of the W mode at low magnetic fields is due to diffusion of the plasma to the walls prior to reaching the probe (see Fig. 4.1(b)).

to reaching the LP. Indeed, LP measurements near the backplate reveal that the W mode densities remain a few times larger than the H mode densities in this region, which is consistent with previous studies of helicon plasma sources [122, 123].

Within a given mode, T_e increased slightly as $\dot{m}$ decreased, which agrees with previous theoretical [46] and experimental results [124]. The inverse relationship between T_e and B_0, predicted to be a consequence of improved confinement of the plasma [74, 125], was not observed in our experiment. Rather, we found T_e to be insensitive to changes in B_0 within our experimental uncertainty. We anticipate that this discrepancy may be due to the open-ended nature of our device. T_e is typically determined by the balance between ionization and particle losses within the plasma source [46]. In the limit that the loss of particles due to advection along the magnetic field dominates diffusive losses to the PS walls, the particle balance (and therefore T_e) becomes intensive to changes in B_0.

Helicon modes in low-magnetic-field RF plasmas have previously been observed in the literature [45, 126], and have been recently studied in depth by Lafleur *et al.* [127, 128, 129, 130]. A few curious distinctions between the mode transitions observed in our PS (using a spiral antenna) and those found in literature (typically with a Boswell-type antenna) are worth mentioning: (1) the W mode existed for applied magnetic fields that are an order of magnitude larger than previously observed; and (2) the density jump between E and W modes was around two orders of magnitude, compared to less than an order of magnitude reported in the literature.

Although it appears that the W mode in our experiment was stable at $B_0 = 0$ G, theory indicates that the propagation of helicon waves requires a finite background magnetic field [46]. Therefore, it is possible that a second inductive mode exists at $B_0 = 0$ G [131].

For the remainder of our experiments, unless otherwise specified, we operated the PS in the W and H modes while varying the applied magnetic field at a fixed delivered

power, $P_D = 500$ W. We performed experiments for five different backplate locations, which correspond to the following magnetic flux contour colors in Fig. 3.3: $L_{\mathrm{bp}} = 6.0$ cm (Red), $L_{\mathrm{bp}} = 8.5$ cm (Orange), $L_{\mathrm{bp}} = 11.5$ cm (Green), $L_{\mathrm{bp}} = 15.0$ cm (Blue), and $L_{\mathrm{bp}} = 18.0$ cm (Purple). Here, $L_{\mathrm{bp}} = |z_{\mathrm{bp}}|$.

Chapter 4

Channel Plasma Confinement[1]

Global models of helicon plasmas have been used to estimate the plasma density by equating the absorbed RF power to the power lost by the flux of plasma to the radial walls of the PS, and axially along the applied magnetic field [44, 46]. For propulsion applications, the power deposited into the plasma must be preferentially directed through the exhaust. This implies that the mass flux in the radial direction due to cross-field diffusion should remain much smaller that the flux due to the field-aligned advection of the plasma. The numerical model of Ahedo and Navarro-Cavallé [17] found a sharp rise in η_m at a critical applied magnetic field strength for a specified thruster geometry and fixed $\dot{m}$ and T_e, indicating a transition from a low confinement regime to a high confinement regime. Using a simplified model for the MN channel, we derived in Chapter 2 an analytical equation that describes the scaling of the critical magnetic field strength.

Although experiments have generally demonstrated better performance for HPTs with increasing magnetic field values [58, 60, 62], it is unclear to what extent the performance enhancement is due to improved plasma confinement in the PS (higher η_m) [60], or decreased outward diffusion of the plasma in the MN expansion region

---

[1]This chapter contains the experimental results presented in [73]: J. M. Little and E. Y. Choueiri, "Critical Condition for Plasma Confinement in the Source of a Magnetic Nozzle Flow," *IEEE Trans. Plasma Sci.*, Vol. PP, no. 99, 2014.

(higher C_T) [62]. The goals of this Chapter are to experimentally verify the existence of a critical magnetic field for efficient plasma confinement in magnetic nozzle plasma sources, determine using probe measurements the dimensionless scaling parameters for our experiment, and confirm the scaling law for the mass utilization efficiency derived in Chapter 2. To this end, we use visible photography of the operating thruster to give a broad overview of the plasma structure in our experiment in Sec. 4.1. These qualitative observations are then examined in depth in Sec. 4.2 using RF-LP measurements of the radial plasma structure at the MN throat. Finally, we use these probe measurements in Sec. 4.3 to estimate the mass utilization efficiency and directly compare the analytical scaling laws with experimental measurements. We provide a summary of our findings in Sec. 4.4.

4.1 Visible plasma structure

Photographs of the PS operating at various applied magnetic field strengths for $L_{\mathrm{bp}} = 11.5$ cm are shown in Fig. 4.1. At zero applied magnetic field much of the plasma remained inside the glass tube of the PS. As we increased the magnetic field the plasma migrated downstream and eventually formed a plume in the MN divergent-field. This behavior indicates that, without a magnetic field, the majority of plasma is lost to the glass walls through diffusion. Increasing the applied magnetic field decreases the radial diffusion of the plasma, allowing the plasma to advect through the glass tube opening to form a plume. We verified this notion using thermal infrared camera measurements, which qualitatively showed that the rate of heating of the glass tube near the injection location decreased inversely with the magnetic field strength.

Also shown in Fig. 4.1 are the approximate magnetic flux surfaces that intersect the glass tube at the exhaust, ψ_w, and the inner radius of the backplate at the injection plane, ψ_i. Figs. 4.1(C)-(F) show that the edge of the bright plasma core corresponded
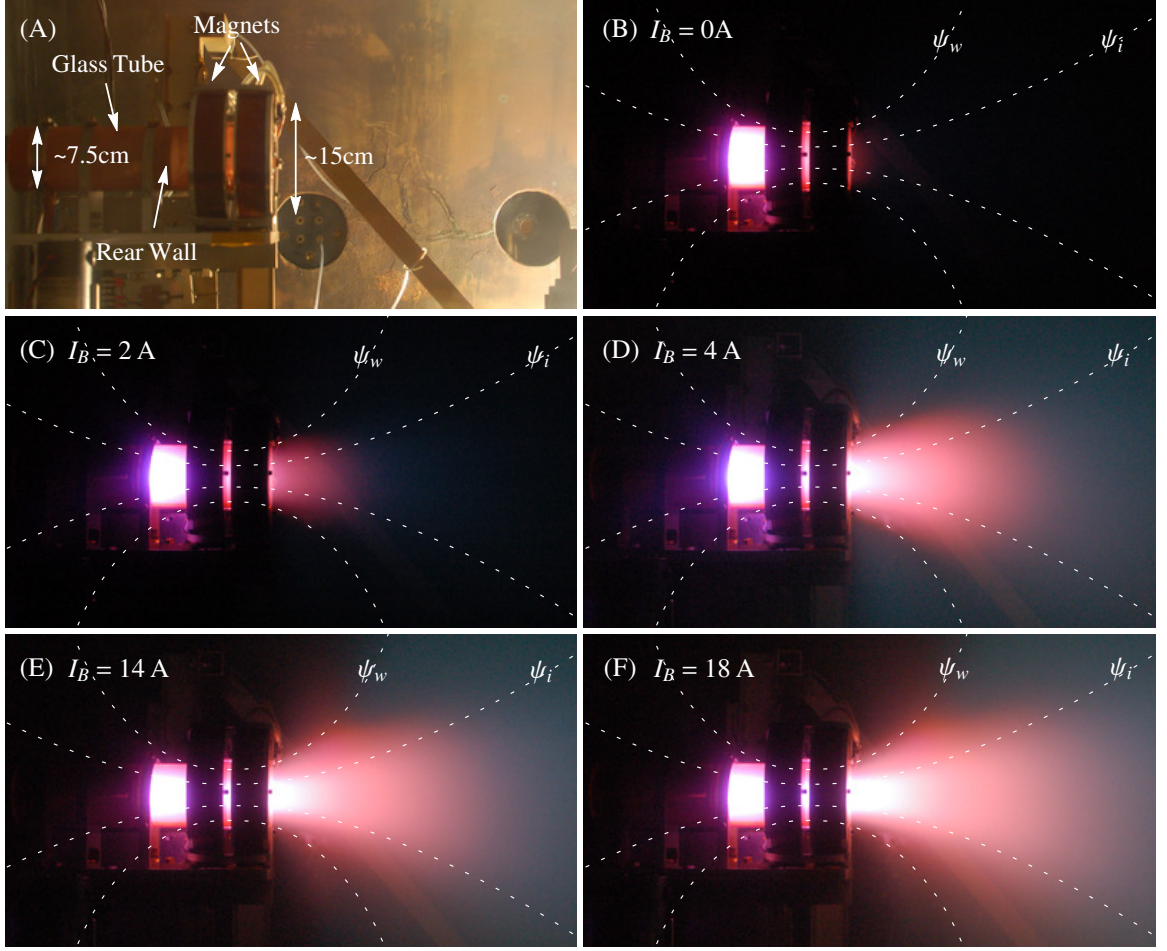
Figure 4.1: Photographs (f/7.1, 1/30 s exposure) of the plasma source (A) operating at various magnet currents, I_B (B-F). The operating parameters are $P_D = 500$ W, $\dot{m} = 2$ mg/s, and $L_{\mathrm{bp}} = 11.5$ cm (note that the backplate location shown in (A) corresponds to $L_{\mathrm{bp}} = 8.5$ cm). Photos (B-D) depict the "blue core" of the helicon mode, which is absent from the inductive mode (E-F). The dashed white lines denote the surfaces of constant magnetic flux corresponding the surfaces that intersect the glass tube at the exhaust, ψ_w, and the inner radius of the backplate recession at the injection plane, ψ_i.

roughly to ψ_i. Furthermore, as we increased I_B, the boundary of this core became even sharper, especially in the plume.

We also looked at the effect of moving the backplate on the plasma structure. The intersecting flux surface (ψ_i) compresses radially as the backplate is moved upstream (see e.g. Fig. 3.3). This explains the radial compression observed of the advective
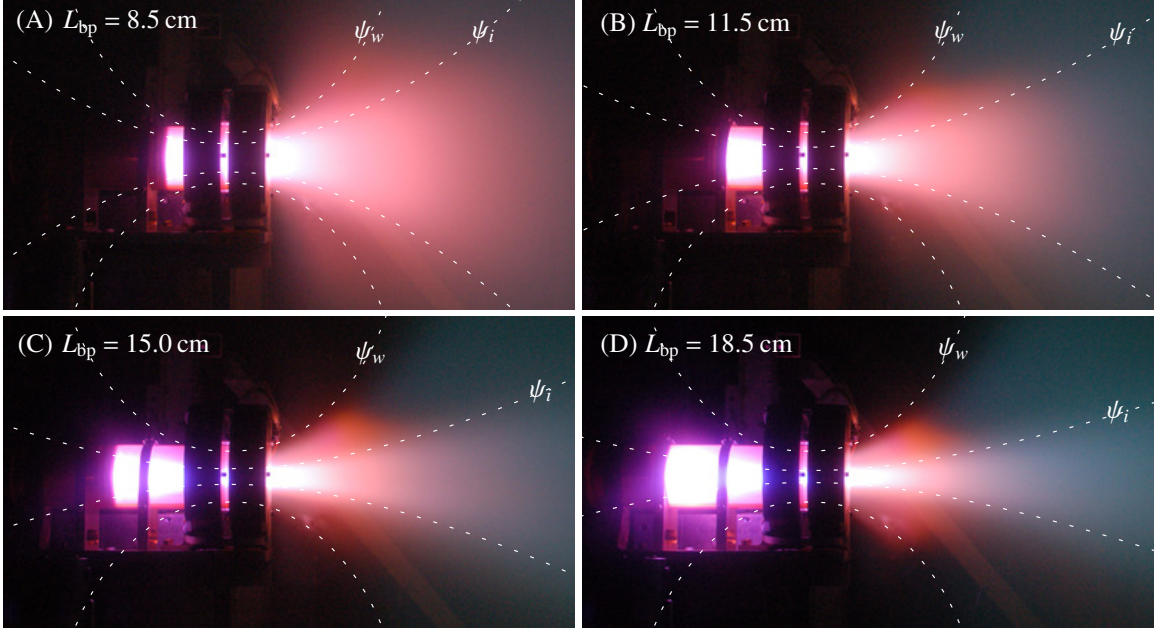
Figure 4.2: Photographs (f/7.1, 1/30 s exposure) of the plasma source operating with different injection locations, L_{bp}. The operating parameters are $P_D = 500$ W, $\dot{m} = 2$ mg/s. The dashed white lines denote the surfaces of constant magnetic flux corresponding the wall radius at the exhaust, ψ_w, and the radius of the backplate recession at the injection plane, ψ_i.

core, as seen in the photographs in Fig. 4.2. It is clear from these pictures that, as the core was compressed, the divergence of the plume decreased dramatically: a result that qualitatively agrees with MN performance models [23, 95], and suggests higher performance for larger L_{bp}.

4.2 RF-LP measurements

Using the RF-LP, we measured the plasma density and electron temperature at the MN throat as a function of the applied magnetic field. We note that the measurements contained within this chapter we made with an early version of the RF-LP that did not possess the external electrode. The main consequence is that the probe signal is filtered but not RF compensated. For this probe, we estimate a larger electron

temperature error of 25%. Furthermore, we observed slight erosion of the probe tip, from which we determine a 15% error in the probe tip area.

The results for four different backplate locations are shown in Fig. 4.3. Here, the colors of the data points correspond to the colored contours of Fig. 3.3. Furthermore, the solid data points denote W mode plasmas, while the open data points denote H mode plasmas. The W-H mode transition was assumed to occur when both the impedance match and visible emission changed abruptly as described earlier in this section. We note that the shaded region in Fig. 4.3 corresponds to an I_B-range in which the plasma was unable to remain impedance matched at $P_D = 500$ W.

In general, the plasma density at the MN throat increased with the applied magnetic field in the W mode. As I_B increased beyond a certain threshold, however, the plasma transitioned to the H mode and was marked by a slight decrease in n_i for both $L_{\mathrm{bp}} = 8.5$ cm and $L_{\mathrm{bp}} = 11.5$ cm. We suspect that this decrease indicates diminished power coupling between the antenna and plasma [46]. We observed neither a W-H nor a H-C mode transition for $L_{\mathrm{bp}} = 18.5$ cm in the magnet current range considered, $I_B \leq 32$ A.

The plasma density as $I_B \rightarrow 0$ decreased drastically (by nearly three orders of magnitude) as the distance between the injection plane and throat increased. This trend supports the notion that plasma was being lost to the walls through radial diffusion prior to reaching to probe, which was located a distance L_{bp} from the injection region. Furthermore, we found a sharp rise in n_i with the increasing magnetic field, which is indicative of the low-confinement to high-confinement transition observed by Ahedo and Navarro-Cavallé [17].

We also measured the radial dependence of the plasma density at the MN throat. These results are shown in Fig. 4.4(a) for various L_{bp}. The radial location of each measurement is normalized by the radius of the PS wall, r_w, and the densities are normalized by $\bar{n}_a$, which will be defined later. In general, the plasma density remained
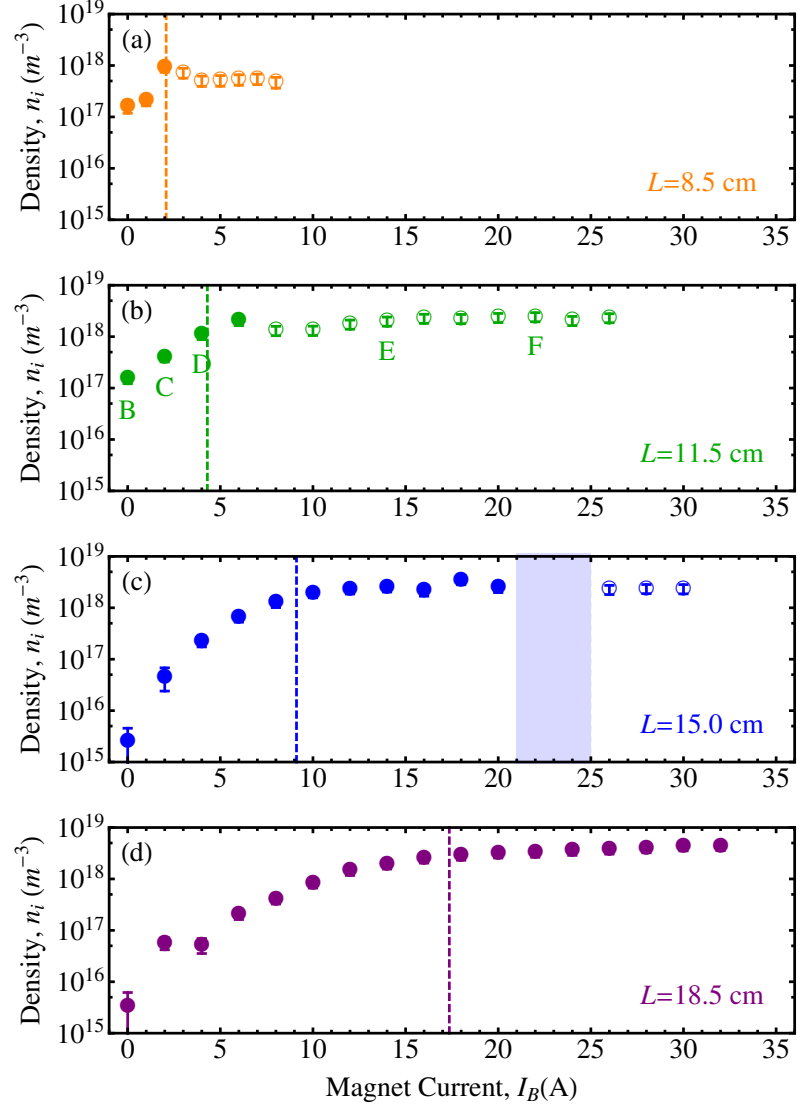
Figure 4.3: Langmuir probe density measurements at the center of the magnetic nozzle throat for $P_D = 500$ W and $\dot{m} = 2$ mg/s. The solid and open data points correspond to the W and H modes, respectively. The plasma was not stable at $P_D = 500$ W in the shaded blue region for $L_{\mathrm{bp}} = 15.0$ cm. The letters next to the data points in (b) represent the photographs shown in Fig. 4.2. The dashed vertical lines denote the magnet current required to generate the characteristic magnetic field described in Sec. 4.3.

uniform near the axis of the PS to a certain radial distance, after which the density fell off exponentially.

The visible structure of the plasma and radial density measurements support the following scenario: plasma formed in the injection region ($z = -L_{\mathrm{bp}}$) with a
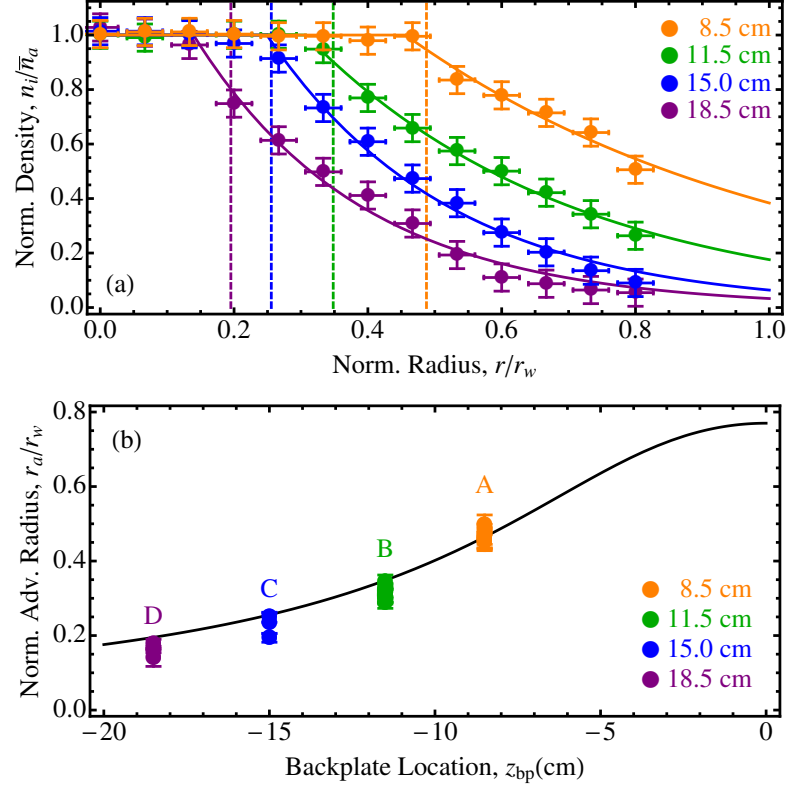
Figure 4.4: Radial Langmuir probe measurements of the (a) radial plasma density profile and (b) scaling of the radius of the boundary between the advective and diffusive regions normalized by the wall radius, r_a/r_w. The solid lines in (a) come from Eq. (4.1), while the dashed lines represent the location of r_a/r_w predicted from Eq. (4.2). The solid line is (b) also comes from Eq. (4.2). Note that the letters in (b) correspond to the photographs in Fig. 4.2.

radially uniform density profile advects along the converging magnetic field towards the throat plane ($z = 0$). The density profile at the throat remains uniform in the limit that transport is governed purely by advection along the magnetic field. However, the plasma density spreads out radially due to cross-field diffusion. We infer the radial uniformity of the density profile at the injection region from the LP probe measurements, which became increasingly more uniform as L_{bp} decreased (i.e. the probe moved closer to the injection region). Furthermore, the exponential radial dependence of the plasma density in the diffusive region is expected from the diffusion equation [100].

Guided by this physical picture, we found the following model to be appropriate to describe the plasma density profile at the MN throat:

$$n_i \left(r \right) = \begin{cases} \bar{n}_a & : r < r_a \\ \bar{n}_a \exp\left[- \left(r - r_a \right) / \delta \right] & : r > r_a \end{cases} \tag{4.1}$$

Here, r_a defines the boundary between the advective ($r < r_a$) and diffusive ($r > r_a$) regions of the plasma, $\bar{n}_a$ is the average plasma density in the advective region, and δ is the diffusive length scale. The solid lines in Fig. 4.4(a) result from a least-squares fit of Eq. (4.1) to the radial LP data.

It is clear from Fig. 4.4(a) that r_a increased inversely with L_{bp} in our experiment. For zero cross-field diffusion, the radius of the advective region at $z = 0$ is expected to scale according to

$$r_a \approx r_i / \sqrt{\Pi_B}, \tag{4.2}$$

where we have assumed $B_z \gg B_r$. Here, r_i is the radius of the injection region and $\Pi_B = B_0 / B_i$ is the magnetic mirror ratio between the MN throat and injection region.

We compare in Fig. 4.4(b) the values of r_a found from a least-squares fit of Eq. (4.1) to the radial LP data to the theoretical prediction of Eq. (4.2). Here, we normalize r_a by the radius of the PS wall, r_w. The agreement between the calculated and predicted values of r_a agrees well with the qualitative observations drawn from the photographs in Fig. 4.2.

We take a moment to explain a contradiction between the radial density profiles measured in our experiment and the Bessel function density profile commonly used in magnetic nozzle performance models [23, 95]. The Bessel function profile was adopted from the work of Ahedo [88], who showed that the radial density profile of an infinitely long cylinder of plasma was given by the zeroth-order Bessel function for both unmagnetized plasmas and magnetized plasmas in the large Hall parameter

limit. We suspect that the finite length of our PS prevents the emergence of the Bessel function profile for all but the lowest applied magnetic fields. In fact, for magnetic fields below a critical value (see Sec. 4.3), we found that the radial density profile was indeed more appropriately described by a Bessel function than the model presented in Eq. (4.1).

Finally, it is necessary to examine the role of azimuthal currents in the transfer of momentum [23, 32] from the plasma to the MN for the density profiles shown in Fig. 4.4(a). The density plateau near the axis implies that azimuthal currents are negligible within the advective core of the plasma. Therefore, we anticipate that momentum is transferred by the azimuthal current density created by the pressure gradient within the diffusive layer [23, 132]. The fact that the diffusive layer *transfers* momentum does not imply that the advective core of the plasma does not produce thrust. Rather, the strength of the azimuthal current density in the diffusive layer is proportional to the local plasma density, which is globally influenced by the expansion of both the advective and diffusive regions of the plasma [23].

4.3   Critical condition for plasma confinement

The relative importance of field-aligned advection with respect to to cross-field diffusion may be analyzed using a dimensionless, anisotropic Péclet number, which we define as

$$Pe_{\mathrm{an}} \equiv \frac{c_s/L}{D_\perp/R^2}. \tag{4.3}$$

Here, c_s is the ion acoustic speed, L is the channel length, R is the channel radius, and $D_\perp$ is the cross-field diffusion coefficient. Effectively, Pe_{an} is the ratio of the cross-field diffusion timescale to the field-aligned advection timescale.

We can use the LP measurements in Fig. 4.3 to relate Pe_{an} to the critical magnetic field. Assuming that classical collisions dominate diffusion, the cross-field diffusion

coefficient can be written as $D_\perp = \eta_\perp p_e / B^2$ [44]. Here, $p_e = n_e T_e$ is the electron pressure and $\eta_\perp \approx (100 T_{\rm ev})^{-3/2}$ $[\Omega \cdot {\rm m}]$ is the cross-field resistivity of the plasma assuming singly-charged ions [100]. We can express the anisotropic Péclet number in the injection region as $Pe_{\rm an}^i = (B_0/B_0^*)^2$, where

$$B_0^* \equiv \frac{\Pi_B}{R} \sqrt{\frac{p_e L \eta_\perp}{c_s}}, \tag{4.4}$$

is a characteristic magnetic field. We consider the injection region because it represents the location of minimum $Pe_{\rm an}$ for our convergent-field MN geometry.

Setting $R = r_w$, $L = L_{\rm bp}$, $n_e = 2 \times 10^{18}$ m^{-3} and $T_{\rm ev} = 5$ eV in Eq. (4.4) we can calculate the characteristic magnetic field for the data in Fig. 4.3. According to Fig. 3.2, the magnet current corresponding to B_0^* for our experiment is approximately I_B^* [A] $\approx B_0^*$ [G] $/21$. The value of I_B^* is shown for different values of $L_{\rm bp}$ in Fig. 4.3 using a colored dashed line. From this figure we see that B_0^* corresponds to the magnetic field near which the "elbow" in the density measurements occur. In other words, B_0^* represents the critical magnetic field observed by Ahedo and Navarro-Cavallé [17], which suggests that the transition from a low-confinement regime to a high-confinement regime occurs as the magnetic field increases to the point when $Pe_{\rm an} \sim 1$ in the injection region.

A simple scaling relation between η_m and $Pe_{\rm an}$ emerges from the theoretical model that we derived in Sec. 2.1 if we consider the limit $\Lambda \gg 1$, $\Psi \ll 1$, and $\Lambda \Psi \sim 1$, which is valid over most operating conditions of our PS. In this limit, Eq. (2.10) then becomes

$$\eta_m \approx \left(\frac{1 + \eta_{m,0} \Pi}{1 + \Pi} \right) e^{-b/Pe_{\rm an}}. \tag{4.5}$$

Again, the exponential dependence on $Pe_{\rm an}$ emphasizes the importance of proper plasma confinement in the PS. Indeed, it is clear that $\eta_m \to 0$ for $Pe_{\rm an} \ll 1$. For $Pe_{\rm an} \gg 1$, however, the plasma is well confined and $\eta_m \to \eta_{\rm hc}$, where $\eta_{\rm hc}$ is the mass

utilization efficiency at high-confinement. We note that η_{hc} depends on both the efficiency of the ionization region, $\eta_{m,0}$, and balance between ionization and charge exchange collisions, Π.

We can examine the scaling of η_m with Pe_{an}^i from our experimental data by estimating the mass utilization efficiency as $\eta_m \approx \bar{n}_a m_i A_{\mathrm{eff}} c_s / \dot{m}$, where A_{eff} is the effective cross-sectional area that results from integrating the density profile of Eq. (4.1) over the cross-sectional area of the throat plane. We have assumed the ions remain singly charged and satisfy the sonic condition at the MN throat [1].

We show in Fig. 4.5 the experimentally estimated mass utilization efficiency, η_m, versus the anisotropic Péclet number calculated at the injection plane, Pe_{an}^i. Data is shown for the four backplate locations that correspond to the LP data in Figs. 4.3 and 4.4. Also shown is a solid line that represent the scaling of η_m with Pe_{an} that we derived in Eq. (4.5). The data clearly shows the transition between a low-confinement
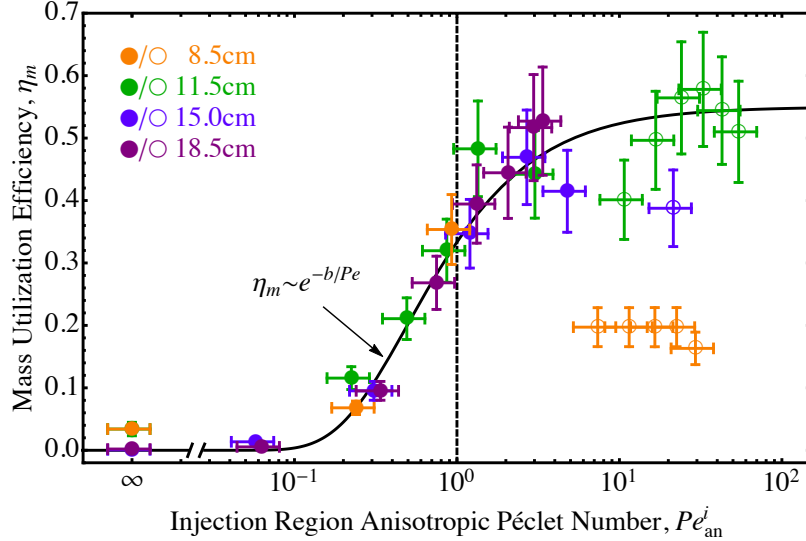
Figure 4.5: Scaling of the estimated mass utilization efficiency, η_m, with the injection region anisotropic Péclet number, Pe_{an}^i, for $P_D = 500$ W and $\dot{m} = 2$ mg/s. The solid and open data points correspond to the W and H modes, respectively. The solid black line represents Eq. (4.5) with $\eta_{\mathrm{hc}} = 0.55$ and $b = 0.5$ chosen for the best fit. The transition between diffusive and advective modes is marked with a dashed line at $Pe_{\mathrm{an}}^i = 1$.

99

and high-confinement mode near $Pe_{\mathrm{an}}^i = 1$ (dashed, vertical line). Furthermore, the scaling law derived in Eq. (4.5) appropriately describes this transition.

The mass utilization efficiency measured in the high-confinement limit, $\eta_{\mathrm{hc}} \approx 0.55$, implies that $\eta_{m,0} \approx 0.35$, which is consistent with the ionization percentage in helicon plasmas [44, 81, 82]. Here, we have used $T_e \approx 5$ eV to calculate $\Pi \approx 1.2$ using the equations in Sec. 2.3. Measurements at different mass flow rates and powers indicate that η_{hc} increases with P and inversely with $\dot{m}$. For example, we measured $\eta_{\mathrm{hc}} \approx 0.75$ for $\dot{m} = 2$ mg/s and $P = 700$ W, and $\eta_{\mathrm{hc}} \approx 0.85$ for $\dot{m} = 1$ mg/s and $P = 700$ W. This suggests that the operational regime studied in this paper ($\dot{m} = 2$ mg/s and $P = 500$ W) is power-limited near the ionization region of the antenna. In other words, $\eta_{m,0}$ increases as P increases. Additionally, the inverse relationship between T_e and $\dot{m}$ lowers the value of Π, thus increasing η_{hc}. Thus, while the data in Fig. 4.5 indicate a relatively low η_{hc}, the ability to increase η_{hc} by varying $\dot{m}$ and P is encouraging from a propulsion standpoint.

Finally, we note that the H mode data does not match the predicted scaling as well as the W mode data due to the decrease in density that occurs during the W-H mode transition, which is especially true for the case of $L_{\mathrm{bp}} = 8.5$ cm. We suspect that this is the result of diminished power coupling between the antenna and plasma as evidenced by the impedance mismatch observed during this transition. The scaling for the H mode may be recovered by introducing a different value for $\eta_{m,0}$ that is less than that of the W mode, which is consistent with the lower ionization fractions observed for H mode plasmas [46].

4.4   Chapter summary

In this chapter, we have used visible photography and RF-LP measurements to characterize plasma transport in the channel of an HPT while varying the length of the

channel and the applied magnetic field strength. A number of conclusions can be drawn from these measurements:

- Plasma formed in the injection region of the PS advects along the applied magnetic field towards the MN throat. Electron-ion collisions create a diffusive region surrounding the advective core. A critical magnetic field exists above which advection from the MN dominates diffusion to the channel walls.

- The length of the channel influences the flow in two ways: (1) the magnetic field topology becomes more pinched, resulting in a plasma density profile with a concentration towards the thruster centerline, and (2) the critical magnetic field increases because more wall area exists.

- In agreement with the analytical model that we derived in Sec. 2.1, the mass utilization efficiency scales with the anisotropic Péclet number calculated at the injection region, Pe^i_{an}. The critical magnetic field corresponds to $Pe^i_{\mathrm{an}} \sim 1$.

Chapter 5

Electron Thermodynamics

We saw in Chapter 2 that the final exhaust velocity, u_{ex}, of the ions in the far downstream region has a strong influence on both the specific impulse and thrust efficiency of a MN thruster. We estimated u_{ex} by assuming that the expansion followed a polytropic process. This assumption introduced a free parameter into our model in the form of the electron polytropic index, γ_e. Using analytical and experimental investigations, we address in this chapter the scaling of γ_e with the plasma parameters.

The thermodynamics of an expanding magnetized plasma play an important role in momentum and energy transfer in solar wind [133], astrophysical jet [134], and electric propulsion plasmas [12]. The mathematical complexity required to account for the energy transfer processes in the plasma fluid equation [135] renders most analytical models of magnetically expanding plasmas intractable. To make the equations more manageable, theoreticians often impose an *ad hoc* state equation between the plasma temperature and density. The prevailing state equation is that of a polytropic process, which assumes $p/n^\gamma = C(\psi)$. Here, p and n are the plasma pressure and density, respectively, and C is constant along a characteristic surface ψ (e.g. a magnetic flux surface). The value of the polytropic index, γ, determines the global behavior of

the expanding plasma. Two common examples for a monatomic gas are isothermal $(\gamma = 1)$ and adiabatic $(\gamma = 5/3)$ processes.

The polytropic index is important when modeling electric propulsion plasmas [76, 91, 92, 93]. This is especially true for those that rely on plasma acceleration through a magnetic nozzles (MN) [17] because momentum is primarily imparted to the thruster from the thermally expanding plasma propellant [32]. The commonly used assumption of isothermal expansion $(\gamma = 1)$, often justified by referencing the large field-aligned electron thermal conductivity, leads to an exhaust jet with an unbounded kinetic power [85]. In spite of this physical inconsistency, isothermal models are useful for studying the macroscopic dynamics [23] of the expanding plasma and the influence of the plasma and magnetic field topologies on the performance of MNs [95]. The relevant physical processes in the downstream region, however, are strongly influenced by the electron temperature. Therefore, MN performance and plasma detachment models would benefit greatly from improved understanding of electron cooling in magnetically expanding plasmas.

In this Chapter, we use a quasi-1D theoretical model to prove that electron cooling in a magnetically expanding weakly collisional plasma is well-approximated by a polytropic process (Sec. 5.2), and derive a limiting value of γ for regimes in which heat conduction dominates over heat convection. We show that this value is consistent with previous experimental measurements, and perform additional experiments on a MN plasma to show that the result of the theoretical model can be extended to the collisionless regime (Sec. 5.2). Our results are summarized in Sec. 5.3.

5.1   Quasi-1D expansion model

Investigating the electron thermal conductivity in a MN plasma, Litvinov [136] combined a quasi-1D expansion model with an energy equation that balanced heat con-

duction and convection. A dimensionless quantity was found, referred to as the adiabaticity parameter, that governed the transition away from an adiabatic flow. Assuming a polytropic process, Litvinov derived a minimum value of $\gamma_e \approx 1.19$ using a Taylor series expansion of the fluid equations about the MN throat. We loosely follow Litvinov's model with the following exceptions: (1) we solve for the exact solution to the quasi-1D fluid equations, (2) show that this solution is consistent with a polytropic process, (3) and consider expansion through a cross-section that more accurately represents the magnetic field topology of a MN.

Plasma acceleration through a MN [Fig. 5.1(a)] can be described using a quasi-1D fluid model [1]. Using the convention $y' \equiv dy/d\hat{z}$, the plasma continuity and momentum equations may be cast in normalized form as

$$(\hat{n}\hat{u}\hat{A})' = 0, \tag{5.1}$$

$$\hat{n}\hat{u}\hat{u}' = -(\hat{n}\hat{T}_e)', \tag{5.2}$$

where $\hat{n} \equiv n/n_0$, $\hat{u} \equiv u/\sqrt{T_{e,0}/m_i}$, $\hat{A} \equiv A/A_0$ and $\hat{T}_e \equiv T_e/T_{e,0}$ are the normalized plasma density, velocity, cross-sectional area, and electron temperature, respectively. With the exception of the velocity, each quantity is normalized by it's value at the MN throat. These equations describe ion acceleration along the magnetic field of an electron-driven magnetic nozzle (ED-MN), where expansion is driven by the thermal electrons ($T_e \gg T_i$), and the force of the electron pressure is communicated to the ions through the ambipolar potential, $\hat{\phi}' = (\hat{n}\hat{T}_e)'/\hat{n}$. The Lorentz force is omitted from the model because it primarily governs confinement of the plasma in the cross-field direction, and has little influence on the field-aligned expansion [23].

A closure relation for T_e is needed to solve Eqs. (5.1) and (5.2). We assume that the plasma is weakly-collisional, or $\tau_{ei} > \tau > \tau_e$. Here, τ_{ei}, τ, and τ_e are the timescales for electron-ion thermal equilibration, plasma expansion, and electron

104

collisions, respectively [135]. Neglecting also radiation losses, the energy equation takes the form

$$\left[\hat{n}\hat{u}\hat{A}\left(\frac{1}{2}\hat{u}^2 + \frac{5}{2}\hat{T}_e\right) + \frac{1}{\text{Nu}}\hat{q}_e\hat{A}\right]' = 0. \tag{5.3}$$

Here, $q_e = \kappa_e T_e'$ is the electron heat conduction with thermal conductivity, κ_e. We have defined $\text{Nu} \equiv n_0 T_{e,0}\sqrt{T_{e,0}/m_i}/q_{e,0}$ as the Nusselt number of the flow – a dimensionless parameter that compares the magnitude of convective to conductive heat transport. We note that Nu is equivalent to the adiabaticity parameter found by Litvinov.

Spitzer and Harm derived an expression for the electron thermal conductivity, κ_{SH}, in a collisional plasma [137]. Because $\kappa_{SH} \propto \tau_e$, the electron thermal conductivity increases as collisions become less frequent. It is generally accepted, however, that electron heat conduction is limited by the electron flux in collisionless plasmas [138]. A consensus does not exist in regards to the transition between these regimes, which has been predicted to occur when $\text{Kn}_e \sim 10^{-2} - 1$ [139]. Here, $\text{Kn}_e \equiv \lambda_e/L_{\nabla T_e}$ is the electron Knudsen number and $L_{\nabla T_e} \equiv T_e/|\nabla T_e|$ is the temperature gradient length scale. We will consider plasmas that satisfy $\text{Kn}_e \ll 1$, which implies $\text{Nu} \gg (m_e/m_i)^{1/2}$ using $\kappa_e = \kappa_{SH}$.

We consider first the limit in which electron heat conduction along the magnetic field dominates convection, or $\text{Nu} \ll 1$. The first term in Eq. (5.3) is negligible in this limit, and we can write $(\hat{q}_e\hat{A})' = 0$. Ignoring it's weak dependence on n and T_e (through the Coulomb logarithm), the electron thermal conductivity scales as $\kappa_{SH} \propto \hat{T}_e^{5/2}$. From this, we obtain the closure relation used in our model, $\hat{A}\hat{T}_e^{5/2}\hat{T}_e' = (\hat{T}_e')_0$. This equation indicates that electron cooling in the limit $\text{Nu} \ll 1$ depends primarily on the cross-sectional area of the expanding plasma.

We note that $(\hat{q}_e\hat{A})' = 0$ is the quasi-1D analogue of a solenoidal electron heat flux, or $\nabla\cdot\mathbf{q}_e = 0$. This form should not be confused with the adiabatic condition ($\mathbf{q}_e = 0$). Interestingly, the combination of a solenoidal heat flux and classical (Spitzer-Harm)

105

electron thermal conduction results in $\nabla^2(\hat{T}_e^{7/2}) = 0$. The quantity $\hat{T}_e^{7/2}$ represents an effective potential, which can be found using the proper boundary conditions.

The electron temperature gradient at the MN throat, $(\hat{T}_e')_0$, may be found with the requirement $\hat{T}_e \to 0$ as $\hat{z} \to \infty$, where $\hat{z}$ is the axial coordinate normalized by the magnet radius, r_c.. This yields, $(\hat{T}_e')_0 = -(2/7)\hat{k}_B^{-1}$, with $\hat{k}_B = \int_0^\infty \hat{A}^{-1}d\hat{z}$. Using the energy equation, we find the following analytical expression for $\hat{T}_e$:

$$\hat{T}_e = \left[1 - \hat{k}_B^{-1}\int_0^{\hat{z}} \hat{A}^{-1}d\hat{\zeta}\right]^{2/7}. \tag{5.4}$$

Here, $\hat{\zeta}$ is the dummy variable for integration over $\hat{z}$. Eq. (5.4) is similar in form to the predicted T_e-profile in the solar transition region [140].

We combine Eqs. (5.1)-(5.2) with the energy equation to find

$$\hat{A}\left(\hat{u}^2 - \hat{T}_e\right)\hat{u}' = \hat{u}\hat{T}_e\hat{A}' - \hat{u}\hat{T}_e^{-5/2}\hat{T}_e'. \tag{5.5}$$

The flow becomes choked when $\hat{A}' - \hat{T}_e^{-7/2}(\hat{T}_e')_0 = 0$. At this point, $\hat{u}^* = (\hat{T}^*)^{1/2}$, where the asterisk denotes values at the location of the singularity, $\hat{z}^*$. For a given $\hat{A}$, we obtain the numerical solution to (5.5) using Eq. (5.4) and the initial conditions, $\hat{T}(0) = 1$, $\hat{T}_e'(0) = (\hat{T}_e')_0$, and $\hat{u}(z^*) = \hat{u}^*$. Finally, the density and potential are found from the continuity equation and ion momentum equation, $\hat{n}\hat{u}\hat{A} = \hat{u}_0$ and $\hat{\phi} = (\hat{u}_0^2 - \hat{u}^2)/2$, respectively.

The applied magnetic field is well-approximated as a magnetic dipole. The cross-sectional area of the magnetically confined plasma then takes the form $\hat{A} = (1+\hat{z}^2)^{3/2}$. It immediately follows that $\hat{k}_B = 1$ and $(\hat{T}_e')_0 = -2/7$. Inserting these values into Eq. (5.4), we find the variation of $\hat{T}_e$ with $\hat{z}$ shown by the solid line in Fig. 5.1(b). It can be shown that the flow is choked at $\hat{z}^* = -2/\sqrt{525}$, with $\hat{u}^* = (25/23)^{1/7}$. The axial variation of $\hat{n}$, $\hat{u}$, and $\hat{\phi}$ obtained from Eq. (5.5) and the conservation equations is shown in Fig. 5.1(c)-(e). Here, $\hat{u}_0 \approx 1.12$ and $\hat{\phi}_0$ are the normalized velocity and
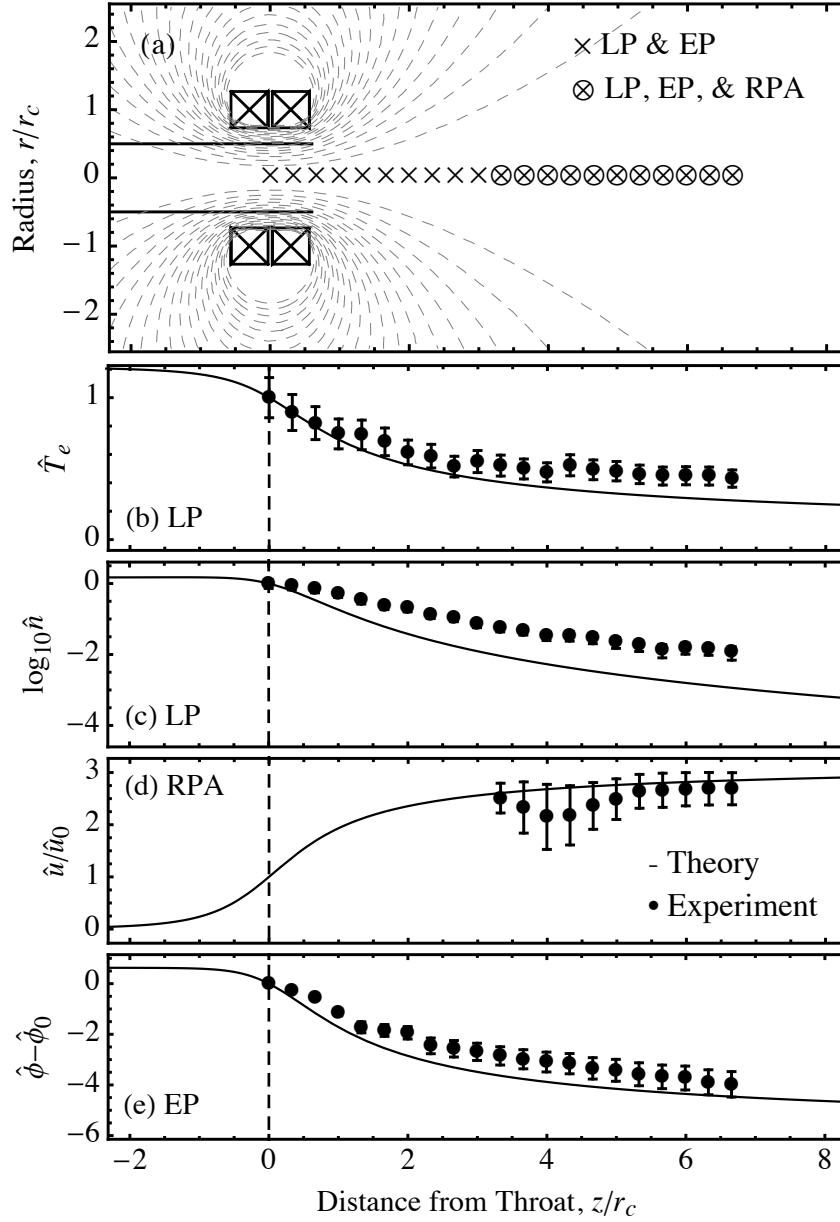
Figure 5.1: (a) Schematic showing the plasma source, MN field lines (dashed) and locations at which Langmuir probe (LP), emissive probe (EP), and retarding potential analyzer (RPA) measurements are taken. The panels contain the following measurements for $I_B = 17.5$ A: (b) electron temperature, (c) mean ion velocity ($\hat{u}_0 \approx 1.12$), (d) plasma density, and (e) plasma potential. Solid lines in (b)-(e) represent theoretical predictions, and the dashed lines indicate the location of the nozzle throat.
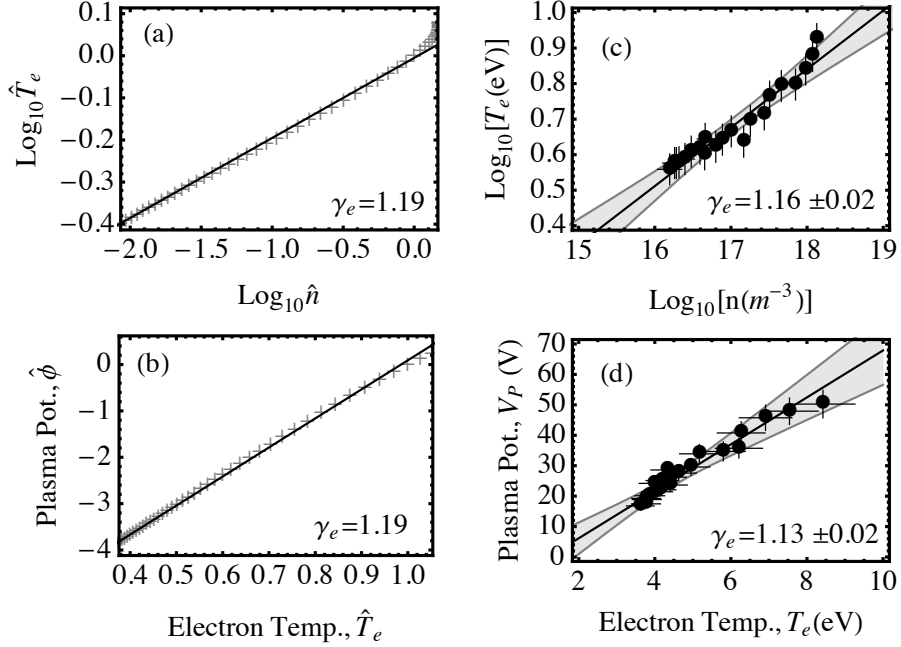
Figure 5.2: Comparison between the quasi-1D model (+) and polytropic scaling (line) for (a) $\log_{10} \hat{T}_e$ vs. $\log_{10} \hat{n}$, and (b) $\hat{\phi}$ vs. $\hat{T}_e$. Experimental measurements of the same quantities for $I_B = 17.5$ A are shown in (c) and (d) along with the line of best fit and 95% confidence interval.

potential at the MN throat, respectively. It is evident that the density decreases along with the electron temperature as the plasma expands through the diverging magnetic field. A supersonic ion beam forms downstream with an energy commensurate with the sum of the initial ion energy at the throat and the energy acquired through the ambipolar potential drop. This potential drop forms in the wake of the expanding electrons to maintain quasinuetrailty in the exhaust, and is known to be the primary source of ion acceleration in ED-MNs [24].

We now address the question: can plasma expansion in a MN be describe in terms of a polytropic process? If so, what is the effective polytropic index that best describes this expansion? The definition of a polytropic process predicts that the electron temperature and density are related through $d(\ln \hat{T}_e)/d(\ln \hat{n}) = \gamma_e - 1$. Additionally, inserting the polytropic equation into the electron momentum equation and neglecting inertial terms yields $d\hat{\phi}/d\hat{T}_e = \gamma_e/(\gamma_e - 1)$. For a polytropic process,

the slope of the curves for $\ln \hat{T}_e$ vs. $\ln \hat{n}$ and $\hat{\phi}$ vs. $\hat{T}_e$ should be constant. Using the solution to the quasi-1D model, we show in Fig. 5.2(a) and (b) that this is predicted to be the case in the region downstream from the MN throat for Nu $\ll 1$.

We derive analytically the polytropic index by noting that the $\lim_{\hat{z}\to\infty} \hat{u}' = 0$. In this limit, substitution of the continuity and polytropic equations into the energy equation provides $\gamma_e = 1 - (\hat{T}_e')_0/\hat{\alpha}$, where $\hat{\alpha} = \lim_{\hat{z}\to\infty}(\hat{A}'\hat{T}_e^{7/2})$. Eq. (5.4) and the equation for $\hat{A}$ can be used to show that $\hat{\alpha} = 3/2$, from which we find $\gamma_e = 25/21 \approx 1.19$ to be in agreement with Litvinov's approximation [136]. The lines of constant slope in Figs. 5.2(a) and (b) correspond to $\gamma_e = 1.19$. Here, we find extraordinary agreement between the polytropic scaling and the quasi-1D model for $\hat{z} > 0$.

We extend our theoretical model to include the full version of Eq. (5.3) to examine the influence of Nu on γ_e. The solid line in Fig. 5.3, constructed using cubic spline interpolation of sixteen numerical solutions of the quasi-1D model, illustrates the
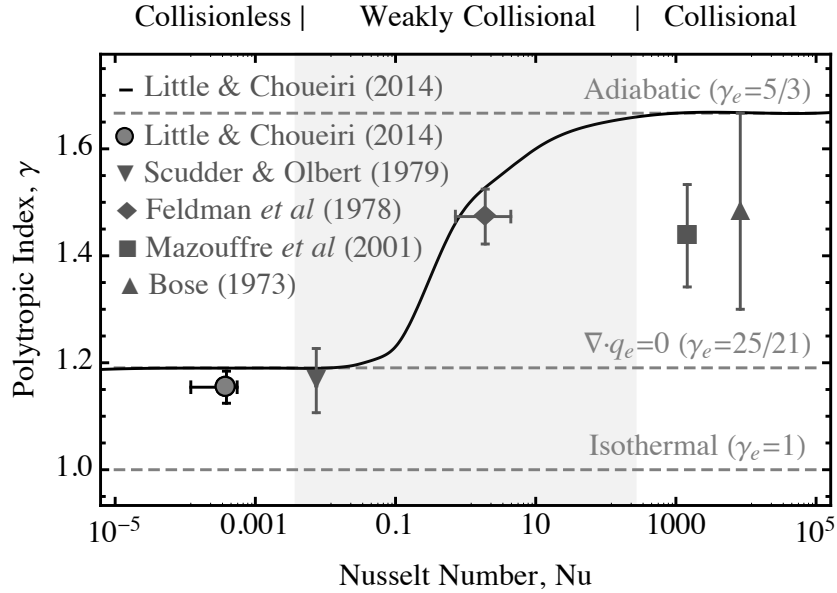

Figure 5.3: Predicted scaling of the polytropic index, γ, with the plasma Nusselt number, Nu. Dashed lines show relevant values of γ_e. Data point indicate experimental estimates obtained from the literature. The shaded region shows the weakly collisional regime for Argon plasmas.

predicted relationship between γ_e and Nu. We also show experimentally obtained values of γ_e found in the literature for different types of thermally expanding plasmas, including arc-heated electric propulsion [141, 142] and solar wind plasmas [133, 143]. We see from the theoretical curve that, contrary to the isothermal assumption ($\gamma_e = 1$) commonly used for Nu $\ll$ 1, the asymptotic value $\gamma_e = 25/21$ is quickly approached for Nu $<$ 0.1. Near Nu $\sim$ 1, a transition from solenoidal to adiabatic expansion occurs. Finally, as expected, $\gamma_e \to 5/3$ for Nu $\gg$ 1. The discrepancy between theory and experiment for Nu $\gg$ 1 is due to physical phenomena that are not taken into account in Eq. (5.3), and are important in high-density, highly collisional plasmas. Specifically, excitation, ionization, and recombination processes can create additional degrees of freedom in the plasma [144] – thus decreasing γ_e.

5.2   Experimental validation

MN plasmas for electric propulsion typically operate in a collisionless regime where $\mathrm{Kn}_e \gtrsim 1$, thus limiting the applicability of the Spitzer-Harm model for electron thermal conduction [138]. It is reasonable to ask the follow-up question: can plasma expansion in a *collisionless* MN plasma be described in terms of a polytropic process? We now turn towards an experimental investigation to answer this question and determine how the measured polytropic index compares to the theory for weakly collisional plasmas.

Measurements were taken in the downstream region of the Magnetic Nozzle Plasma Dynamics and Detachment Experiment (MN-PD^{2}X) [73]. The plasma source (PS) consists of a 7.5 cm inner diameter, 30.5-cm-long tube of borosilicate glass mounted concentrically inside two electromagnetic coils with a mean radius of $r_c = 7.51$ cm. Argon gas is injected through the center of a Macor backplate located 18.5 cm upstream from the center of the magnets. A two-turn spiral antenna

positioned next to the backplate is used to excite the plasma using 13.56 MHz RF radiation. The power delivered to the antenna was fixed at 500 W for the present study. The assembly is mounted inside a fiberglass vacuum chamber with an 8 ft. diameter and 25 ft. length. The measurements reported here were taken for an Argon mass flow rate of 0.5 mg $\cdot$ s^{-1}. At this flow rate, the steady-state pressure of the facility was measured to be around 20 μTorr. The MN is formed by passing DC current through the electromagnets. The strength of the peak magnetic field, B_0, is controlled with the applied current, I_B, such that $B_0[\text{G}] \approx 21 I_B[\text{A}]$. Langmuir probe measurements of the density and electron temperature within the PS suggest that we were operating in a low-field helicon mode [124] throughout this study. Typical plasma parameters associated with this mode for our experiment are $n \sim 10^{18}$ cm^{-3} and $T_e \sim 7$ eV. We note that $T_e \gg T_i$ for this type of plasma source, and expect thermal expansion to be driven by the electrons [24].

We characterized the expanding plasma using three diagnostics. A swept RF-compensated Langmuir probe (LP) [108] measured the plasma density, n, and electron temperature, T_e. The plasma potential, V_p, was obtained with a heated emissive probe (EP) using the floating point method [115]. We determined the mean velocity of the ion beam, u, from the ion energy distribution function (IEDF) measured with a four-grid retarding potential analyzer (RPA) [120]. The probe positions were controlled using a translation stage. For the LP and EP, we took measurements along the MN centerline ($r = 0$ cm) every 2.5 cm from $z = 0$ cm (throat) to $z = 50$ cm [see Fig. 5.1(a)]. Perturbations due to the size of the RPA restricted measurements of the ion velocity to $z \geq 25$ cm. This process was repeated six times for different $I_B \in [5, 20]$ A.

In Fig. 5.1 we show the axial variation of the measured plasma parameters normalized in accordance with the theoretical model. Immediately we see that Eq. (5.4), derived for a weakly collisional plasma, accurate predicts the decrease of $\hat{T}_e$ with $\hat{z}$ in

our collisionless plume [Fig. 5.1(b)]. The measured ambipolar potential drop and ion beam velocity also agree with the theoretical prediction [Figs. 5.1(d)-(e)]. We see a discrepancy between the measured and predicted rate at which the density decreases in the plume [Figs. 5.1(c)]. Two effects external to the theoretical model conspire to produce this discrepancy: the actual magnetic field falls off slower than a dipole magnet near the throat of the MN [73], and ion cross-field motion produces a plume that is more focused towards the MN centerline [23].

We calculate γ_e using linear regression of the $\log_{10} T_e$ vs. $\log_{10} n$ and V_p vs. T_e datasets. Typical datasets are shown in Figs. 5.2(c) and (d) along with the lines of best-fit and 95% confidence intervals. A clear linear relationship is observed in each dataset, with the calculated γ_e agreeing between the two independent methods within their experimental uncertainties. Furthermore, in accordance with the theoretical model, as we approach the MN throat we find a slight upward and downward deflection from linearity of the $\ln \hat{T}_e$ vs. $\ln \hat{n}$ and $\hat{\phi}$ vs. $\hat{T}_e$ data, respectively. We also observed γ_e to be relatively unaffected by I_B, with a weighted mean among all measurements of $\gamma_e = 1.15 \pm 0.03$. Therefore, although our plume is collisionless in the classical sense, the polytropic index corresponds surprisingly well with the predicted value for a weakly collisional plasma (Fig. 5.3).

Finally, we return to Eq. (5.3) to determine if the flux-limited (FL) model [138] for electron heat conduction in a collisionless plasma also yields polytropic expansion. FL electron heat conduction can take the form $1/q_e = 1/q_{\mathrm{SH}} + 1/q_{\mathrm{FL}}$ [145], where q_{SH} is the classical heat conduction, and $q_{\mathrm{FL}} \equiv bnm_e v_{t,e}^3$ is the FL electron heat flux where b is a constant of order unity. Numerically solving Eq. (5.3), we observed a number of inconsistencies between the FL model and our experimental measurements: (1) the expansion is no longer polytropic as q_{FL} becomes the same order of q_{SH}, (2) $\hat{T}_e$ increases with $\hat{z}$ as $q_e \rightarrow q_{\mathrm{FL}}$, and (3) $\hat{u}_e$ grows without bound as $q_e \rightarrow q_{\mathrm{FL}}$. Thus, we find that our experimental observations cannot be explained using the FL

model for electron heat conduction, which may imply an anomalous source of electron collisions is present in our plasma. The apparent validity of classical heat conduction in collisionless plasmas has been observed in the solar transition region [140] and tokamak scrape-off layers [139].

5.3 Chapter summary

In summary, we have shown that electron cooling in a magnetically expanding weakly collisional plasma may be described using a polytropic law when the energy balance in the plasma is governed by field-aligned heat convection and conduction. This finding is significant because it suggests that theoretical and computational models of plasma expansion may be simplified by replacing the energy equation with a polytropic equation, where the polytropic index depends largely on the Nusselt number of the flow. We derived analytically $\gamma_e = 25/21$ in the limit when heat conduction dominates over convection, and use experimental measurements to argue that this result extends into the collisionless regime.

Chapter 6

Plume Divergence

Our focus in this chapter is on the scaling of the MN exhaust plume divergence with the applied magnetic field strength. As we saw in Chapter 2, plume divergence can significantly degrade the performance of electric propulsion devices that employ MNs. This is apparent in the experimental study of an HPT by Shabshelowitz and Gallimore [60], who measure a beam divergence half angle in excess of 45°, from which they find greater than 50% of the power in the exhaust beam is lost to radial expansion. For comparison, the divergence angle is around 10–20° for a gridded ion thruster [87, 146] and 20–30° for a Hall thruster [87, 147].

Crucial to improving the divergence losses of a MN thruster is an understanding of the fundamental processes by which plasma expands through, and detaches from, a diverging magnetic field. With the intent of experimentally contributing to this understanding, the goal of this chapter is threefold: (1) determine the influence of the applied magnetic field strength and radial plasma profile on the divergence of the exhaust plume, (2) characterize the exhaust plume structure, and (3) examine the role of plasma demagnetization in the detachment process.

Our efforts in this chapter proceed in the following manner. We use Faraday probe measurements in Sec. 6.1 to show that there exists a transition between an

under-collimated plume and a collimated plume that is governed by the strength of the applied magnetic field. Repeating the measurements for various channel lengths, we are able to compare the predictions of the MN theoretical model derived in Chapter 2 with the observed behavior. In Sec. 6.1, we use a detailed mapping of the exhaust plume structure to show that the collimation transition coincides with the disappearance of an electric potential well at the free-jet boundary of the plasma. Finally, we present evidence in Sec. 6.3 that the collimation transition is driven by plasma demagnetization due to finite electron Larmor radius effects. The results of this chapter are summarized in Sec. 6.4

6.1 Plume divergence and ion dynamics

Fundamental to the divergence of the MN exhaust is the issue of ion separation, or detachment, from the applied magnetic field [8, 98, 148, 90]. Cox *et al.* [148] and Deline *et al.* [98] observed that the half-width at half-maximum of the radial density profile diverges less than the magnetic field, from which they conclude that ions have begun to detach from the MN. A similar conclusion was reached by Terasaka *et al.* [90] using Mach probes to spatially map the three-dimensional ion velocity vector. Direct measurements of ion detachment were made using Faraday probe sweeps by Olsen *et al.* [8]. In contrast to the previous studies, Olsen *et al.* observe the ion streamlines to detach *outward* with respect to the diverging magnetic field. Using a second stage to energize the ion population in addition to the electron population, they find that the ion beam detaches *inward*: a phonomenon they attribute to anomalous electron cross-field transport driven by the increased ion momentum.

Many of these experiments were performed at fixed or limited operational parameters. Notably absent from the literature is an experimental campaign addressing the influence of the applied magnetic field strength and radial plasma profile on the

ion dynamics and plume divergence of a MN plasma. The design of our experiment puts us in the unique position to characterize the effect of both of these quantities. Constructed using electromagnetic coils, we can operate our MN within a wide range of fields strengths by varying the current in the magnets (Fig. 3.2). Furthermore, we saw in Chapter 4 that we can control the radial plasma profile entering the MN throat by adjusting the length of the plasma source channel (Fig. 4.4). Therefore, the central goal of this section is to answer the question: *How do the magnetic field strength and radial plasma profile influence ion beam collimation in a MN exhaust?*

6.1.1 Ion streamlines

The performance of a MN depends strongly on the divergence of the exhaust beam, with a collimated beam required to minimize divergence losses. The beam divergence is intimately related to the ion dynamics in the plume because the ions carry most of the momentum by virtue of their large mass compared to the electron mass. Here, we characterize the influence of the applied magnetic field strength on the ion dynamics by measuring the ion streamlines at different plume locations.

Following the method of Olsen *et al.* [8], we can estimate the location of the ion streamlines by measuring the ion current density profile using the swept Faraday probe [see Fig. 3.9(c)]. The streamlines may be found numerically by solving for the location, $\theta_{ts} = \theta_\chi$, at which the area integral of the current density is a certain fraction, χ, of the total current, or

$$\chi = \int_0^{\theta_\chi} j_i \sin\theta_{ts} d\theta_{ts} \Big/ \int_0^{\theta_{max}} j_i \sin\theta_{ts} d\theta_{ts}. \tag{6.1}$$

Here, j_i is the ion current density measured using the Faraday probe, θ_{ts} is the angle that the translation stage makes with the MN centerline and $\theta_{max} = 95°$ is the maximum angle allowed by the translation stage for our system. We note that

the $\sin\theta_{ts}$ comes from converting the area integral in cylindrical coordinates to the translation stage coordinates.

The locations of the ion streamlines for different magnet currents are shown in Figs. 6.1(a)-(f) along with the magnetic flux surfaces (dashed lines) of the nozzle. Data was obtained using the LN$_2$ baffles, with $L_{bp} = 18.5$ cm, $P = 500$ W, and $\dot{m} = 0.5$ mg/s argon. Each figure contains three different data sets that represent the streamlines containing 30%, 60%, and 90% of the total ion current. Note that the error bar is indicative of the signal-to-noise ratio for each measurement. The signal-to-noise ratio scales with the density of the plasma, which is generally lower towards the plasma periphery and for small I_B (recall Sec. 4.2).

We immediately notice that the ion streamlines become more collimated as the applied magnetic field strength increases. Qualitatively, the streamlines for $I_B = 5.0$ diverge faster than the magnetic field lines, while the streamline and field line divergence for $I_B = 7.5$ A is comparable. As I_B increases beyond 10 A the streamlines become less divergent than the field lines. For $I_B \geq 15.0$, this is accompanied by significant cross-field motion of the ions and linearization of the streamline in the far-field. We note that linear streamlines in the far-field were observed by Olsen *et al.* [8], and have been used as a criteria for ion detachment from the MN.

6.1.2 Plume divergence scaling with B-field strength

Clearly a transition in the dynamics of the flow through the MN is occurring near $I_B = 5.0$ A. We define this transition in terms of the collimation of the plume, which we will quantify momentarily. Specifically, we will refer to flow that diverges *more* than the applied magnetic field as *under-collimated*. Alternatively, flow that diverges *less* than the magnetic field will be regarded as *collimated*.
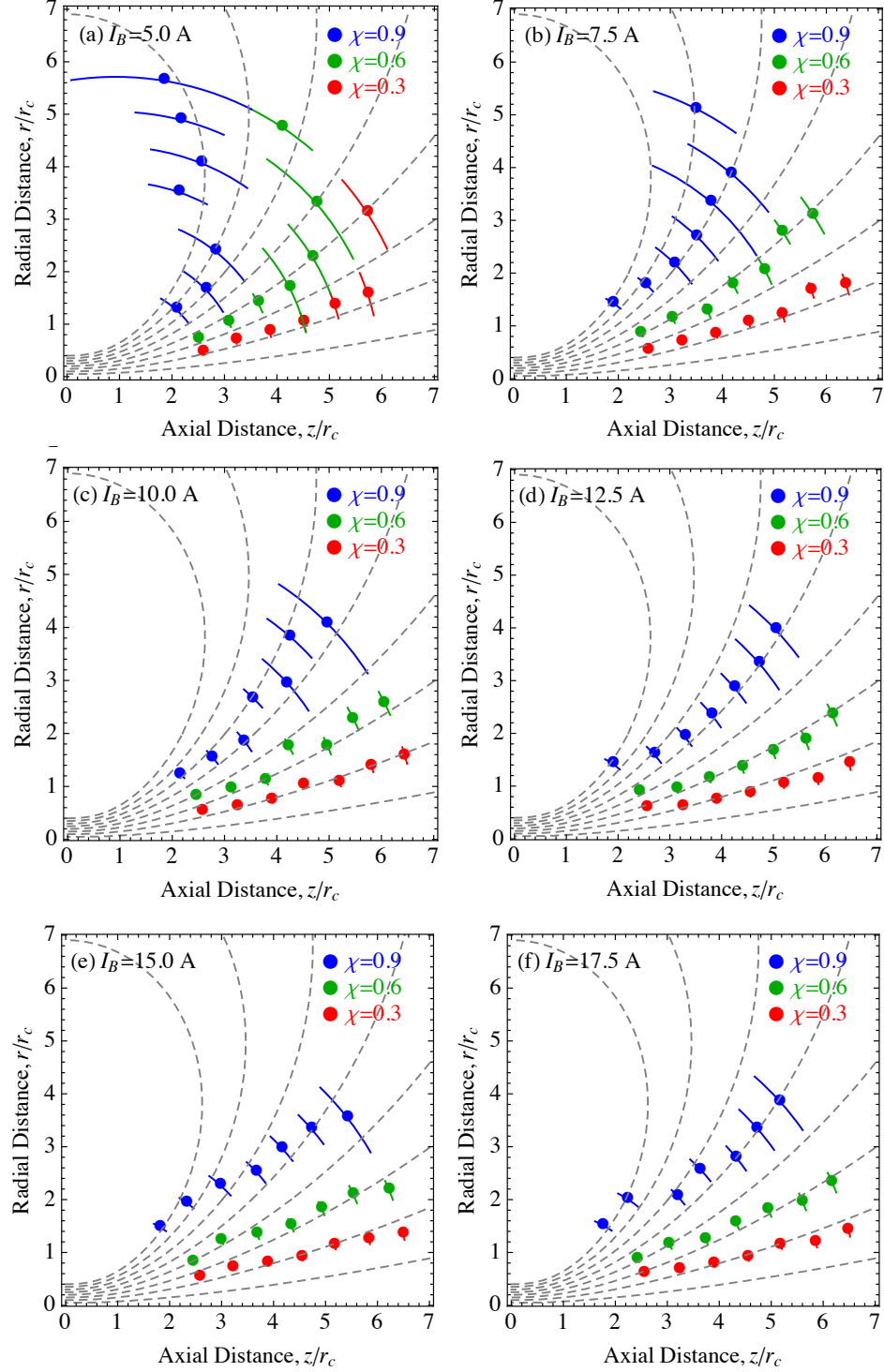
Figure 6.1: Location of the ion streamlines containing (red) 30%, (green) 60%, and (blue) 90% of the total ion current for various (a)-(f) applied field strengths. Dashed lines depict the magnetic flux surfaces, bounded by the magnetic flux surface that intersects the channel wall. Here, $L_{\mathrm{bp}} = 18.5$ cm, $P = 500$ W, and $\dot{m} = 0.5$ mg/s argon, and $p \approx 20$ μTorr

The plume divergence may be quantified using the divergence half-angle of the ion beam, θ_{div}, such that

$$\cos\theta_{\text{div}} = \int_0^{\theta_{\text{max}}} j_i \cos\theta_{\text{ts}} \sin\theta_{\text{ts}} d\theta_{\text{ts}} \Big/ \int_0^{\theta_{\text{max}}} j_i \sin\theta_{\text{ts}} d\theta_{\text{ts}}. \tag{6.2}$$

We calculate θ_{div} using the furthest downstream FP sweep, corresponding to a probe tip location 50 cm from the MN throat at $r = 0$.

Quantifying the magnetic field divergence is more obscure, however, because different magnetic field lines diverge at different rates. Furthermore, the ion current density is largest towards $r = 0$, which means that the plume divergence is weighted towards the MN centerline. To account for this, we calculate the magnetic field divergence, θ_B, as the *hypothetical* plume divergence if the ion current density profile remained constant (i.e. self-similar with respect to the surfaces of constant magnetic flux) throughout the plume, which would be true if the ion streamlines followed the magnetic field lines. We use RF-LP measurements to estimate the ion current density profile at the MN throat, j_0. We then substitute $j_i \rightarrow j_0 \cos(\Delta\theta_{\text{p}})$ and $\theta_{\text{div}} \rightarrow \theta_B$ into Eq. (6.2) to solve for θ_B, where we have defined $\Delta\theta_{\text{p}}$ as the angle that the magnetic field vector makes with the probe.

The results of this quantification may be seen in Fig. 6.2 where we plot the divergence half-angle as a function of the magnet current. Here, we use the furthest downstream FP sweep to determine θ_{div}. The shaded region represents the range of θ_B-values calculated using the RF-LP measurements at the MN throat for the different I_B. In accordance with our qualitative analysis of Fig. 6.1, we observe a transition from an under-collimated flow to a collimated flow near $I_B = 5.0$ A. As I_B increases the flow becomes collimated and the beam diverges less than the magnetic field. Eventually, we observe the divergence half-angle to approach an asymptotic value much less that θ_B.
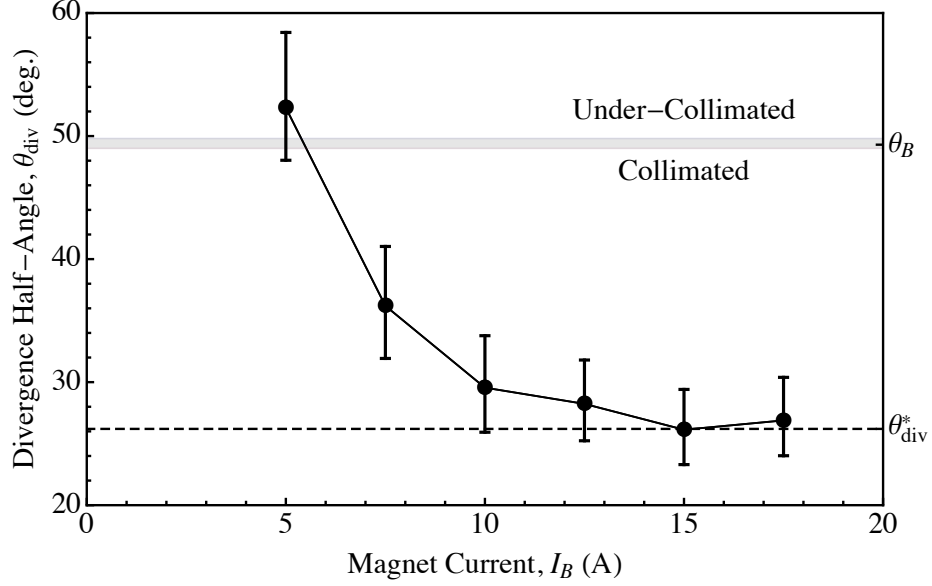
Figure 6.2: Exhaust plume divergence half-angle, θ_{div}, versus magnet current, I_B, demonstrating the transition from an under-collimated flow to a collimated flow. The grey region represents the range of values corresponding to the magnetic field divergence, θ_B, for different I_B. The dashed line represents the theoretical value of the divergence half-angle, θ^*_{div}. Measurements taken at $z_0 = 50$ cm.

We note that the plume divergence should increases at high magnetic fields due to the effect of the Lorentz force on the ion trajectories. The magnetic field strength at which the Lorentz force has an appreciable effect on the ion motion can be approximated by $B_0\,[\text{kG}] \approx 0.1\sqrt{\mu_i T_{\text{ev}}}$ [23], where μ_i is the ion atomic number. For our plasma ($\mu_i = 40$, $T_{\text{eV}} \approx 7$ eV), the required magnetic field is $B_0 \approx 1.7$ kG. The maximum operating magnetic field of our magnets is $B_{\text{max}} \approx 1.0$ kG. Furthermore, for the operating parameters focused on in this study, the helicon mode is only stable for $B_0 \leq 0.45$ kG [73]. We are therefore restricted in our experiments to operate under the threshold magnetic field at which ion magnetization becomes important.

6.1.3 Influence of the radial density profile

Using a theoretical model, Ahedo and Merino [23] observed that the divergence of the plume decreases as the plasma entering the MN throat becomes more concentrated

120

towards the axis. This dependance is due to the fact that the magnetic flux surfaces further from the axis diverge downstream at a greater rate than those close to the axis. The movable backplate in our experimental setup offers the unique ability to change the channel length between tests. We saw in Chapter 4 that, due to the nature of the converging magnetic field in the channel, the concentration of plasma towards the axis increases with the distance from the backplate to MN throat, L_{bp}. This capability allows us to perform the first experimental verification of the relationship between the plume divergence and radial density profile, and provides a means to validate the theoretical performance model derived in Sec. 2.2.

Both the transition between radial density profiles with the mass flow rate and the radial dependance of the electron temperature are characteristics that we observe in our plasma source and have not been predicted from theoretical models. The transition radial density profile transition likely results from a combination of enhanced collisionality brought about by the increased neutral density that accompanies higher mass flow rates, and neutral depletion at lower mass flow rates. The lower T_e towards the channel wall likely results from the magnetic field topology within our PS. Because the magnetic field contours are convergent within the channel, there is a region of plasma whose upstream magnetic flux surface intersects the channel wall as opposed to the backplate. The magnetic field restricts the cross-field electron heat conduction, thus plasma formed in this side region cannot thermalize with the bulk plasma.

Before proceeding, we need to develop a common metric for the density profile to compare the experimental and theoretical results. In Chapter 4 we measured a radial density profile that was uniform until a certain radius, beyond which the density fell off exponentially. Repeating these measurements at a lower mass flow rate, 0.5 mg/s as opposed to 2.0 mg/s, we observed both the radial density and electron temperature profiles to be Gaussian. Subsequent measurements with mass flow rates in-between

these values revealed a transition between the two profiles. This is in contrast to the theoretical results of Chapter 2, which were derived for a zeroth-order Bessel function with a scaling parameter governing the uniformity of the profile.

Given the differing profiles, it is convenient to define a metric for the concentration of plasma flux towards the axis of the MN at the throat plane. Therefore, we introduce the mean flux radius,

$$\bar{r}_f \equiv \int_0^{r_p} j_i r dA \bigg/ \int_0^{r_p} j_i dA, \tag{6.3}$$

which is calculated at the MN throat, or $z = 0$. Here, j_i is the ion current density, r_p plasma radius, and A is the cross sectional area. We see that $\bar{r}_f$ decreases as the flux of plasma becomes more concentrated towards $z = 0$. For a uniform plasma, $dj_i/dr = 0$, and $\bar{r}_f = 2r_p/3$.

We show in Fig. 6.3 the minimum divergence half-angle, measured from our experiment for four different values of L_{bp}, plotted against the mean flux radius normalized by the magnet radius, r_c. In accordance with the measurements presented in Chapter 4, $\bar{r}_f$ scaled inversely with L_{bp}. A clear dependence of θ_{div} on $\bar{r}_f$ is observed, with θ_{div} increasing by around 17° as $\bar{r}_f/r_c$ increases from ~ 0.15 to ~ 0.25. The dependence of the plume divergence on the radial plasma concentration is also apparent from the visual nature of the plume, which can be seen from the photographs of the operating experiment included in Fig. 6.3.

It is interesting to note that the divergence angle of $\theta_{\mathrm{div}} \approx 43°$ for large $\bar{r}_f$ nearly coincides with the experiments by Shabshelowitz and Gallimore [60], who find $\theta_{\mathrm{div}} \geq 45°$. Their plasma was formed in a glass tube that yields a ratio r_p/r_c similar to our experiment. The magnetic field in their channel was uniform – a limit towards which our experiment approaches for small L_{bp}. Although they did not measure the radial density profile at the throat, it seems that the large plume divergence measured in their experiment was primarily due to a large value of $\bar{r}_f/r_c$. These divergence losses may be remedied either by increasing the radius of their magnets, r_c, or decreasing

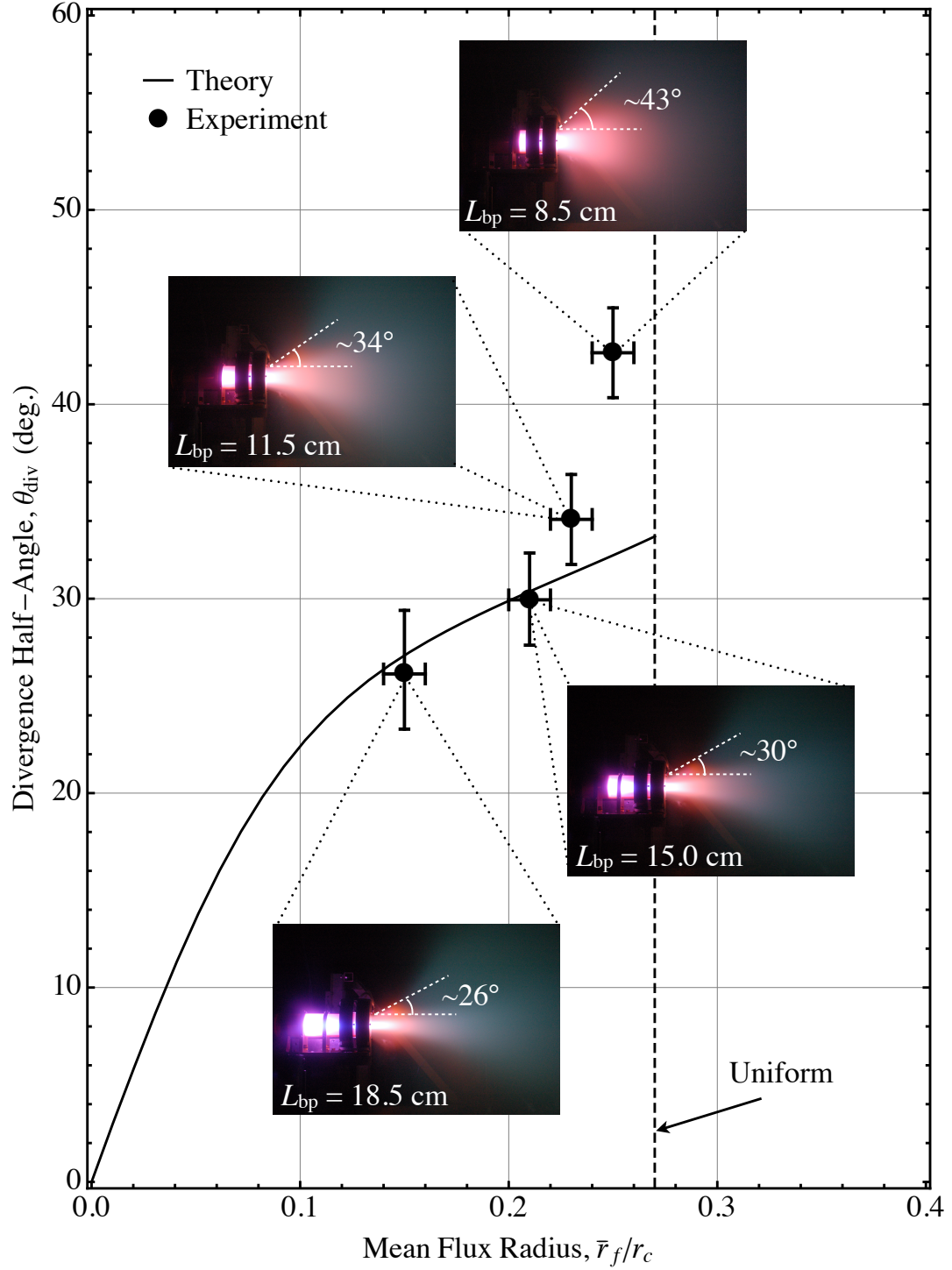Figure 6.3: Theoretical (solid line) and experimental (points) of the divergence half-angle, θ_{div}, on the mean flux radius calculated at the MN throat, $\bar{r}_f$. Photographs (f/7.1, 1/30 s exposure) show the experiment operating at the backplate location, Lbp corresponding to each data point. The dashed line represents the limit of $\bar{r}_f$ that corresponds to a radially uniform flow.

$\bar{r}_f$ through the use of a converging magnetic field prior to the MN. Indeed, using the latter method, we were able to obtain divergence angles of $\theta_{\mathrm{div}} \approx 26°$, which is comparable to the Hall thruster plume.

The solid line in Fig. 6.3 corresponds to the theoretically predicted divergence half-angle. We obtained this using the analytical solution derived in Sec. 2.2, and adding a polytropic equation of state to account for electron cooling in the expanding plasma [see Appendix B]. A Gaussian distribution was used for both the density and temperature profiles at the MN throat, $n = \exp\left(-r^2/\sigma_n^2/2\right)$ and $T_e = \exp\left(-r^2/\sigma_t^2/2\right)$, where σ_n and σ_t are the standard deviations of each profile. We used Eq. (2.64) to calculate θ_{div} from the relation $\cos\theta_{\mathrm{div}} \approx \eta_{\mathrm{div}}^{1/2}$. A value of $\gamma_e = 1.15$ was chosen to correspond to the experimental measurements in Chapter 5. For simplicity, we related the shape of the density and temperature profiles through the empirical relation, $\sigma_t \approx 1.3\sigma_n$, which was accurate to within a few percent for our experiment. Solutions were obtained for $\sigma_n \in [0, 3]$, which corresponds to $\bar{r}_f \in [0, 0.27]$. The upper bound of $\bar{r}_f$ represents a uniform flux profile, shown in Fig. 6.3 with a dashed line.

As expected from Sec. 2.2, the theoretically predicted divergence half-angle increases with the mean flux radius. For $L_{\mathrm{bp}} = 18.5$ cm and $L_{\mathrm{bp}} = 15.0$ cm, the predicted divergence agrees with the experiment to within the uncertainty of our measurements. As $\bar{r}_f$ is increased, however, the theory under predicts θ_{div}. Furthermore, the increase of θ_{div} with $\bar{r}_f$ is much greater for the experimental measurements that the theoretical prediction.

Two effects may be causing the discrepancy between theory and experiment at large $\bar{r}_f$. First, the approximation used in Eq. 2.55 is valid primarily for $\psi \ll 0.1$, corresponding to regions near the centerline. The density outside of this region remains small for low values of $\bar{r}_f$. However, the density outside this region becomes appreciable as $\bar{r}_f$ increases, forcing the theoretical solution to break down. Alternatively, the magnetic field strength could be playing a role in the large measured divergence

for $L_{\mathrm{bp}} = 8.5$ cm. The behavior of the operating modes, detailed in Sec. 3.5, limited experiments in this configuration to $I_B \leq 7.5$ A. According to Fig. 6.2, it is possible that we are not operating in the asymptotic regime for θ_{div} vs. I_B. If this is the case, the discrepancy may be due to phenomenon external to the theoretical model that become important at low I_B. With that said, Shabshelowitz and Gallimore [60] measured divergence angles greater than 45° for magnetic field strengths exceeding those of our experiment.

6.2   Exhaust structure and confinement

We observed in Sec. 6.1 that a transition occurs from an under-collimated to a collimated exhaust plume as the applied magnetic field strength increases above a certain value. Here, we use RF-LP and EP measurements to measure the transverse density and plasma potential profiles at various locations in the exhaust to gain insight on the physical mechanism behind the collimation transition.

6.2.1   Density and potential profiles

Density profiles are obtained from the ion saturation current, I_{sat}, of the RF-LP using a -27 V bias. An estimation for the electron temperature is required to determine the density from I_{sat}. For this, we use the polytropic law to relate the local electron temperature to the local density at the measurement location using measurements of the electron temperature and density at the MN throat, the value of γ_e determined from the axial RF-LP data (see Chapter 5), and the known magnetic field topology. This technique allows us to estimate the density anywhere in the plume.

A typical transverse density profile is shown in Fig. 6.4. The geometry associated with the measurement sweep is shown as an inset. Here, θ_{ts} is the angle that the translation stage makes with the centerline, and z_0 is the axial location of the probe
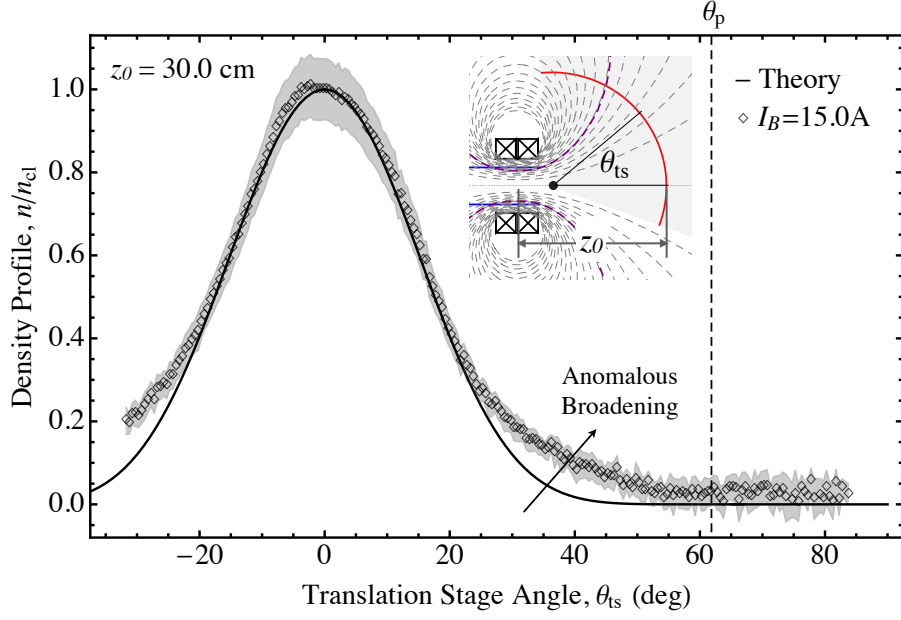
Figure 6.4: Normalized transverse plasma density profile for various magnet currents, I_B. The dashed line represents the predicted plasma-vacuum boundary, which coincides with the magnetic flux surface that intersects the glass tube at the plasma source exit.

tip at $\theta_{ts} = 0$. We normalize the density profile by the density at the MN centerline, n_{cl}. The shaded region represents the uncertainty in the measurement. We also show the theoretically predicted density profile obtained by inserting our measurements of γ_e and the n-and T_e-profiles at the MN throat into the model of Sec. 2.2 with the electron cooling correction in Appendix B. Finally, the dashed line marks the location of the predicted free jet boundary, θ_p, which coincides with the magnetic flux surface that intersects the glass tube at the channel exit.

The plasma density is clearly peaked towards the MN centerline and agrees remarkably well with the theoretical prediction in this region. The agreement with the model implies that the density profile is not self-similar such that it expands at a lower rate than the magnetic field. Self-similarity breaks down in the presence of ion cross-field motion – in accordance with the FP measurements in Fig. 6.1. A discrepancy between the predicted and observed density profile develops in the plume periphery

126

for $\theta_{ts} \geq 25°$. The plasma density in the periphery is far too low to attribute this discrepancy to classical diffusion. The γ_e-dependent correction for T_e produces some broadening of the density profile, however, it cannot account for the formation of the non-Gaussian region observed near the plasma periphery. It is therefore possible that the broadened profile results from some form of anomalous diffusion.

The plasma potential profile for the same conditions is shown in Fig. 6.5(a). The normalized plasma potential is given by $\phi = (V_p - V_{p,0})/T_{e,0}$, where $V_{p,0}$ and $T_{e,0}$ are the plasma potential and electron temperature at the MN throat, respectively. The potential profile is obtained by subtracting from the normalized potential its value at the MN centerline, ϕ_{cl}. Again, the dashed line in this figure coincides with the predicted plasma boundary.

We observe that the plasma potential is also peaked towards the MN centerline. This is due to the ambipolar electric field that forms to maintain quasineutrality at the plasma periphery [23], which is shown in Fig. 6.5(b). The most interesting feature, and one that is not predicted from existing theoretical models for MN plasma expansion, is the potential structure that forms in the vicinity of the free jet boundary. Here, we observe the formation of a potential well with strength Φ_w near θ_p. We demonstrate in Fig. 6.5(b) that the potential well coincides with a switch in the direction of the transverse electric field near the edge of the plasma.

Potential wells at the plasma edge are seemingly ubiquitous to magnetically confined plasmas [149, 150, 151]. In tokamak plasmas the electric field points inward from the bounding flux surface and is predicted to form as ions are lost from the device due to finite Larmor radius (FLR) effects [149]. A similar electric field forms near the plasma edge of reversed field pinch (RFP) plasmas [150]. The $E \times B$ velocity shear layer that results from this potential structure is an important aspect of these devices as it indicates the boundary of the plasma confinement zone [149] and can reduce turbulent transport through shear stabilization [152].
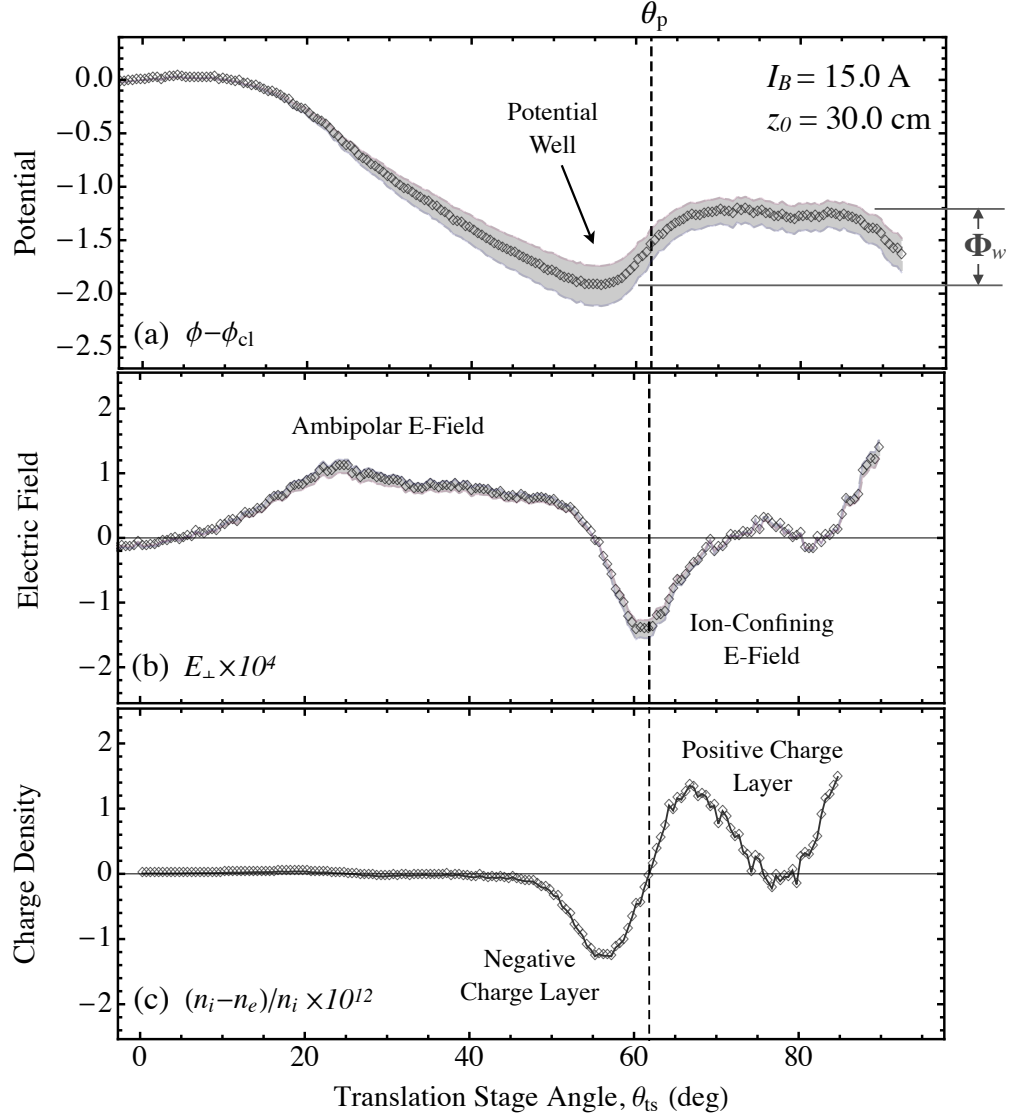
Figure 6.5: Normalized transverse (a) plasma potential, (b) electric field, and (c) charge density profiles in the exhaust. The dashed line represents the predicted plasma-vacuum boundary. A potential well is observed near the plasma periphery. The presence of this well forms a strong, ion-confining electric field at $\theta \approx \theta_p$, resulting from positive and negative charge layers in this region.

Wall losses due to FLR effects cannot explain the appearance of the potential well in our experiment because the plasma expands into a large vacuum chamber, thus avoiding interactions with the chamber walls. Rather, the potential well forms in response to finite transverse ion energies at the edge of the plasma [151]. The electrons remain magnetized far into the plume, and thus form a negative charge

cloud that is bound by the outermost flux surface. Ions with sufficient energy near the plasma periphery are able to overshoot the edge of the electron cloud, and create an excess of positive charge just beyond the boundary, with a comparable negative charge layer just within the boundary [153]. The charge density calculated from our probe sweeps is shown in Fig. 6.5(c).

The question may then be asked, *what is the source of the cross-field ion energy at the free-jet boundary?* This energy should scale with the strength of the potential well, Φ_w, which suggests values on the order of T_e measured at the throat. Recall, however, that $T_i \ll T_e$ for a helicon plasma [154], which suggests the initial thermal energy of the ions is insufficient to form the well. Additionally, the classical MN expansion model with $T_i = 0$ predicts that the ions do not acquire transverse energy at the plasma edge [23]. It is true that a potential well emerges from the model with the inclusion of $T_i \sim T_e$ [70]; however, the density in the downstream plasma is far too low for collisions to thermally equilibrate the electrons and ions. Therefore, an anomalous source of ion energy must be present near the edge of the downstream, expanding plasma. One such mechanism may be ion acoustic turbulence driven by strong density and temperature gradients [155]. IAT may also explain the broadening of the density profile in Fig. 6.4 as it has been linked with an enhanced plasma resistivity [156]. Indeed, we observe this broadening in a region predicted to have large azimuthal electron velocities [23], which could drive IAT. Alternatively, the well could result from the transition from a wall-bound to a magnetically-expanding flow. The near-wall region possesses a thin inertial layer that contains ions with significant cross-field velocities [88]. The potential well may then form if a portion of these ions are convected downstream.

Finally, we note that a similar potential structure was measured by Charles using a helicon plasma magnetically expanding into a grounded diffusion chamber [157], and studied in further depth by Saha *et al.* [158] for a similar system. In both of these

analyses the potential well coincided with a region of high plasma density. Thus, a hollow, conical plume emerged from their plasma source into the diffusion chamber. Observing this structure in PIC simulations, and noting its detriment for propulsion applications, Rao and Singh [159] argue that the potential structure needs to be considered when studying MN thrust generation. This is despite the fact that they find the potential well in their simulations to result from the interaction between the plasma and grounded diffusion chamber – an interaction that would not be present in space. From this we argue that the plume structure of these experiments differs from ours due to the presence of a grounded wall in the vicinity of the exhaust. A careful examination of this issue is required before extrapolating their results to magnetic plasma expansion into a true vacuum.

6.2.2 Loss of confinement

Whatever the mechanism is that energizes the peripheral ions, the potential well formed in their presence is of great interest to us because it gives us a metric to analyze the magnetic confinement of the exhaust plasma. Here, we use this metric to analyze in greater depth the transition from an under-collimated to a collimated plume. From this analysis, we develop a broad physical picture of plasma expansion through a MN.

We compare in Fig. 6.6(a) the potential profiles for $I_B = 5.0$ A and $I_B = 15.0$ A obtained from probe sweeps at $z_0 = 25$, 30, and 35 cm [shown in red in Fig. 6.6(b)]. We also show the $\chi = 0.9$ ion streamline for each value of I_B in Fig. 6.6(b), from which we recall the plume is under-collimated for $I_B = 5.0$ A and collimated for $I_B = 15.0$ A. A potential well exists for both cases at $z_0 = 25$ cm, with the location of the streamline agreeing to within experimental error. Further downstream at $z_0 = 30$ cm, the potential well for $I_B = 5$ A disappears, and the streamline begins to diverge faster than the applied magnetic field. At this location, the plume for $I_B = 5$ A is
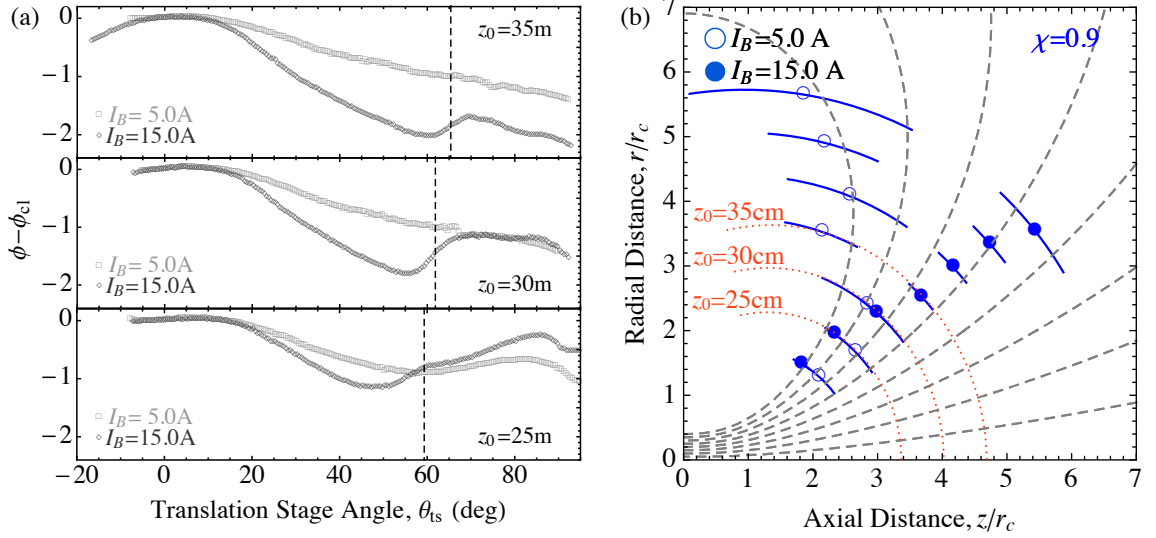
Figure 6.6: A comparison between the (a) plasma potential profiles and (b) ion streamlines for $I_B = 5.0$ A and 15.0 A. These figures demonstrate the increased plume divergence associated with the disappearance of the ion-confining potential well at the plasma edge.

no longer confined by the magnetic field. The breakdown of confinement is readily apparent from the large difference between the two streamlines at $z_0 = 35$ cm. In general, we see that Φ_w decreases with increasing z_0 due to the decreasing magnetic field strength. Eventually the potential well for $I_B = 15.0$ A also disappears, however, the rapid plume divergence observed for the under-collimated flow is not observed.

We see from Fig. 6.6(a) that the location of the potential well closely follows the location of the bounding magnetic flux surface, ψ_p. A closer inspection reveals the well to form just within ψ_p, with the location of the maximum inward electric field closely corresponding to ψ_p. This is demonstrated in Fig. 6.7 for six different magnetic field strengths. Here, the data points represent the location at which the inward electric field is greatest, and the solid lines correspond to ψ_p. The fact that fewer data points are shown for low values of I_B reflects the disappearance of the potential well at small z_0. We observe the furthest downstream location at which a
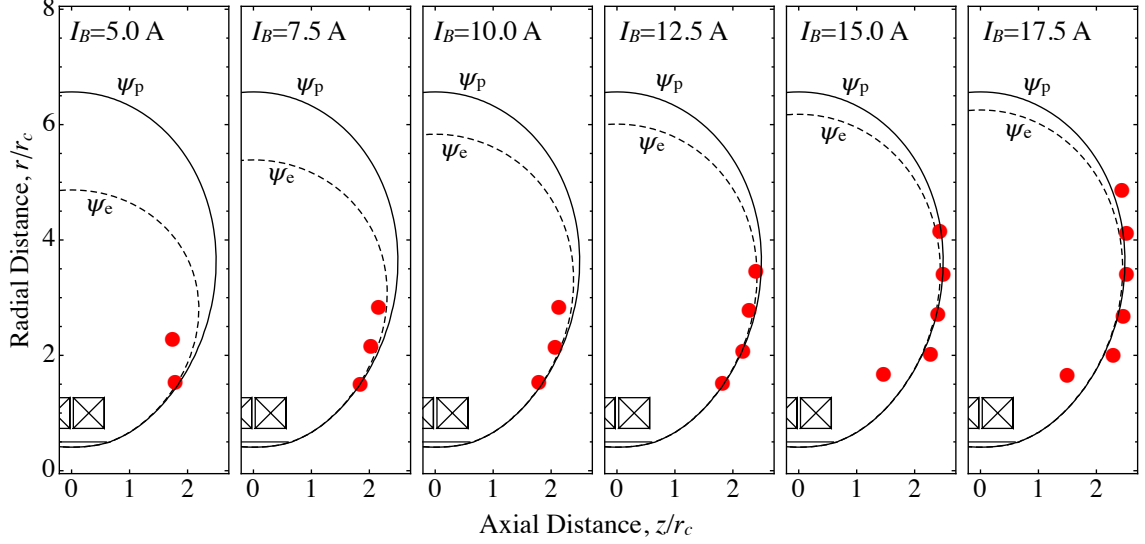
Figure 6.7: Measured location (red circles) of the maximum ion-confining electric field determined from the potential profile measurements. The bounding magnetic flux surface is labelled ψ_p. Also shown are the electric streamlines, ψ_e, that are predicted from the fluid model when electron inertia is included.

potential well exists increases with I_B. This suggests that the plasma is confined over a greater distance as the applied magnetic field strength increases.

The following physical picture emerges by combining our observations with the present understanding of MNs in the literature. A cloud of hot electrons expands through the diverging magnetic field, setting up an ambipolar potential drop through which the ions are accelerated [22, 24]. An outward component of the ambipolar electric field develops in the bulk of the plasma that radially deflects the ions to preserve quasineutrality [23]. In general, the strength of the ambipolar electric field is insufficient to force the ions to follow the curvature of the magnetic field lines, and the majority of ions separate inwards with respect to the diverging magnetic field to produce a collimated beam [9].

The electron cloud is confined by the applied magnetic field and remains within a volume defined by the bounding magnetic flux surface. Diamagnetic currents that result from this confinement transfer momentum from the expanding plasma to the

MN [31]. Effectively, the electron pressure is pushing against a magnetic wall formed by the nozzle [160]. Confinement eventually breaks down, corresponding to the end of the magnetic wall. This analogy can be visualized in Fig. 6.7 by imagining that the red data points trace the outline of a solid surface. Similar to an under-expanded nozzle, the residual thermal energy of the plasma at the point of lost confinement produces an additional outward expansion that depends on the Mach number of the flow. An under-collimated beam is one in which the residual electron thermal energy remains a significant portion of the ion beam kinetic energy when confinement is lost. In this case, the rapid expansion of the unconfined electrons causes the ion beam to diverge faster than the magnetic field. Unlike a conventional nozzle, confinement is lost gradually, and discrete shocks are not expected to form.

Throughout decades of research on the plasma physics of MNs, the question was commonly asked: *how does plasma detach from the applied magnetic field?* Inherent to this question is the assumption that the plasma is "stuck" to the magnetic field lines that must eventually close upon themselves. Therefore, a mechanism must exist for it to become "unstuck". This assumption obviously breaks down if confinement is lost downstream. Therefore, we argue that an equally relevant question is: *by what mechanism is confinement lost in a magnetic nozzle?* We end the chapter using experimental evidence to support of an existing theoretical model that may provide an answer to this fundamental question.

6.3 Evidence of electron demagnetization

Two theories presently exist that predict the outward expansion of a MN plasma following demagnetization. Both were analyzed by Ahedo and Merino as an extension of their 2D expansion model [23]. The first theory predicts that the magnetic field induced by the diamagnetic currents in the plasma becomes on the order of the

applied magnetic field in the downstream plume [7]. This effect is governed by the local value of β, defined as the ratio of the thermal energy density in the plasma to the energy density in the applied field. The induced magnetic field dominates the applied field as β approaches unity, leading to the expulsion of magnetic flux from the plasma and outward expansion. In the isothermal model of Ahedo and Merino, β increases downstream because the magnetic field decreases faster than the density. Implementing the polytropic law within their model, we find that the rate at which β grows downstream strongly depends on the rate of electron cooling in the plume. For the value of γ_e found in Chapter 5, β never exceeds unity for our plasma, thus plasma demagnetization through induced magnetic fields is not expected to be important.

The second theory was developed by Ahedo and Merino [69] in response to criticism that their 2D expansion model did not include the effects of electron inertia. Electron inertia was viewed as a key component of Hooper's [5] plasma detachment model, which predicted both the plasma ions and electrons to detach inward with respect to the magnetic field. Implementing the azimuthal component of the electron inertial force, Ahedo and Merino predict that electron finite Larmor radius (FLR) effects demagnetize the plasma and force outward separation with respect to the applied field. Physically, the model of Ahedo and Merino is more appropriate for MN plasmas because they include a finite electron temperature, whereas Hooper assumes both $T_i = 0$ and $T_e = 0$.

In regards to the question of plasma confinement in the MN exhaust, our experimental findings in Sec. 6.2 are compelling for two reasons: (1) they agree qualitatively with the notion that the plasma demagnetizes as the applied field strength decreases, and (2) they allow a direct comparison with theoretical predictions for how this process occurs fundamentally. Here, we provide a brief overview of the theory of electron demagnetization through FLR effects, and compare the disappearance of the potential well in our measurements with the location at which these effects become important.

6.3.1 Theory of electron demagnetization

Plasma demagnetization though electron FLR effects can be demonstrated by adding the electron azimuthal inertia term to the two-fluid equations [69, 70]. Before we proceed with this theory, we note that dimensionless units will be used throughout this section in accordance with the formalism of Sec. 2.2.2. Specifically, densities and electron temperatures will be normalized by their value at the center of the MN throat, n_0 and $T_{e,0}$, respectively. The electric potential, Φ, is normalized by the electron temperature, $T_{e,0}$, such that $\phi = e\Phi/kT_{e,0}$. Length scales are normalized by the magnet radius, r_c, the electron velocity is normalized by the electron thermal velocity, $v_{t,e} = \sqrt{k_b T_{e,0}/m_e}$, and the magnetic flux is normalized by $B_0 r_c^2$. Furthermore, $r_L \equiv m_e v_{t,e}/(e B_0 r_c)$ is the characteristic electron Larmor radius.

The polytropic law relates the density and electron temperature along a magnetic flux surface, ψ, through the equation

$$C(\psi) = \frac{T_e}{n^{\gamma_e-1}}. \tag{6.4}$$

Projecting the electron momentum equation along the magnetic field yields a generalized Bernoulli equation

$$H(\psi) = \phi - C(\psi)\frac{\gamma_e}{\gamma_e - 1}n^{\gamma_e-1}. \tag{6.5}$$

Finally, conservation of canonical angular momentum along an electron steamline requires

$$D_e(\psi_e) = r_L r u_{\theta e} - \psi, \tag{6.6}$$

where ψ_e is the electron streamfunction. Clearly, ψ is conserved along the electron streamlines in the limit of zero electron inertia ($r_L \to 0$). Simply put, the electron streamlines coincide with the magnetic field lines.

Each of the conserved quantities in Eqs. (6.4)-(6.6) may be found from the plasma parameters at the MN throat. The electron force balance in the direction perpendicular to the magnetic field produces an azimuthal velocity given by

$$u_{\theta e} = -r \left(H' + \frac{n^{\gamma_e - 1}}{\gamma_e - 1} C' \right), \tag{6.7}$$

which can also be viewed as the sum of the diamagnetic and $E \times B$ drift velocities [100]. Here, we have used the convention $H' = dH/d\psi$ and $C' = dC/d\psi$. In general, $u_{\theta e}$ grows with r along constant ψ_e. Therefore, ψ must increase above its value at the throat. In other words, the electron streamlines are deflected outwards from the magnetic field lines to offset the angular momentum that the electrons acquire to maintain force balance.

The equivalent of Eqs. (6.5)-(6.7) in the isothermal limit can be used to calculate the electron streamlines everywhere in the exhaust using only the density distribution at the MN throat [69]. The second term in Eq. (6.7) prevents this for $\gamma_e \neq 1$, however; this method is still viable in the downstream plasma periphery due to the smallness of n. We take advantage of this fact in Fig. 6.7 to calculate the outermost electron streamfunction for our experiment at each I_B. It is clear that ψ_e diverges from ψ_p, with the point of divergence occurring further downstream for larger I_B. Furthermore, there is a qualitative relationship between the point of divergence and the point at which the potential well disappears.

6.3.2   Confinement loss and electron demagnetization

We quantify the extent to which the outermost electron streamline is deflected from the bounding magnetic flux surface using the following parameter,

$$\epsilon_\psi \equiv \frac{\psi - \psi_p}{\psi_p}. \tag{6.8}$$

Here, ψ is evaluated along ψ_e. Effectively, ϵ_ψ represents the change in magnetic flux encompassed by ψ_e relative to the initial magnetic flux.

Using Eqs. (6.4)-(6.8), we define the normalized de-magnetization radius

$$r_d = \sqrt{\frac{1}{H'(\psi_p)} \left[\frac{\psi_p \epsilon_\psi}{r_L^2} - r_p u_{\theta e,t}(\psi_p) \right]}, \tag{6.9}$$

which describes the radius of the outermost electron streamline at the point where it has separated by the amount ϵ_ψ. In the limit where $u_{\theta e,t}(\psi_p) \ll \epsilon_\psi r_p/(2r_L^2)$, valid for our plasma, the demagnetization radius is given by

$$r_d \approx \frac{r_p}{r_L} \sqrt{\frac{\epsilon_\psi}{2H'(\psi_p)}}. \tag{6.10}$$

Here, we see here that the demagnetization radius scales inversely with the characteristic electron Larmor radius at the throat.

Assuming the plasma becomes demagnetized at a specific value of ϵ_ψ, Eq. (6.9) predicts the scaling of the demagnetization radius with the applied magnetic field strength (through r_L), plasma radius (through r_p and ψ_p), and radial temperature and density profiles at the throat (through H' and $u_{\theta e,t}$). We will use this scaling to determine if demagnetization via electron FLR effects can explain our experimental observations.

We begin by calculating r_d from our experimental data. We define the experimental value of r_d as the radius at which the ion confining potential well disappears. Because we limited our data sweeps to seven discrete values of z_0, we are only able to measure the potential well near ψ_p at seven different values of r. Therefore, we are only able to determine if the well disappears in between two discrete values of r. To improve upon this, we use the strength of the well, Φ_w, to estimate the value z_0 where the disappearance occurs. Specifically, we fit a line to the measurements of Φ_w
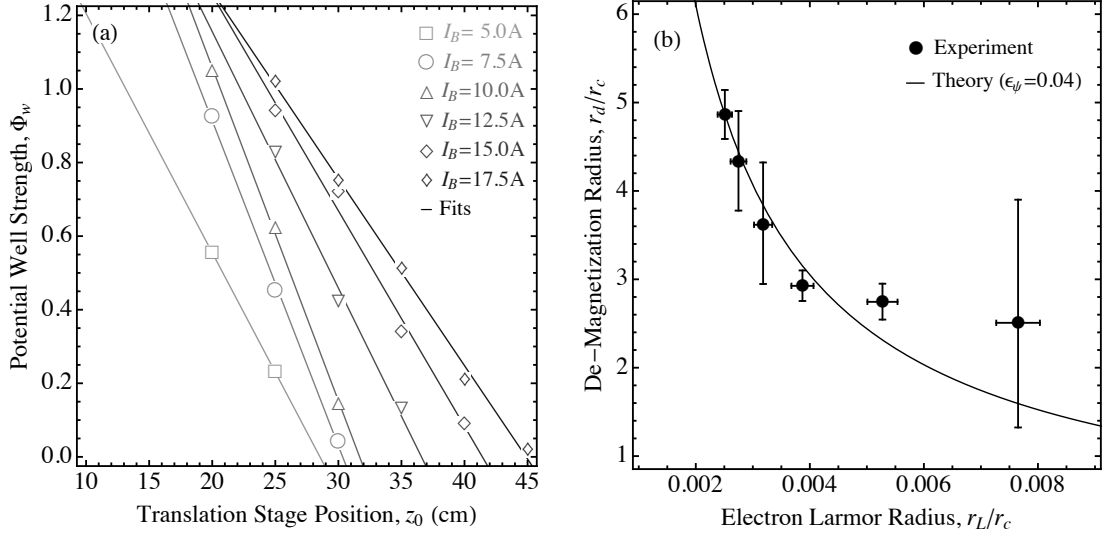
Figure 6.8: (a) Dependance of the potential well strength, Φ_w, on the translation stage position, z_0. (b) Experimental estimates of the normalized radius at which the plume becomes demagnetized, r_d/r_c. Also shown are theoretical predictions for r_d/r_c obtained by including electron inertia in the fluid model.

vs. z_0, and extrapolate this line to $\Phi_w = 0$. The value of z_0 corresponding to $\Phi_w = 0$ is then used to calculate r_d. This process is shown in Fig. 6.8(a).

We show in Fig. 6.8(b) the resulting values of r_d as a function of r_L, where r_L is calculated using RF-LP measurements of T_e at the throat, and increases with decreasing I_B. Also shown is the theoretical scaling $r_d \propto r_L^{-1}$, predicted from Eq. (6.10). Here, we chose $\epsilon_\psi = 0.04$ to produce the best fit to the data. We see that the theory and experiment agree to within the experimental uncertainty. This suggests that demagnetization via electron FLR effects may be the main culprit behind the loss of confinement in the MN exhaust. Furthermore, our data indicates that confinement is lost when the deviation of the electron streamlines from the magnetic field lines exceeds four percent.

We note that Fig. 6.7 depicts the electron streamline (ψ_e) to wrap around towards the plasma source. This seems to indicate that the plasma is not demagnetized, but instead bows outward with respect to ψ_p while remaining under the influence of the

138

applied field. The figure is misleading, however, because ψ_e is only calculated with the azimuthal component of the electron inertial force. In reality, other terms within the electron fluid model are important as FLR effects become of dominant order [69]. These terms, which include the viscosity tensor [161], render the fluid equations intractable for all but the simplest problems. Therefore there is no reason to suspect the electrons streamlines remain symmetric about $z = 0$, as suggested in Fig. 6.7, because the magnetic force is no longer dominant. Therefore, while the method of calculating ψ_e in the previous section is quantitatively useful for predicting the point along the free jet boundary where confinement is lost via electron demagnetization, its solution beyond this point should be viewed only as a qualitative indicator of the outward expansion of the plasma. Additional investigations using more detailed fluid models or full PIC simulations will likely be necessary to understand the self-consistent behavior of the plasma in this region and how it relates to the idea of magnetic nozzle plasma detachment.

Ion response to demagnetization

Finally, in light of the fact that confinement was lost for both the under-collimated and collimated plumes, it is reasonable to ask why rapid divergence of the ion streamlines was measured for one case but not the other.

The ability of the ions to separate either outwards or inwards with respect to the applied field in the presence of outward separating electrons was observed in the numerical simulations of Ahedo and Merino [69], and in the experiments by Olsen *et al.* [8]. It is possible to conclude from the analysis of Ahedo and Merino that the discrepancy is not due to ion magnetization because the case for which inward ion separation occurs corresponded to larger magnetic fields. Instead, the ion dynamics must be dictated by their susceptibility to the ambipolar electric field formed in the wake of the outward electron expansion.

Returning to the magnetic coordinate system described in Sec. 2.2, we can analyze the influence of the ambipolar electric field on the ion motion by recalling the force balance on the ions in the direction perpendicular to the magnetic field,

$$rB\frac{d\phi}{d\psi} = -\frac{u_i^2}{R_c} \tag{6.11}$$

Here, the left hand side represents the ambipolar electric force and the right hand side is the ion centrifugal force, both in normalized units. We will assume that the ions approximately follow the magnetic flux surfaces, letting R_c equal the local curvature radius of the magnetic field lines, and analyze the potential drop in the cross-field direction required to meet this assumption. If we recall $(rBR_c)^{-1} \approx k(\zeta)$ from Eq. (2.55), and take $T_{e,t} = \exp(-\psi/\sigma_t^2)$ in accordance with our measurements, integration of Eq. (6.11) over the plume cross section yields an expression for the potential drop between the center of the plasma and the plasma boundary,

$$\frac{\Delta\phi_p}{\bar{\phi}} = -\frac{k\sigma_t^2}{\bar{\phi}}\left(1 - e^{-\psi_p/\sigma_t^2}\right) + \frac{2k\psi_p}{\gamma_e} \tag{6.12}$$

Here, we have normalized the potential drop, $\Delta\phi_p$, by the average potential over the cross-section, $\bar{\phi}$. The first term represents only a small correction for $\gamma_e\sigma_t^2/(2\psi_p\bar{\phi}) \ll 1$, from which we can approximate

$$\frac{\Delta\phi_p}{\bar{\phi}} \approx \frac{2k\psi_p}{\gamma_e}. \tag{6.13}$$

Effectively, this equation describes the scaling of the potential drop required to turn the ions through a curvature equal to the magnetic field curvature.

The simulations of Ahedo and Merino [23, 69] show that there exists a region downstream beyond which the ion trajectory linearizes. In other words, the ambipolar potential is insufficient to deflect the ions through the full curvature of the

magnetic field. This suggests that there is a fundamental limit to the value $\Delta\phi_p/\bar{\phi}$ sustainable by the plasma. Because the value of $\Delta\phi_p/\bar{\phi}$ dictates the non-uniformities that develop in the flow, which result from ion cross-field motion, we expect this limit to lie somewhere within the range $(\Delta\phi_p/\bar{\phi})^* \sim 0.1 - 1$.

Using the simplifications $k \approx 3z_\zeta/4$ and $\psi_p \approx r_p^2/2$, we estimate the location at which the influence of the ambipolar electric field over the ion motion breaks down as

$$z_\zeta^* \approx \frac{4\gamma_e}{3r_p^2} \left(\frac{\Delta\phi}{\bar{\phi}}\right)^*. \tag{6.14}$$

Here, z_ζ represents the axial location of the ζ-surface at $r = 0$. We see that the ion separation location is pushed downstream as the ratio of the plasma radius to the magnet radius, r_p, decreases. This effect can be attributed to a combination of the slower rate of ion acceleration through the nozzle and lower field divergence inherent to small r_p.

It is interesting to compare z_ζ^* with the turning point of the nozzle. We recall that the cross-sectional surface corresponding to the MN turning point can be estimated from $\zeta_{\mathrm{tp}} \approx 2.5\psi_p^2 \approx 5r_p^4/8$. Noting that $z_{\zeta,\mathrm{tp}} = (2\zeta_{\mathrm{tp}})^{-1/2}$, the location of the turning point is well-approximated as $z_{\zeta,\mathrm{tp}} \approx 4/(\pi r_p^2)$. Therefore we find that $z_\zeta^* < z_{\zeta,\mathrm{tp}}$ is always satisfied for the expected value of $(\Delta\phi_p/\bar{\phi})^*$. In other words, the ions are no longer under the influence of the ambipolar electric field as they reach the turning point of the nozzle. This observation agrees with recent simulations by Merino and Ahedo [9].

Finally, we can estimate a value for $(\Delta\phi_p/\bar{\phi})^*$ using the data in Fig. 6.1. Recall that the under-collimated plume corresponds to the failure of confinement for $z_\zeta < z_\zeta^*$. The data in Fig. 6.1 for $I_B = 7.5$ A suggests that this case is near the transition between these two regimes. From Fig. 6.8 we see that confinement breaks down near $z_\zeta \approx 31/7.511 \approx 4.1$. For $r_p \approx 0.41$ and $\gamma_e \approx 1.15$, this yields a value $(\Delta\phi_p/\bar{\phi})^* \approx 0.5$. Therefore, our data suggests the plasma is only capable of sustaining a potential

drop nearly half as large as the average potential. This result agrees qualitatively with the initial observations of Ahedo and Merino for the existence of both inward and outward ion separation [69], although a direct comparison is not possible because the magnetic field used in their simulations diverges at a slower rate than the dipole magnetic field implied by our assumptions.

Plume collimation mode transition

We can now analyze the transition from an under-collimated plume to a collimated plume within the context of the ion response to electron demagnetization. The radius of the plasma where ion ambipolarity breaks down can be found using the approximation $r_\zeta \approx \sqrt{2\psi_p} z_\zeta^{3/2}$. Letting $(\Delta\phi_p/\bar{\phi})^* = 1/2$, we find this radius to scale as

$$r^* \approx \frac{1}{r_p^2} \left(\frac{2\gamma_e}{3}\right)^{3/2} \tag{6.15}$$

Interestingly, r^* increases as the initial plume radius decreases. Recall that in the limit where $u_{\theta e,t}(\psi_p) \ll \epsilon_\psi r_p/(2r_L^2)$, the demagnetization radius is given by

$$r_d \approx \frac{r_p}{r_L} \sqrt{\frac{\epsilon_\psi}{2H'(\psi_p)}}, \tag{6.16}$$

which indicates that the demagnetization radius scales linearly with the ratio of the plasma and electron Larmor radii at the throat.

These characteristic radii describe the transition between under-collimated and collimated flows. If $r_d < r^*$, the electrons demagnetize while maintaining influence over the ions. The ions are deflected outwards with respect to the diverging magnetic field, producing an under-collimated plume. For $r_d > r^*$, the ion kinetic energy is too strong for them to be deflected by the outward electron expansion. The ion motion is then unimpeded in the far-field, resulting in a collimated plume. In this case, the outward electron separation and inward ion separation produces an apparent incon-

142

sistency. However, the fluid model should only be considered accurate to the point where the electrons demagnetize. After this point, more complex phenomenon will likely allow the electrons to flow downstream to neutralize the ion plume. Irrespective of these phenomenon, a detached ion beam has been demonstrated even under the assumption of fully magnetized electrons, which suggests that ion detachment is a robust feature of MN plasma flows [9].

Relationship to the performance model

In Sec. 6.1 we derived a scaling relation for the divergence efficiency of a MN, which suggests that the divergence of the nozzle is independent of the applied field strength. Implicit in this derivation was the assumption that the plasma remained confined through the turning point of the expanding magnetic field. The results of this section suggest an addendum to this model for $r_d < r^*$.

Specifically, the loss of confinement implies that momentum is no longer transferred between the plasma and MN. The domain of the performance model should then be limited to the region upstream from the location where the electrons demagnetize. Eq. (6.16) implies that the nozzle expansion ratio, $(r_d/r_p)^2$, scales with the applied field strength squared. Therefore, the field strength is an important quantity in this regime because it determines how much thermal energy is converted into ion kinetic energy prior to electron demagnetization. This is especially true in light of the fact that expansion for $\gamma_e \approx 1.2$ occurs over a fairly long length scale.

It is reasonable to question: *why not increase the magnetic field strength such that* $r_d > r^*$? For our experimental parameters, we can set $r_d = r^*$ within Eqs. (6.15) and (6.16) to find a critical magnetic field strength of $B_c^* \sim 160$ G, which corresponds to the transition between an under-collimated and collimated plume. This value agrees well with our observation that the transition occurs near $I_b = 7.5$ A. Indeed, magnetic fields of this magnitude are relatively easy to produce using either permanent magnets

or electromagnets, and are feasible for a plasma propulsion system. However, we showed in Chapter 2 that electron temperatures in excess of 50 eV are required to outweigh ionization losses. Furthermore, r_p should remain small to limit the plume divergence. If we take our system and assume instead that $T_e = 50$ eV and $r_p = 0.2$, we calculate $B_c^* \sim 10$ kG for a collimated plume – a value that becomes exceeding harder to engineering. Consequently, the parameters required of a highly efficient MN thruster will likely limit operation to an under-collimated plume, thus limiting the performance model domain to $r < r_d$.

6.4   Chapter summary

In this chapter, we have experimentally analyzed the influence of the applied magnetic field strength on the plume divergence of a MN plasma. We found that decreasing the strength of the applied magnetic field invokes a transition from a collimated plume to an under-collimated plume, where an under-collimated plume is defined such that the plume divergence is greater than the magnetic field divergence.

Measurements of the transverse density and potential profiles revealed the presence of an energized population of ions near the plasma periphery. We saw that this population results in the formation of a potential well near the predicted free-jet boundary of the plasma. The potential well is formed by a charge layer that develops in this region in response to the energetic ions overshooting the magnetized electrons. Comparing the potential profile for the under-collimated and collimated plumes, we found a correlation between the disappearance of the potential well and the rapid divergence of the under-collimated plume.

The presence of the potential well acts as an indication of plasma confinement in the downstream region. We used this as a metric to compare our experimental findings with existing theories for electron demagnetization. We showed that the

disappearance of the potential well scales with the location at which electron finite Larmor radius effects become of dominant order. This suggests that confinement is lost as the electrons demagnetize. Furthermore, the residual thermal energy of the electrons forces an outward expansion in a process similar to that of an under-expanded nozzle.

Finally, we considered the ion response to the demagnetization of the electron cloud. We derived a condition that characterizes the ability of the ions to respond to the ambipolar electric field formed in the wake of the expanding electrons. Using this condition, we found a simple requirement on the magnetic field strength that must be met to ensure a collimated plume.

Chapter 7

Conclusion

> *"Every passing hour brings the Solar System forty three thousand miles closer to Globular Cluster M13 in Hercules – and still there are some misfits who insist that there is no such thing as progress."*
>
> – Kurt Vonnegut, *The Sirens of Titan*

This dissertation includes the major findings from our investigation into the performance scaling of magnetic nozzles for electric propulsion systems. In spite of the large body of literature formed around our understanding of the physical processes in MNs and their influence on plasma propulsion [7, 17, 23, 67, 68, 72, 69, 9, 70], the measured performance of MN thrusters has failed to meet theoretical expectations [55, 56, 57, 58, 60, 61, 62, 63]. To understand why, we posed at the outset the fundamental question: *Under what conditions is it possible to efficiently produce thrust by accelerating plasma through a magnetic nozzle?*

Throughout the course of answering this question, we used both theoretical and experimental investigation of the fundamental processes in MN plasmas. We used a simple model for the plasma channel to analyze the mass utilization and channel efficiency scaling. We derived an analytical solution to a 2D fluid model [23], and used this solution to examine the scaling of the plume divergence. To obtain a better

understanding of the physical processes relevant to our performance model, and to verify some of its predictions, we built an experiment consisting of a helicon plasma source and MN.

We present performance estimates obtained from our experimental measurements in Sec. 7.1. The major findings of our analytical and experimental investigation are summarized in Sec. 7.2. We conclude the dissertation in Sec. 7.3 with a discussion of future research pathways.

7.1   Performance estimate

We designed our experiment to probe the fundamental dynamics of plasma flow through a magnetic nozzle. As a result, our thruster was not optimized for propulsion applications and we did not perform direct thrust measurements. However, it is constructive to estimate the performance of the thruster and the relative contribution of the various loss processes. We emphasize the fact that the performance numbers contained in this section are estimated from our theoretical model and probe measurements, and were not directly measured.

We include in Tab. 7.1 the estimated performance of our thruster operating in both the low confinement (LC) and high confinement (HC) modes for $\dot{m} = 0.5$ mg/s, $P = 500$ W, and $L_{\mathrm{bp}} = 18.5$ cm. The final column contains the method used to obtain the values in the second and third columns. Here, we show either the equation number, the equation itself, or the section that describes how the parameter was obtained. The values of each parameter are included along with their estimated error, or in some cases, a broad range in which the value may fall.

The plasma density and electron temperature correspond to measurements at the throat center. The density difference between the LC and HC modes is consistent with the behavior shown in Fig. 4.3, where plasma diffusion to the wall dominates

Table 7.1: Performance estimates for low and high confinement mode operation

Parameter	Low Confinement	High Confinement	Method
Magnetic Field, B_0 (G)	105	420	Input
Mass Flow Rate, $\dot{m}$ (mg/s)	0.5	0.5	Input
RF Power, P (W)	500	500	Input
Backplate Location, L_{bp} (cm)	18.5	18.5	Input
Plasma Density, n (m^{-3})	$(1.4 \pm 0.1) \times 10^{17}$	$(1.6 \pm 0.1) \times 10^{18}$	Measured
Electron Temperature, T_e (eV)	6.4 ± 0.6	7.9 ± 0.8	Measured
Electron Polytropic Index, γ_e	1.15 ± 0.03	1.15 ± 0.03	Measured
Ion Acoustic Speed, c_s (km/s)	4.2 ± 0.2	4.7 ± 0.2	$(\gamma_e T_e/m_i)^{1/2}$
Velocity Increment, g_u	3.8 ± 0.1	3.8 ± 0.1	Eq. (2.25)
Thrust, F (mN)	0.5 ± 0.1	4.2 ± 0.5	Eq. (1.3)
Specific Impulse, I_{sp} (s)	100 ± 10	860 ± 100	Eq. (1.4)
Ionization Parameter, Λ	3 ± 1	5 ± 1	Eq. (2.7)
Neutral Pumping Parameter, Π	1.0 ± 0.1	0.8 ± 0.1	Eqs. (2.7)-(2.8)
Confinement Parameter, Ψ	$\sim 0.01 - 1$	$\sim 0.001 - 0.03$	Eq. (2.9)
Anisotropic Peclet Number, Pe$_{an}$	0.12 ± 0.05	2.8 ± 0.9	Eq. (2.9)
Ion Wall Flux/Ion Exit Flux, μ_w	< 7	< 0.03	Eq. (2.18)
Fast Neutral Exit Flux/Ion Exit Flux, μ_f	$\sim 1 - 13$	$\sim 0.67 - 0.88$	Eq. (2.21)
Mass Utilization Efficiency, η_m	0.07 ± 0.01	0.53 ± 0.04	Sec. (4.3)
Divergence Efficiency, η_{div}	0.36 ± 0.09	0.81 ± 0.05	Eq. (6.2)
Channel Efficiency, η_c	0.14 ± 0.05	0.97 ± 0.03	Eq. (2.14)
Thermal Conversion Efficiency, η_{conv}	0.57 ± 0.05	0.62 ± 0.04	Eq. (2.27)
Plasma Source Efficiency, η_{ps}	0.3 ± 0.1	0.3 ± 0.1	Eq. (1.5)
Thrust Efficiency, η_T	$(0.05 \pm 0.01) \times 10^{-2}$	0.04 ± 0.01	Eq. (1.5)

advection along the magnetic field in the LC mode. The increased wall losses accompanied with a transition to the LC mode are reflected in a number of parameters: (1) the confinement parameter, which takes a range of values due to the convergent nature of the magnetic field in the channel, increases by an order of magnitude, (2) the anisotropic Péclet number (calculated at the injection location) decreases by more than an order of magnitude, and (3) the ion wall and fast neutral neutral fluxes dominate the ion flux into the MN. The combined effect is nearly an order of magnitude decrease in the thrust, specific impulse, mass utilization efficiency, and channel efficiency. As a result, we estimate the thrust efficiency to differ by nearly two orders of magnitude between the two modes. The difference between direct performance measurements will not be this dramatic because our analysis ignores the force imparted to the thruster by the expanding neutral gas.

The estimated performance of our HPT is poor compared to state of the art EP technology (Fig. 1.5), even for the HC mode. Furthermore, the estimated specific impulse and thrust efficiency are only marginally better than HPTs found in the literature at similar powers ($I_{\mathrm{sp}} \leq 530$ s and $\eta_T \leq 0.03$ for $P \leq 500$ W [58, 60, 55, 66, 62]). It is reasonable to suspect given the similarities between our thruster and other HPTs that the relative losses are similar among all devices.

The breadth of our experimental measurements allows us to predict the underlying mechanisms behind the poor estimated performance in the HC mode. For the electron temperature and density inherent to our device, the low thrust and specific impulse result primarily from poor mass utilization, with a secondary influence being the divergence of the exhaust beam. The reason for the poor mass utilization is likely CEX collisions as $\Psi \ll 1$ and $\Pi \sim 1$. As we found in Sec. 2.3, CEX losses can only be remedied through operation at higher electron temperatures. The thrust efficiency is mainly affected by the mass utilization, thermal conversion, and plasma source efficiencies. Again, the mass utilization and thermal conversion efficiency can be

increased by operating at higher electron temperatures. The plasma source efficiency, which in our model includes losses due to antenna-plasma coupling and the flux of plasma to the rear wall of the device, is the primary reason for the low thrust efficiency. If we assume the ion flux to the rear wall is equal to the ion flux from the device [17], we find that nearly 60 W are being deposited to the backplate. This implies that, out of the 500 W delivered to the antenna, only 210 W are being coupled to the plasma. The fact that only 40% of the incident power is coupled to the plasma agrees with recent analytical models for a similar plasma source (albeit with a different antenna geometry) [162], and suggests that a deeper understanding of the antenna-plasma interaction should be a priority of future HPT research.

7.2 Summary of major findings

7.2.1 Analytical insight

In our analytical model of the channel region of a MN thruster we have determined that there exists two modes of confinement depending on the relative diffusion, ionization, and transit timescales of the plasma. The plasma flux to the channel walls is important in the low confinement modes. An optimum channel length exists in this mode that leverages the ionization of the incoming propellant with the plasma wall losses. The high confinement mode occurs when cross-field diffusion is limited to the point where the transit timescale is much shorter than the diffusion timescale. Here, the only requirement on the channel length is to ensure it is long enough to allow considerable ionization of the incoming propellant.

The efficiency of the MN requires that the majority of internal energy stored within the plasma is converted into directed kinetic energy. This process consists of two parts: (1) thermal energy conversion, and (2) plume divergence. To maximize the thermal efficiency of the MN, the ion beam energy must be much greater than the effective

ionization energy of the propellant gas. We found that this requirement creates the need for plasma sources capable of reaching electron temperatures in the range of tens to hundreds of electron volts. Above these temperatures, however, we found the mass utilization efficiency to decrease along with the ionization cross section. From this, we conclude that heavier gases such as xenon are the most promising propellant. In regards to the divergence efficiency, we found that the addition of an extra magnet increases the ion Mach number before the exhaust, and could be used to decrease the divergence of the plume.

7.2.2 Experimental insight

With our experimental setup and diagnostics we performed a detailed analysis of the plasma in both the channel and magnetic nozzle regions. Measuring the mass utilization efficiency for various magnetic field strengths and channel lengths, we verified the existence and scaling of the two confinement modes predicted from our channel model. From this, we derived an analytical expression for the critical magnetic field strength required to operate in the high confinement mode.

We used measurements of the electron temperature, density, plasma potential, and ion beam energy along the MN centerline to show that electron cooling in a magnetically expanding plasma may be described using a polytropic law. We demonstrated this point analytically using a quasi-1D expansion model, from which we derived a value for the electron polytropic index in the limit when heat conduction is important. The remarkable agreement between this value and our experimental data suggests that electron heat conduction along the magnetic field plays an important role in the expansion process.

Finally, we used the versatility of our plasma source to investigate the scaling of the plume divergence with the radial plasma profile at the MN throat and magnetic field strength. We verified the prediction that the divergence decreases as the plasma is

more concentrated towards the axis [23] – an observation that agreed reasonably well with our theoretical scaling law. By decreasing the applied magnetic field strength, we found that a transition occurs from a collimated plume to an under-collimated plume, where we defined an under-collimated plume such that the plume divergence is greater than the magnetic field divergence. Using a detailed analysis of the density and potential profiles in the exhaust, we showed that the increased divergence of the under-collimated plume is consistent with a theoretical model [7] for the demagnetization of the electrons via finite Larmor radius effects.

7.3   Future work

Our work here indicates that improvements in both our fundamental understanding of the plasma physics relevant to MNs and the characteristics of the plasma sources used for MN plasma propulsion are required before this technology becomes competitive with existing electric propulsion systems.

The results presented in Chapter 4 suggest that classical diffusion dominates the plasma losses to the channel walls in our experiment. This need not necessarily be the case, however, as helicon plasma sources operating at higher pressures and magnetic fields have exhibited signs of non-classical diffusion [163, 164]. The enhanced diffusion is thought to result from turbulent transport resulting from drift wave instabilities near the outer regions of the plasma [165]. If we compare the helicon thruster performance model of Ahedo and Navarro-Cavallé [17], which assumes classical diffusion, to that of Lafleur [72], which considered turbulent Bohm diffusion, we find that high efficiency operation in the presence of turbulent diffusion requires significantly higher magnetic fields. Because the instabilities that lead to turbulent diffusion typically only become dominant at large fields ($B \geq 1,000$ G) [166, 164], there may exist

an interesting tradeoff between the formation of these instabilities and the desire to suppress the resulting turbulent diffusion.

As we mentioned briefly in Sec. 6.2, the onset of instabilities near the periphery of the downstream plasma may play an important role in ion energization and electron cross-field diffusion. Future work could concentrate on verifying the existence of high energy ions at the plasma periphery with direct measurements of the IEDF using laser-induced fluorescence spectroscopy. Ion acoustic turbulence (IAT) is suspected of creating high energy ions in the plume of hollow cathode plasmas [167]. A similar process may be occurring in the MN plume. Electric probes could be used to correlate IAT with the appearance of high energy ions, while also assessing the role of turbulence in enhancing electron diffusion [164]

Our analytical model predicts that the divergence efficiency can be improved through the addition of a large exhaust magnet downstream from the MN throat, however; experimental evidence in support of this prediction was not obtained. The benefit of the additional magnet should be experimentally characterized because its inclusion adds weight and complexity to the propulsion system. An alternative method to reduce the plume divergence is to induce azimuthal currents within the plasma prior to exhausting through the nozzle [168]. Initial studies of the theoretical benefit of the induced currents [169], and their measured influence of the MN plume [170], merit further investigation.

Finally, improvements are necessary in the source of the MN plasma flow. The poor measured performance of MN thrusters can be attributed to relatively large ionization losses at low electron temperatures, poor power coupling between the external antenna and plasma, and low mass utilization efficiencies that result from this insufficient coupling. Because the plasma resistance, and therefore the power coupling efficiency [46], generally decreases with increasing temperature, there may exist an optimum operating temperature that balances ionization and power coupling losses.

In light of their importance to the efficiency of these devices, investigations into the physical mechanisms that influence the antenna-plasma coupling within the context of MN plasma sources are worth further consideration.

Appendix A

Magnetic Nozzle Thrust Transfer[1]

We use a Green's function approach to prove the claim that momentum is transferred to a magnetic nozzle by induced plasma currents – a mechanism predicted as early as Seikel [3]. Taking the reference frame of the nozzle coil and considering the force transmitted to the coil by volumetric and surface currents within the plasma downstream the nozzle throat, we ultimately arrive at the same thrust expression that Ahedo and Merino [23] derived using a control volume analysis. We then return to the control volume derivation to expand upon their result to include the influence of induced magnetic fields.

We begin with the assumption that the applied magnetic field is generated by a single current loop of infinitesimal cross-section with strength, I. For this analysis, we ignore all other magnetic coils within the source region. The force experienced by the current loop, or "nozzle coil," is given by the integral of the Lorentz force acting over its circumference

$$\mathbf{F}^c = \oint_{coil} \mathbf{I} \times \mathbf{B}^{(i)} dl, \tag{A.1}$$

---

[1]This appendix contains theoretical results presented in [85]: J. M. Little and E. Y. Choueiri, "The influence of induced currents on magnetic nozzle acceleration and plasma detachment," *Proceedings of 46th Joint Propulsion Conference, Nashville, TN*, AIAA 2010-6615, 2010.

where $\mathbf{B}^{(i)}$ is the induced magnetic field vector due to all other currents within our domain. Clearly, $\mathbf{I} = I\hat{\mathbf{e}}_\theta$, where $\hat{\mathbf{e}}_\theta$ is the unit vector in the azimuthal direction. Therefore, the goal becomes to express the induced magnetic field vector in terms of the surface and volumetric plasma currents.

It has been shown that the axisymmetric nature of a magnetic nozzle inhibits the formation of a significant azimuthal magnetic field component [5] and allows us to ignore any contributions due to currents in the radial and axial direction. This property permits the description of the induced magnetic field in terms of a scalar flux function, ψ,

$$\mathbf{B}^{(i)} = \frac{1}{r}\left(\hat{\mathbf{e}}_\theta \times \nabla\psi\right). \tag{A.2}$$

Substitution of Eq. (A.2) into Ampere's law for a steady-state flow yields the following relationship between ψ and the induced plasma currents, j_θ:

$$L\psi \equiv \frac{1}{r}\nabla^2\psi - \frac{1}{r^2}\frac{\partial\psi}{\partial r} = \mu_0 j_\theta. \tag{A.3}$$

Here, we have defined the operator, L, to correspond to the left-hand side of Ampere's law.

It is possible to define a Green's function, G, for operator L, such that $LG\left(\mathbf{r},\mathbf{r'}\right) = \delta\left(\mathbf{r}-\mathbf{r'}\right)$, where δ is the Dirac delta function. The Green's function takes the form [171]

$$G\left(\mathbf{r},\mathbf{r'}\right) = \frac{1}{2\pi}\frac{\sqrt{rr'}}{k}\left[\left(2-k^2\right)K\left(k^2\right) - 2E\left(k^2\right)\right], \tag{A.4}$$

with

$$k^2 = \frac{4rr'}{\left(r+r'\right)^2 + \left(z-z'\right)^2}. \tag{A.5}$$

Furthermore, we define the inner product between two scalar functions, f and g, as $\langle f, g \rangle = \int fg\,dA$. Here, dA represents the differential area within the $r-z$ plane.

Using Eqs. (A.3) and (A.4) in conjunction with the inner product yields,

$$\langle L\psi, G\rangle - \langle \psi, LG\rangle = \int \nabla \cdot \left(\frac{G}{r}\nabla\psi - \frac{\psi}{r}\nabla G\right) dA. \tag{A.6}$$

where the term on the right-hand side tends to zero for the domain $r \in [0, \infty)$ and $z \in (-\infty, \infty)$. We thus arrive at an expression for the induced flux function in terms of currents developed within the plasma:

$$\psi = \langle L\psi, G\rangle = \mu_0 \langle j_\theta, G\rangle. \tag{A.7}$$

Physically, Eq. (A.7) represents the sum of the differential flux contributions at location $\mathbf{r}$ due to an infinitesimal current loop of strength $j_\theta dr' dz'$ located at $\mathbf{r}'$.

The thrust generated by the expanding plasma is equivalent to the axial component of Eq. (A.1). Denoting $\mathbf{r}_c$ as the radius of the coil and $r_c = \mathbf{r}_c \cdot \hat{\mathbf{e}}_r$, we may express the force on the coil in the axial direction as

$$F_z^c = -2\pi r_c I B_r^{(i)}(\mathbf{r}_c), \tag{A.8}$$

where

$$B_r^{(i)}(\mathbf{r}) = -\frac{\mu_0}{r}\int j_\theta(\mathbf{r}') G_z(\mathbf{r}, \mathbf{r}')dA' - \frac{\mu_0}{r}\int J_\theta(\mathbf{r}') G_z(\mathbf{r}, \mathbf{r}')ds', \tag{A.9}$$

is the radial component of the induced magnetic field as obtained from Eqs. (A.2) and (A.7). j_θ and J_θ are the volumetric and surface current densities within the plasma, respectively. G_z represents the partial derivative of the Green's function with respect to z, and ds' is a differential length element along the plasma-vacuum edge.

We now use Eq. (A.9) and the symmetry of the Green's function derivative, $G_z(\mathbf{r}, \mathbf{r'}) = -G_z(\mathbf{r'}, \mathbf{r})$, to rewrite Eq. (A.8) as

$$F_z^c = \int j_\theta(\mathbf{r'}) \left[-\frac{\mu_0 I}{r'} G_z(\mathbf{r'}, \mathbf{r}_c) \right] 2\pi r' dA' + \int J_\theta(\mathbf{r'}) \left[-\frac{\mu_0 I}{r'} G_z(\mathbf{r'}, \mathbf{r}_c) \right] 2\pi r' ds'. \tag{A.10}$$

Furthermore, we recognize the term in the square brackets as the applied magnetic field,

$$B_r^{(a)}(\mathbf{r}) = -\frac{\mu_0}{r} I G_z(\mathbf{r}, \mathbf{r}_c). \tag{A.11}$$

Due to axisymmetry, we transform the surface and line integrals into volume ($dV' = 2\pi r' dA'$) and surface ($dS' = 2\pi r' ds'$) integrals, respectively. The resulting axial force on the applied field coil is thus,

$$F_z^c = \int j_\theta(\mathbf{r'}) B_r^{(a)}(\mathbf{r'}) dV' + \int J_\theta(\mathbf{r'}) B_r^{(a)}(\mathbf{r'}) dS' = -F_{L,V}^{(a)} - F_{L,S}^{(a)}, \tag{A.12}$$

which is equal and opposite to the integral over all space of the volumetric, $F_{L,V}^{(a)}$, and surface, $F_{L,S}^{(a)}$, Lorentz forces acting on the plasma due to the *applied (a)* magnetic field. Thus, we recover the result obtained by Ahedo and Moreno with the exception that a distinction must be made between the applied magnetic field and the total magnetic field.

With this understanding of momentum transfer for magnetic nozzles, we may now proceed with the classic control volume derivation for thrust. Consider the control volume $CV_1 : r \in [0, \infty); z \in [0, z^*)$, with $z = 0$ denoting the location of the nozzle throat and z^* any location far enough into the plume that the integrals asymptote. Eq. (A.12) allows us to express the thrust as

$$F = F_0 + F_{L,V}^{(a)} + F_{L,S}^{(a)}. \tag{A.13}$$

Here, F_0 is the momentum flux at the nozzle throat, and $F_{L,V}^{(a)}$ and $F_{L,S}^{(a)}$ are integrals of the *applied* volumetric and surface Lorentz forces downstream the throat, respectively.

We now take the sum of the ion and electron momentum equations and integrate over the control volume, $CV_2 : r \in [0, \infty); \; z \in (-\infty, z^*)$. We neglect the electron mass compared to the ion mass ($m_e << M_i$), set the plasma density equal to the ion density ($\rho = \rho_i$), and assume the plasma pressure is isotropic and is the sum of the ion and electron pressures ($p = p_e + p_i$). Eq. (A.13) then allows us to express the thrust as

$$F = F_m + F_p - F_{L,V}^{(i)} - F_{L,S}^{(i)}, \tag{A.14}$$

where

$$F_m = 2\pi \int \rho u_z^2 r \, dr, \;\; F_p = 2\pi \int p r \, dr, \tag{A.15}$$

$$F_{L,V}^{(i)} = -2\pi \int j_\theta B_r^{(i)} r \, dA, \;\; F_{L,S}^{(i)} = -2\pi \int J_\theta B_r^{(i)} r \, ds, \tag{A.16}$$

are the momentum, pressure, and *induced (i)* volumetric and surface Lorentz force contributions to the thrust, respectively. The integrals in Eq.(A.15) are evaluate at $z = z^*$, while the integrals in Eq.(A.16) are evaluated throughout the plasma upstream from the point $z = z^*$.

We recognize Eq. (A.14) as the thrust equation for a conventional nozzle with two additional terms related to the interaction between the plasma currents and the magnetic fields that they induce. Using Ampere's law to express the current densities in terms of the induced magnetic field, Eq.(16) gives rise to the thrust contribution of what is typically regarded as the magnetic pressure. The individual contributions of $F_{L,V}^{(i)}$ and $F_{L,S}^{(i)}$ relative to either F_m or F_p scale linearly with β, where β is defined as the ratio of the plasma energy to the magnetic field energy within the nozzle source. The thrust equation thus becomes equivalent to that of a conventional nozzle in the low-β limit where the momentum carried by induced magnetic fields is negligible compared to the momentum in the flowing plasma.

Finally, physical insight may be gained by considering a third control volume defined as the shell of infinitesimal thickness containing the plasma-vacuum boundary. Integrating the axial component of the momentum equation over this control volume yields

$$\int p\hat{\mathbf{e}}_z \cdot \mathbf{dS} = F_{sp} = F_{L,S}^{(a)} + F_{L,S}^{(i)}. \tag{A.17}$$

Eq. (A.17) describes the confinement of the expanding plasma in the axial direction, which is a balance between the plasma pressure and the Lorentz forces within the induced diamagnetic current layer developed at the plasma edge [23].

A parallel may be drawn between momentum transfer in conventional and magnetic nozzles. In a conventional nozzle, thrust is the result of the pressure distribution along the inner surfaces of the nozzle. A magnetic nozzle, on the other hand, may not have any solid surfaces to balance the pressure of the expanding plasma. Rather, surface currents are induced that effectively act as a "magnetic wall" that both confines the expanding plasma, Eq. (A.17), and transmits the momentum from the plasma to the applied field coil through their mutual interaction, Eq. (A.12).

Appendix B

Magnetic Nozzle Model with Polytropic Cooling

Here we present modifications to an approximate analytical solution [95] to the theoretical model of Ahedo and Merino [23], which we will use throughout the thesis to compare the predicted and observed behavior of an expanding MN plasma. The theoretical model considers the plasma as a quasineutral two-fluid system of ions and electrons where, because collisions are neglected, the interaction between the fluids is governed solely by the ambipolar electric field. Cross-field electron motion is assumed to be negligible, while ions are allowed to separate from the applied magnetic field. This disparity gives rise to finite longitudinal currents in the flow. For simplicity, we will henceforth refer to the theoretical framework initially modeled by Ahedo and Merino as Collisionless Expansion Theory (CET).

The first numerical solutions [23] to CET assumed a cold ion gas and hot, isothermal electron gas. The isothermal assumption is troubling because it requires an infinite heat flux from the plasma source to the MN plasma to maintain the electron temperature throughout the expansion. This problem can be avoided by imposing a

polytropic law for electron cooling, or

$$\hat{b} \cdot \nabla \left(\frac{p_e}{n^{\gamma_e}} \right) = 0. \qquad (B.1)$$

Here, $\hat{b}$ is the magnetic field unit vector, $p_e = n k_b T_e$ is the electron pressure, n is the plasma density, and γ_e is the polytropic index. Eq. (B.1) states that the quantity p_e/n^{γ_e} is constant along a magnetic field. We show in Chapter 5 that the polytropic law is a reasonable assumption for electron cooling, and will experimentally estimate γ_e as a function of the applied magnetic field strength.

We derived in Sec. 2.2 an approximate analytical solution to isothermal electron CET to examine the scaling of the MN efficiency and thrust coefficient with the incoming plasma profile and radius, and the topography of the MN field. We will now modify this solution to incorporate the polytropic law for electrons and a non-uniform electron temperature profile at the entrance boundary condition.

The analytic solution relies on a transformation from cylindrical to magnetic coordinates, where the magnetic coordinates are defined by ψ and ζ such that ψ labels magnetic flux surfaces and ζ labels surfaces everywhere perpendicular to the ψ-surfaces. This condition may be expressed symbolically as

$$\mathbf{B} = -\frac{1}{r} \left(\mathbf{e}_\theta \times \nabla \psi \right) = -\nabla \zeta, \qquad (B.2)$$

where $\mathbf{B}$ is the magnetic field vector and $\mathbf{e}_\theta$ is the unit vector in the azimuthal direction.

The first step is to solve for the ψ-averaged plasma potential as a function of ζ using the quasi-1D expansion equations [1], Modifying these equations to incorporate the polytropic law and a non-uniform entrance plasma, the quasi-1D equation for $\bar{\phi}$

becomes

$$\bar{\phi} - \frac{\gamma_e}{\gamma_e - 1} \left[\left(\frac{A_0}{A} \sqrt{\frac{\gamma_e}{\gamma_e - 2\bar{\phi}}} \right)^{\gamma_e - 1} - 1 \right] = 0. \tag{B.3}$$

Here, $\bar{\phi}$ is the ψ-averaged potential by the electron temperature at the center of the throat. The cross-sectional area of the beam projected on a ζ-surface is given by A, with a value of A_0 at the throat plane.

The potential at any location within the plume may then be approximated by assuming that the cross-field electric field balances the centrifugal force of the ions curving along the magnetic field. Except for the limit of highly magnetized ions for which the Lorentz force plays a role [23], the cross-field force balance may be written as

$$\frac{d\phi}{d\psi} - \frac{2}{\gamma_e r B R_c} \phi + \frac{T_0}{r B R_c} = 0, \tag{B.4}$$

where B and R_c are the magnetic field magnitude and radius of curvature at a given point, and T_0 is the electron temperature profile at the throat. Furthermore, we have assumed that the radial plasma potential profile is uniformly zero at the throat.

The additive constant of the solution to Eq. (B.4) may be found from

$$\int_0^{\psi_p} \left(\phi - \bar{\phi} \right) d\psi = 0, \tag{B.5}$$

with ψ_p representing the bounding magnetic flux surface of the plasma.

Conservation equations along the magnetic field lines in the limit where the angle between the ion velocity unit vector and magnetic field unit vector is small yield algebraic expressions for the remaining parameters of the model in terms of ϕ:

$$u = \sqrt{T_0 - \frac{2}{\gamma_e} \phi}, \tag{B.6}$$

$$n = n_0 \left[\left(\frac{\gamma_e - 1}{\gamma_e} \right) \frac{\phi}{T_0} + 1 \right]^{1/(\gamma_e - 1)}, \tag{B.7}$$

163

$$T = T_0 + \left(\frac{\gamma_e - 1}{\gamma_e} \right) \phi. \tag{B.8}$$

Here, u, n and T are the ion velocity, plasma density, and electron temperature normalized by their values at the center of the MN throat. Furthermore, the ion velocity along the throat plane is assumed to correspond to the local ion acoustic speed.

The solution above inherently assumes that the ions approximately follow the magnetic field lines. While this is a good assumption in the near-field of the nozzle, ion separation in the far-field results in Eq. (B.4) over-predicting the cross-field electric field in this region. We found that conservation of the ion mass flow rate is violated as a result of this over-prediction, and that introducing a correction for mass conservation allows the solution to extend to the far-field with reasonable accuracy.

We define the mass conservation error as $\epsilon_{\dot{m}} = \dot{m}/\dot{m}_0$ where $\dot{m} = \int_\zeta nu\,dA$ is the ion mass flow rate through a ζ-surface. A correction to the plasma potential may then be introduced to the quasi-1D equations such that multiplying the solution to Eqs. (B.4) and (B.5) ensures mass-conservation throughout the plume. This correction, which depends only on the coordinate ζ, may be found from,

$$\frac{1}{2}\gamma_e - \bar{\phi} + \epsilon_{\dot{m}}^2 \left(\alpha_\phi \bar{\phi} - \frac{1}{2}\gamma_e \right) \left[\frac{(\gamma_e - 1)\,\alpha_\phi \bar{\phi} + \gamma_e}{(\gamma_e - 1)\,\bar{\phi} + \gamma_e} \right]^{2/(\gamma_e - 1)} = 0. \tag{B.9}$$

Finally, the corrected ion velocity, density, and temperature may be found by substituting $\phi \to \alpha_\phi \phi$ into Eqs. (B.6)-(B.8).

The solution to Eqs. (B.4), (B.5), and (B.9) depends on the magnetic topology, ψ, electron polytropic index, γ_e, plasma radius, r_p, and the radial density and electron temperature profiles at the nozzle throat, n_0 and T_0, respectively. Note that the solution does not depend on the strength of the magnetic field.

Bibliography

[1] S. Andersen, V. O. Jensen, P. Nielsen, and N. D'Angelo, "Continuous supersonic plasma wind tunnel," *Phys. Fluids*, vol. 12, no. 3, pp. 557–560, 1969.

[2] L. Spitzer, *Physics of Fully Ionized Gases.* Courier Dover Publications, 2013.

[3] G. R. Seikel, "Generation of thrust-electromagnetic thrustors," vol. 22, p. 19, 1962.

[4] R. W. Moses, R. A. Gerwin, and K. F. Schoenberg, "Resistive plasma detachment in nozzle based coaxial thrusters," *AIP Conference Proceedings*, vol. 246, no. 1, pp. 1293–1303, 1992.

[5] E. B. Hooper, "Plasma detachment from a magnetic nozzle," *J. Propul. Power*, vol. 9, no. 5, pp. 757–763, 1993.

[6] A. V. Arefiev and B. N. Breizman, "Magnetohydrodynamic scenario of plasma detachment in a magnetic nozzle," *Phys. plasmas*, vol. 12, no. 043504, 2005.

[7] E. Ahedo and M. Merino, "On plasma detachment in propulsive magnetic nozzles," *Phys. Plasmas*, vol. 18, no. 053504, 2011.

[8] C. Olsen, M. Ballenger, M. Carter, F. Diaz, M. Giambusso, T. Glover, A. Ilin, J. Squire, B. Longmier, E. Bering III, and P. Cloutier, "Investigation of plasma detachment from a magnetic nozzle in the plume of the vx-200 magnetoplasma thruster," *IEEE Trans. Plasma Sci.*, vol. PP, no. 99, 2014.

[9] M. Merino and E. Ahedo, "Plasma detachment in a propulsive magnetic nozzle via ion demagnetization," *Plasma Sources Sci. Tech.*, vol. 23, no. 3, p. 032001, 2014.

[10] I. M. Podgornyi and R. Z. Sagdeev, "Physics of interplanetary plasma and laboratory experiments," *Sov. Phy. Usp.*, vol. 12, pp. 445–462, 1970.

[11] F. R. F. Manheimer, W. M., "Plasma acceleration by area expansion," *IEEE Trans. Plasma Sci.*, vol. 29, pp. 75–84, 2001.

[12] R. G. Jahn, *Physics of Electric Propulsion.* New York, NY: McGraw-Hill, 1968.

[13] D. Pavarin, F. Ferri, M. Manente, and *et al.*, "Design of 50W helicon plasma thruster." 31st International Electric Propulsion Conference, IEPC Paper 2009-205, 2009.

[14] I. G. Mikellides, P. G. Mikellides, P. J. Turchi, and T. M. York, "Design of a fusion propulsion system - part 2: Numerical simulation of magnetic-nozzle flows," *J. Propul. Power*, vol. 18, no. 1, pp. 152–158, 2002.

[15] J. E. Polk, W. von Jaskowsky, A. J. Kelley, and R. G. Jahn, "Measurement of mpd thruster erosion using surface layer activation," *J. Propul. Power*, vol. 3, no. 1, pp. 33–38, 1987.

[16] I. G. Mikellides, I. Katz, R. R. Hofer, and D. M. Goebel, "Magnetic shielding of walls from the unmagnetized ion beam in a hall thruster," *Appl. Phys. Lett.*, vol. 102, no. 023509, 2013.

[17] E. Ahedo and J. Navarro-Cavallé, "Helicon thruster plasma modeling: Two-dimensional fluid-dynamics and propulsive performances," *Phys. Plasmas*, vol. 20, no. 043512, 2013.

[18] J. Gilland, "Mission impacts of in-situ propellant usage for electric propulsion vehicles." Proceedings of the 41st AIAA Joint Propulsion Conference, Tuscon, AZ, AIAA Paper 2005-4267, 2005.

[19] J. M. Little, A. S. Rubin, and E. Y. Choueiri, "Similarity parameter evolution within a magnetic nozzle with applications to laboratory plasmas," in *Proceedings of 32nd International Electric Propulsion Conference, Wiesbaden, Germany.* IEPC-2011-229, 2011.

[20] O. A. Popov, "Characteristics of electron cyclotron resonance plasma sources," *J. Vacuum Sci. Tech.*, vol. 7, no. 3, pp. 894–898, 1989.

[21] E. A. Bering III, F. R. C. Díaz, J. P. Squire, T. W. Glover, M. D. Carter, G. E. McCaskill, B. W. Longmier, M. S. Brukardt, W. J. Chancery, and V. T. Jacobson, "Observations of single-pass ion cyclotron heating in a trans-sonic flowing plasma," *Phys. Plasmas*, vol. 17, no. 4, p. 043509, 2010.

[22] K. Kuriki and O. Okada, "Experimental study of a plasma flow in a magnetic nozzle," *Phys. Fluids*, vol. 13, no. 9, pp. 2262–2269, 1970.

[23] E. Ahedo and M. Merino, "Two-dimensional supersonic plasma acceleration in a magnetic nozzle," *Phys. Plasmas*, vol. 17, no. 073501, 2010.

[24] B. Longmier, E. Bering, M. Carter, and *et al.*, "Ambipolar ion acceleration in an expanding magnetic nozzle," *Plasma Sources Sci. Technol.*, vol. 20, p. 015007, 2011.

[25] C. Charles and R. W. Boswell, "Current-free double-layer formation in a high-density helicon discharge," *Appl. Phys. Lett.*, vol. 82, no. 9, p. 1356, 2003.

[26] A. B. Sefkow and S. A. Cohen, "Particle-in-cell modeling of magnetized argon plasma flow through small mechanical apertures," *Phys. Plasmas*, vol. 16, no. 5, p. 053501, 2009.

[27] E. Ahedo and M. M. Sánchez, "Theory of a stationary current-free double layer in a collisionless plasma," *Phys. Rev. Lett.*, vol. 103, no. 13, p. 135002, 2009.

[28] M. Merino and E. Ahedo, "Two-dimensional quasi-double-layers in two-electron-temperature, current-free plasmas," *Phys. Plasmas*, vol. 20, no. 023502, 2013.

[29] C. Charles, R. Boswell, and M. Lieberman, "Xenon ion beam characterization in a helicon double layer thruster," *Appl. Phys. Lett.*, vol. 89, no. 26, pp. 261 503–261 503, 2006.

[30] S. A. Cohen, X. Sun, N. M. Ferraro, E. E. Scime, M. Miah, S. Stange, N. S. Siefert, and R. F. Boivin, "On collisionless ion and electron populations in the magnetic nozzle experiment (mnx)," *IEEE Trans. Plasma Sci.*, vol. 34, no. 3, pp. 792–803, 2006.

[31] E. L. Walker and G. R. Seikel, "Axisymmetric expansion of a plasma in a magnetic nozzle including thermal conduction," NASA, Tech. Rep. TN D-6154, 1971.

[32] K. Takahashi, T. Lafleur, C. Charles, P. Alexander, and R. W. Boswell, "Electron diamagnetic effect on axial force in an expanding plasma: Experiments and theory," *Phys. Rev. Lett.*, vol. 107, no. 23, p. 235001, 2011.

[33] D. Miller, P. Gloersen, E. Gibbons, and D. BenDaniel, "Cyclotron resonance propulsion system," General Electric Co. Missile and Space Vehicle Dept., Tech. Rep. R62SD29, 1962.

[34] H. Hendel and T. Reboul, "Continuous plasma acceleration at electron cyclotron resonance." AIAA Electric Propulsion Conference, AIAA Paper 63001-63, 1963.

[35] D. B. Miller and E. F. Gibbons, "Experiments with an electron cyclotron resonance plasma accelerator," *AIAA J.*, vol. 2, no. 1, pp. 35–41, 1964.

[36] D. B. Miller and G. W. Bethke, "Cyclotron resonance thruster design techniques," *AIAA J.*, vol. 4, no. 5, pp. 835–840, 1966.

[37] H. G. Kosmahl, D. B. Miller, and G. Bethke, "Plasma acceleration with microwaves near cyclotron resonance," *J.Appl. Phys.*, vol. 38, no. 12, pp. 4576–4582, 1967.

[38] J. C. Sercel, "An experimental and theoretical study of the ecr plasma engine," Ph.D. dissertation, California Institute of Technology, 1993.

[39] B. W. Stallard, E. B. Hooper, and J. L. Power, "Whistler-driven, electron-cyclotron-resonance-heated thruster: Experimental status," *J. Propul. Power*, vol. 12, no. 4, pp. 814–816, 1996.

[40] ——, "Plasma confinement in the whistler wave plasma thruster," *J. Propul. Power*, vol. 17, no. 2, pp. 433–440, 2001.

[41] K. D. Diamant, T. V. Albright, B. L. Zeigler, and W. A. Cox, "Miniature cyclotron resonance thruster." Proceedings of the 47th AIAA Joint Propulsion Conference, AIAA Paper 2011-5882, 2011.

[42] J. Jarrige, P. Q. Elias, F. Cannat, and D. Packan, "Performance comparison of an ecr plasma thruster using argon and xenon as propellant gas," in *Proceedings of 33rd International Electric Propulsion Conference, Washington, D.C.* IEPC-2013-420, 2013.

[43] R. Boswell, "Plasma production using a standing helicon wave," *Phys. Lett. A*, vol. 33, no. 7, pp. 457–458, 1970.

[44] F. F. Chen, "Experiments on helicon plasma sources," *J. Vac. Sci. Technol. A*, vol. 10, no. 4, pp. 1389–1401, 1992.

[45] J. Stevens, M. Sowa, and J. Cecchi, "Helicon plasma source excited by a flat spiral coil," *J. Vac. Sci. Technol. A*, vol. 13, no. 5, pp. 2476–2482, 1995.

[46] P. Chabert and N. Braithwaite, *Physics of Radio-Frequency Plasmas.* Cambridge University Press, 2011.

[47] O. V. Batishchev, "Minihelicon plasma thruster," *IEEE Trans. Plasma Sci.*, vol. 37, no. 8, pp. 1563–1571, 2009.

[48] E. Ahedo, "Double-layer formation and propulsive assessment for a three-species plasma expanding in a magnetic nozzle," *Phys. Plasmas*, vol. 18, p. 033510, 2011.

[49] M. A. Lieberman, C. Charles, and R. W. Boswell, "A theory for formation of a low pressure, current-free double layer," *J. Phys. D*, vol. 39, no. 15, p. 3294, 2006.

[50] A. Fruchtman, "Electric field in a double layer and the imparted momentum," *Phys. Rev. Lett.*, vol. 96, no. 6, p. 065002, 2006.

[51] K. A. Polzin, T. E. Markusic, B. J. Stanojev, A. DeHoyos, and B. Spaun, "Thrust stand for electric propulsion performance evaluation," *Rev. Sci. Instrum.*, vol. 77, no. 10, p. 105108, 2006.

[52] M. L. R Walker, A. L. Victor, R. R. Hofer, and A. D. Gallimore, "Effect of backpressure on ion current density measurements in hall thruster plumes," *J. Propul. Power*, vol. 21, no. 3, pp. 408–415, 2005.

[53] E. A. Cubbin, J. K. Ziemer, E. Y. Choueiri, and R. G. Jahn, "Pulsed thrust measurements using laser interferometry," *Review of Scientific Instruments*, vol. 68, no. 6, pp. 2339–2346, 1997.

[54] A. P. Pancotti, M. Gilpin, and M. S. Hilario, "Comparison of electrostatic fins with piezoelectric impact hammer techniques to extend impulse calibration range of a torsional thrust stand," *Rev. Sci. Instrum.*, vol. 83, no. 3, p. 035109, 2012.

[55] S. Pottinger, V. Lappas, C. Charles, and R. W. Boswell, "Performance characterization of a helicon double layer thruster using direct thrust measurements," *J. Phys. D: Appl. Physics*, vol. 44, no. 23, p. 235201, 2011.

[56] K. Takahashi, T. Lafleur, C. Charles, P. Alexander, R. W. Boswell, M. Perren, R. Laine, S. Pottinger, V. Lappas, T. Harle *et al.*, "Direct thrust measurement of a permanent magnet helicon double layer thruster," *Appl. Phys. Lett.*, vol. 98, no. 14, p. 141503, 2011.

[57] T. Harle, S. J. Pottinger, and V. J. Lappas, "Helicon double layer thruster operation in a low magnetic field mode," *Plasma Sources Sci. Tech.*, vol. 22, no. 1, p. 015015, 2013.

[58] L. T. Williams and M. L. R. Walker, "Thrust measurements of a radio frequency plasma source," *J. Propul.Power*, vol. 29, no. 3, pp. 520–527, 2013.

[59] L. T. Williams, "Ion acceleration mechanisms of helicon thrusters," Ph.D. dissertation, Georgia Institute of Technology, 2013.

[60] A. Shabshelowitz and A. D. Gallimore, "Performance and probe measurements of a radio-frequency plasma thruster," *J. Propul. Power*, pp. 1–11, 2013.

[61] K. Takahashi, C. Charles, R. W. Boswell, and A. Ando, "Performance improvement of a permanent magnet helicon plasma thruster," *J. Phys. D: Appl. Physics*, vol. 46, no. 35, p. 352001, 2013.

[62] K. Takahashi, C. Charles, and R. W. Boswell, "Approaching the theoretical limit of diamagnetic-induced momentum in a rapidly diverging magnetic nozzle," *Phys. Rev. Lett.*, vol. 110, no. 19, p. 195003, 2013.

[63] K. Takahashi, C. Charles, R. Boswell, and A. Ando, "Effect of magnetic and physical nozzles on plasma thruster performance," *Plasma Sources Sci. Tech.*, vol. 23, no. 4, p. 044004, 2014.

[64] K. D. Diamant, R. Liang, and R. L. Corey, "The effect of background pressure on spt-100 hall thruster performance."

[65] M. L. R. Walker, "Effects of facility backpressure on the performance and plume of a hall thruster," Ph.D. dissertation, Georgia Institute of Technology, 2005.

[66] C. Charles, K. Takahashi, and R. Boswell, "Axial force imparted by a conical radiofrequency magneto-plasma thruster," *Appl. Phys. Lett.*, vol. 100, no. 11, pp. 113 504–113 504, 2012.

[67] A. Fruchtman, "Neutral depletion in a collisionless plasma," *IEEE Trans. Plasma Sci.*, vol. 36, no. 2, pp. 403–413, 2008.

[68] ——, "The thrust of a collisional-plasma source," *IEEE Trans. Plasma Sci.*, vol. 39, no. 1, pp. 530–539, 2011.

[69] E. Ahedo and M. Merino, "Two-dimensional plasma expansion in a magnetic nozzle: Separation due to electron inertia," *Phys. Plasmas*, vol. 19, no. 083501, 2012.

[70] M. Merino and E. Ahedo, "Influence of electron and ion thermodynamics on the magnetic nozzle plasma expansion," *IEEE Trans. Plasma Sci.*, vol. PP, no. 99, 2014.

[71] C. Charles, R. Boswell, and K. Takahashi, "Investigation of radiofrequency plasma sources for space travel," *Plasma Phys. Contr. F.*, vol. 54, no. 12, p. 124021, 2012.

[72] T. Lafleur, "Helicon plasma thruster discharge model," *Phys. Plasmas*, vol. 21, no. 4, p. 043507, 2014.

[73] J. M. Little and E. Y. Choueiri, "Critical condition for plasma confinement in the source of a magnetic nozzle flow," *IEEE Trans. Plasma Sci.*, vol. PP, no. 99, 2014.

[74] A. Fruchtman, G. Makrinich, and J. Ashkenazy, "Two-dimensional equilibrium of a low temperature magnetized plasma," *Plasma Sources Sci. Technol.*, vol. 14, no. 1, p. 152, 2005.

[75] E. Ahedo, J. M. Gallardo, and M. Martınez-Sánchez, "Effects of the radial plasma-wall interaction on the hall thruster discharge," *Phys. Plasmas*, vol. 10, no. 8, pp. 3397–3409, 2003.

[76] H. Hügel, G. Krülle, and T. Peters, "Investigations on plasma thrusters with thermal and self-magnetic acceleration." *AIAA J.*, vol. 5, no. 3, pp. 551–558, 1967.

[77] T. Lafleur, K. Takahashi, C. Charles, and R. Boswell, "Direct thrust measurements and modelling of a radio-frequency expanding plasma thruster," *Phys. Plasmas*, vol. 18, no. 8, p. 080701, 2011.

[78] E. Ahedo, "Magnetic confinement of a high-density cylindrical plasma," *Phys. Plasmas*, vol. 18, no. 10, p. 103506, 2011.

[79] T. Gronych, R. Ulman, L. Peksa, and P. Řepa, "Measurements of the relative momentum accommodation coefficient for different gases with a viscosity vacuum gauge," *Vacuum*, vol. 73, no. 2, pp. 275–279, 2004.

[80] N. Sternberg, V. Godyak, and D. Hoffman, "Magnetic field effects on gas discharge plasmas," *Phys. Plasmas*, vol. 13, no. 6, p. 063511, 2006.

[81] J. Hanna and C. Watts, "Alfven wave propagation in a helicon plasma," *Phys. Plasmas*, vol. 8, no. 9, pp. 4251–4254, 2001.

[82] A. M. Keesee and E. E. Scime, "Neutral density profiles in argon helicon plasmas," *Plasma Sources Sci. Tech.*, vol. 16, no. 4, p. 742, 2007.

[83] S. M. Rossnagel, S. J. Whitehair, C. R. Guarnieri, and J. J. Cuomo, "Plasma induced gas heating in electron cyclotron resonance sources," *J. Vac. Sci. Technol. A*, vol. 8, no. 4, pp. 3113–3117, 1990.

[84] M. Lampe, G. Joyce, W. M. Manheimer, and S. P. Slinker, "Quasi-neutral particle simulation of magnetized plasma discharges: general formalism and application to ecr discharges," *IEEE Trans. Plasma Sci.*, vol. 26, no. 6, pp. 1592–1609, 1998.

[85] J. M. Little and E. Y. Choueiri, "The influence of induced currents on magnetic nozzle acceleration and plasma detachment," in *Proceedings of 46th Joint Propulsion Conference, Nashville, TN (American Institute of Aeronautics and Astronautics, Washington DC, 2010), AIAA Paper*, no. 2010-6615, 2010.

[86] I. D. Sudit and F. F. Chen, "Discharge equilibrium of a helicon plasma," *Plasma Sources Sci. Technol.*, vol. 5, no. 1, p. 43, 1996.

[87] D. M. Goebel and I. Katz, *Fundamentals of electric propulsion: ion and Hall thrusters.* John Wiley & Sons, 2008, vol. 1.

[88] E. Ahedo, "Parametric analysis of a magnetized cylindrical plasma," *Phys. Plasmas*, vol. 16, no. 11, p. 113503, 2009.

[89] F. N. Gesto, B. D. Blackwell, C. Charles, and R. W. Boswell, "Ion detachment in the helicon double-layer thruster exhaust beam," *J. Propulsion Power*, vol. 22, no. 1, pp. 24–30, 2006.

[90] K. Terasaka, S. Yoshimura, K. Ogiwara, M. Aramaki, and M. Y. Tanaka, "Experimental studies on ion acceleration and stream line detachment in a diverging magnetic field," *Phys. Plasmas*, vol. 17, no. 7, p. 072106, 2010.

[91] M. Auweter-Kurtz, H. Kurtz, H. Schrade, and P. Sleziona, "Numerical modeling of the flow discharge in mpd thrusters," *J Propul. Power*, vol. 5, no. 1, pp. 49–55, 1989.

[92] M. Martinez-Sanchez, "Structure of self-field accelerated plasma flows," *J Propul. Power*, vol. 7, no. 1, pp. 56–64, 1991.

[93] A. Passaro, A. Vicini, F. Nania, and L. Biagioni, "Numerical rebuilding of smart-1 hall effect thruster plasma plume," *J Propul. Power*, vol. 26, no. 1, pp. 149–158, 2010.

[94] E. Ahedo, "Plasma dynamics in a helicon thruster," in *Progress in Propulsion Physics*, vol. 4. EDP Sciences, 2013, pp. 337–354.

[95] J. M. Little and E. Y. Choueiri, "Thrust and efficiency model for electron-driven magnetic nozzles," *Phys. Plasmas*, vol. 20, p. 103501, 2013.

[96] A. Fruchtman, K. Takahashi, C. Charles, and R. Boswell, "A magnetic nozzle calculation of the force on a plasma," *Phys. Plasmas*, vol. 19, no. 3, p. 033507, 2012.

[97] R. Winglee, T. Ziemba, L. Giersch, J. Prager, J. Carscadden, and B. Roberson, "Simulation and laboratory validation of magnetic nozzle effects for the high power helicon thruster," *Phys. Plasmas*, vol. 14, p. 063501, 2007.

[98] C. A. Deline, R. D. Bengtson, B. N. Breizman, M. R. Tushentsov, J. E. Jones, D. G. Chavers, C. C. Dobson, and B. M. Schuettpelz, "Plume detachment from a magnetic nozzle," *Phys. Plasmas*, vol. 16, p. 033502, 2009.

[99] K. Takahashi, Y. Itoh, and T. Fujiwara, "Operation of a permanent-magnets-expanding plasma source connected to a large-volume diffusion chamber," *J. Phys. D*, vol. 44, no. 1, p. 015204, 2011.

[100] F. F. Chen, *Introduction to plasma physics and controlled fusion. Volume 1, Plasma physics*, 2nd ed. Springer, 1984.

[101] B. Smirnov, "Tables for cross sections of the resonant charge exchange process," *Physica Scripta*, vol. 61, no. 5, p. 595, 2000.

[102] W. Lotz, "Electron-impact ionization cross-sections and ionization rate coefficients for atoms and ions from hydrogen to calcium," *Zeitschrift für Physik*, vol. 216, no. 3, pp. 241–247, 1968.

[103] J. V. Dugan Jr and R. J. Sovie, "Volume ion production costs in tenuous plasmas: A general atom theory and detailed results for helium, argon, and cesium." National Aeronautics and Space Administration, Cleveland, Ohio. Lewis Research Center, Tech. Rep., 1967.

[104] J. P. Sheehan, B. W. Longmier, E. A. Bering, C. S. Olsen, J. P. Squire, M. G. Ballenger, M. D. Carter, L. D. Cassady, F. R. C. Díaz, T. W. Glover *et al.*, "Temperature gradients due to adiabatic plasma expansion in a magnetic nozzle," *Plasma Sources Sci. Tech,*, vol. 23, no. 4, p. 045014, 2014.

[105] W. E. Drummond and M. N. Rosenbluth, "Anomalous diffusion arising from microinstabilities in a plasma," *Phys. Fluids*, vol. 5, no. 12, pp. 1507–1513, 1962.

[106] M. D. West, C. Charles, and R. W. Boswell, "Operating radio frequency antennas immersed in vacuum: Implications for ground-testing plasma thrusters," *J. Propul. Power*, vol. 26, no. 4, pp. 892–896, 2010.

[107] C. Bowick, *RF Circuit Design.* Newnes, 1982.

[108] I. D. Sudit and F. F. Chen, "Rf compensated probes for high-density discharges," *Plasma Sources Sci. Technol.*, vol. 3, no. 2, p. 162, 1994.

[109] A. Boschi and F. Magistrelli, "Effect of a r.f. signal on the characteristic of a langmuir probe," *Il Nuovo Cimento*, vol. 29, no. 2, pp. 487–499, 1963.

[110] P. Chung, L. Talbot, and K. Touryan, "Electric probes in stationary and flowing plasmas: theory and application," 1975.

[111] A. Schwabedissen, E. C. Benck, and J. R. Roberts, "Langmuir probe measurements in an inductively coupled plasma source," *Phys. Rev. E*, vol. 55, no. 3, p. 3450, 1997.

[112] F. F. Chen, "Langmuir probe analysis for high density plasmas," *Phys. Plasmas*, vol. 8, p. 3029, 2001.

[113] A. Smirnov, Y. Raitses, and N. J. Fisch, "Plasma measurements in a 100 w cylindrical hall thruster," *J. Appl. Phys.*, vol. 95, no. 5, pp. 2283–2292, 2004.

[114] I. H. Hutchinson, *Principles of plasma diagnostics.* Cambridge university press, 2005.

[115] J. P. Sheehan and N. Hershkowitz, "Emissive probes," *Plasma Sources Sci. Tech.*, vol. 20, no. 6, p. 063001, 2011.

[116] S. Iizuka, P. Michelsen, J. J. Rasmussen, R. Schrittwieser, R. Hatakeyama, K. Saeki, and N. Sato, "A method for measuring fast time evolutions of the plasma potential by means of a simple emissive probe," *J. Phys. E*, vol. 14, no. 11, p. 1291, 1981.

[117] L. Dorf, Y. Raitses, and N. J. Fisch, "Electrostatic probe apparatus for measurements in the near-anode region of hall thrusters," *Rev. Sci. Instr.*, vol. 75, no. 5, pp. 1255–1260, 2004.

[118] D. L. Brown and A. D. Gallimore, "Evaluation of ion collection area in faraday probes," *Rev. Sci. Instr.*, vol. 81, no. 6, p. 063504, 2010.

[119] Y. Azziz, "Experimental and theoretical characterization of a hall thruster plume," Ph.D. dissertation, Massachusetts Institute of Technology, 2007.

[120] J. D. Sommerville and L. B. King, "Hall-effect thruster–cathode coupling, part ii: Ion beam and near-field plume," *J. Propul. Power*, vol. 27, no. 4, pp. 754–767, 2011.

[121] A. Ellingboe and R. Boswell, "Capacitive, inductive and helicon-wave modes of operation of a helicon plasma source," *Phys. Plasmas*, vol. 3, p. 2797, 1996.

[122] R. Boswell, "Very efficient plasma generation by whistler waves near the lower hybrid frequency," *Plasma Phys. Control. Fusion*, vol. 26, no. 10, p. 1147, 1984.

[123] C. M. Franck, O. Grulke, and T. Klinger, "Mode transitions in helicon discharges," *Phys. Plasmas*, vol. 10, no. 1, pp. 323–325, 2002.

[124] T. Lafleur, C. Charles, and R. W. Boswell, "Electron temperature characterization and power balance in a low magnetic field helicon mode," *J. Phys. D: Appl. Physics*, vol. 44, no. 18, p. 185204, 2011.

[125] L. Liard, J.-L. Raimbault, and P. Chabert, "Competitive effects of an axial magnetic field and of neutral gas depletion in a positive column," *Phys. Plasmas*, vol. 16, p. 053507, 2009.

[126] G. Sato, W. Oohara, and R. Hatakeyama, "Experimental characterization of a density peak at low magnetic fields in a helicon plasma source," *Plasma Sources Sci. Technol.*, vol. 16, no. 4, p. 734, 2007.

[127] T. Lafleur, C. Charles, and R. Boswell, "Ion beam formation in a very low magnetic field expanding helicon discharge," *Phys. Plasmas*, vol. 17, p. 043505, 2010.

[128] ——, "Plasma control by modification of helicon wave propagation in low magnetic fields," *Phys. Plasmas*, vol. 17, p. 073508, 2010.

[129] ——, "Characterization of a helicon plasma source in low diverging magnetic fields," *J. Phys. D: Appl. Phys.*, vol. 44, no. 5, p. 055202, 2011.

[130] ——, "Electron–cyclotron damping of helicon waves in low diverging magnetic fields," *Phys. Plasmas*, vol. 18, p. 043502, 2011.

[131] T. Lho, N. Hershkowitz, J. Miller, W. Steer, and G. H. Kim, "Azimuthally symmetric pseudosurface and helicon wave propagation in an inductively coupled plasma at low magnetic field," *Phys. Plasmas*, vol. 5, p. 3135, 1998.

[132] H. Lorzel and P. G. Mikellides, "Three-dimensional modeling of magnetic nozzle processes," *AIAA J.*, vol. 48, no. 7, pp. 1494–1503, 2010.

[133] J. D. Scudder and S. Olbert, "A theory of local and global processes which affect solar wind electrons 2. experimental support," *J. Geophys. Res.*, vol. 84, no. A11, pp. 6603–6620, 1979.

[134] M. Birkinshaw, "Instabilities in astrophysical jets," *Astrophys. and Space Sci.*, vol. 242, pp. 17–91, 1997.

[135] P. M. Bellan, *Fundamentals of Plasma Physics.* Cambridge University Press, 2006.

[136] I. I. Litvinov, "Stationary efflux into a vacuum by a dual-temperature fully ionized plasma," *J. Appl. Mech. Tech. Phys.*, vol. 12, no. 6, pp. 793–802, 1971.

[137] L. Spitzer Jr and R. Härm, "Transport phenomena in a completely ionized gas," *Phys. Rev.*, vol. 89, no. 5, p. 977, 1953.

[138] R. Malone, R. McCrory, and R. Morse, "Indications of strongly flux-limited electron thermal conduction in laser-target experiments," *Phys. Rev. Lett.*, vol. 34, no. 12, p. 721, 1975.

[139] W. Fundamenski, "Parallel heat flux limits in the tokamak scrape-off layer," *Plasma Phys. Contr. F.*, vol. 47, no. 11, p. R163, 2005.

[140] Ø. Lie-Svendsen, T. E. Holzer, and E. Leer, "Electron heat conduction in the solar transition region: validity of the classical description," *AsJ*, vol. 525, no. 2, p. 1056, 1999.

[141] T. Bose, "Thermodynamic expansion processes for argon plasma in a convergent-divergent nozzle." *J. Spacecraft Rockets*, vol. 10, no. 9, pp. 613–615, 1973.

[142] S. Mazouffre, M. Boogaarts, I. Bakker, P. Vankan, R. Engeln, and D. Schram, "Transport of ground-state hydrogen atoms in a plasma expansion," *Phys. Rev. E*, vol. 64, no. 1, p. 016411, 2001.

[143] W. C. Feldman, J. R. Asbridge, S. J. Bame, J. T. Gosling, and D. S. Lemons, "Electron heating within interaction zones of simple high-speed solar wind streams," *J. Geophys. Res.*, vol. 83, no. A11, pp. 5297–5303, 1978.

[144] K. Burm, W. J. Goedheer, and D. Schram, "The isentropic exponent in plasmas," *Phys. Plasmas*, vol. 6, no. 6, pp. 2622–2627, 1999.

[145] W. W. Dalton and S. A. Balbus, "A flux-limited treatment for the conductive evaporation of spherical interstellar gas clouds," *AsJ*, vol. 404, pp. 625–635, 1993.

[146] G. Aston, H. R. Kaufman, and P. J. Wilbur, "Ion beam divergence characteristics of two-grid accelerator systems," *AIAA J.*, vol. 16, no. 5, pp. 516–524, 1978.

[147] J. A. Linnell and A. D. Gallimore, "Efficiency analysis of a hall thruster operating with krypton and xenon," *J. Propul. Power*, vol. 22, no. 6, pp. 1402–1418, 2006.

[148] W. Cox, C. Charles, R. W. Boswell, and R. Hawkins, "Spatial retarding field energy analyzer measurements downstream of a helicon double layer plasma," *Appl. Phys. Lett.*, vol. 93, no. 7, p. 071505, 2008.

[149] H. Tsui, A. Wootton, J. Bell, R. Bengston, D. Diebold, J. Harris, N. Hershkowitz, C. Hidalgo, J. Ingraham, S. Kilpatrick *et al.*, "A comparison of edge turbulence in tokamaks, stellarators, and reversed-field pinches*," *Phys. Fluids B: Plasma Phys.*, vol. 5, no. 7, pp. 2491–2497, 1993.

[150] V. Antoni, D. Desideri, E. Martines, G. Serianni, and L. Tramontin, "Plasma potential well and velocity shear layer at the edge of reversed field pinch plasmas," *Phys. Rev. Lett.*, vol. 79, no. 24, p. 4814, 1997.

[151] R. Bamford, K. J. Gibson, A. J. Thornton, J. Bradford, R. Bingham, L. Gargate, L. O. Silva, R. A. Fonseca, M. Hapgood, C. Norberg *et al.*, "The interaction of a flowing plasma with a dipole magnetic field: measurements and modelling of a diamagnetic cavity relevant to spacecraft protection," *Plasma Phys. Contr. Fusion*, vol. 50, no. 12, p. 124025, 2008.

[152] K. Burrell, "Effects of $E \times B$ velocity shear and magnetic shear on turbulence and transport in magnetic confinement devices," *Phys. Plasmas*, vol. 4, no. 5, pp. 1499–1518, 1997.

[153] M. Shoucri, "Charge separation and electric field at a cylindrical plasma edge," in *Numerical Simulation - From Theory to Industry*, M. Andriychuk, Ed. InTech, 2012.

[154] E. E. Scime, P. A. Keiter, M. W. Zintl, M. M. Balkey, J. L. Kline, and M. E. Koepke, "Control of ion temperature anisotropy in a helicon plasma," *Plasma Sources Sci. Tech.*, vol. 7, no. 2, p. 186, 1998.

[155] A. E. Petrov, K. A. Sarksyan, N. N. Skvortsova, and N. K. Kharchev, "Observation of nonlinear coupling between drift and ion-acoustic oscillations in low-frequency plasma turbulence," *Plasma Phys. Reps.*, vol. 27, no. 1, pp. 56–61, 2001.

[156] Y. Kawai and M. Guyot, "Observation of anomalous resistivity caused by ion acoustic turbulence," *Phys. Rev. Lett.*, vol. 39, no. 18, p. 1141, 1977.

[157] C. Charles, "High density conics in a magnetically expanding helicon plasma," *Applied Physics Letters*, vol. 96, no. 5, p. 051502, 2010.

[158] S. Saha, S. Raychaudhuri, S. Chowdhury, M. Janaki, and A. Hui, "Two-dimensional double layer in plasma in a diverging magnetic field," *Phys. Plasmas*, vol. 19, no. 9, p. 092502, 2012.

[159] S. Rao and N. Singh, "Numerical simulation of current-free double layers created in a helicon plasma device," *Phys. Plasmas*, vol. 19, no. 9, p. 093507, 2012.

[160] J. M. Little and E. Y. Choueiri, "Plasma detachment and momentum transfer in magnetic nozzles," in *Proceedings of 47th Joint Propulsion Conference, San Diego, CA (American Institute of Aeronautics and Astronautics, Washington DC, 2010), AIAA Paper*, no. 2011-6001, 2011.

[161] C. F. Kennel and J. M. Greene, "Finite larmor radius hydromagnetics," *Ann. Phys.*, vol. 38, no. 1, pp. 63–94, 1966.

[162] B. Tian, E. Ahedo, and J. Navarro-Cavalle, "Investigation of plasma-wave interaction in helicon antenna thrusters."

[163] G. R. Tynan, M. J. Burin, C. Holland, G. Antar, N. Crocker, and P. H. Diamond, "Radially sheared azimuthal flows and turbulent transport in a cylindrical plasma," *Phys. Plasmas*, vol. 11, no. 11, pp. 5195–5203, 2004.

[164] M. J. Burin, G. R. Tynan, G. Y. Antar, N. A. Crocker, and C. Holland, "On the transition to drift turbulence in a magnetized plasma column," *Phys. Plasmas*, vol. 12, no. 5, p. 052320, 2005.

[165] C. Holland, J. Yu, A. James, D. Nishijima, M. Shimada, N. Taheri, and G. Tynan, "Observation of turbulent-driven shear flow in a cylindrical laboratory plasma device," *Phys. Rev. Lett.*, vol. 96, no. 19, p. 195002, 2006.

[166] C. J. Chen, "Anomalous diffusion and instabilities of an argon plasma in a strong magnetic field," *J. Appl. Phys.*, vol. 37, no. 1, pp. 419–425, 1966.

[167] B. A. Jorns, I. G. Mikellides, and D. M. Goebel, "Investigation of energetic ions in a 100-a hollow cathode," in *Proceedings of 50th Joint Propulsion Conference, Cleveland, OH (American Institute of Aeronautics and Astronautics, Washington DC, 2010), AIAA Paper*, no. 2014-3826, 2014.

[168] P. F. Schmit and N. J. Fisch, "Magnetic detachment and plume control in escaping magnetized plasma," *J. Plasma Phys.*, vol. 75, no. 03, pp. 359–371, 2009.

[169] L. Ferrario, J. M. Little, and E. Y. Choueiri, "Propulsive performance of a finite-temperature plasma flow in a magnetic nozzle with applied azimuthal current," *Phys. Plasmas*, p. Accepted, 2014.

[170] ——, "Experimental investigation of plasma plume characteristics in applied radial electric field magnetic nozzle." in *Proceedings of 50th Joint Propulsion Conference, Cleveland, OH (American Institute of Aeronautics and Astronautics, Washington DC, 2010), AIAA Paper*, no. 2014-4026, 2014.

[171] J. D. Jackson and J. D. Jackson, *Classical electrodynamics.* Wiley New York etc., 1962, vol. 3.

177